12-2022

DETERMINATION OF NEAR-SOL CARBON IMPURITY CONTENT DUE TO DIVERTOR TARGET LEAKAGE USING CARBON-13 TRACERS VIA METHANE INJECTION ON THE DIII-D TOKAMAK

Jonah David Duran
University of Tennessee, Knoxville, jduran2@vols.utk.edu

Recommended Citation

Duran, Jonah David, "DETERMINATION OF NEAR-SOL CARBON IMPURITY CONTENT DUE TO DIVERTOR TARGET LEAKAGE USING CARBON-13 TRACERS VIA METHANE INJECTION ON THE DIII-D TOKAMAK. " PhD diss., University of Tennessee, 2022.
https://trace.tennessee.edu/utk_graddiss/7732

To the Graduate Council:

I am submitting herewith a dissertation written by Jonah David Duran entitled "DETERMINATION OF NEAR-SOL CARBON IMPURITY CONTENT DUE TO DIVERTOR TARGET LEAKAGE USING CARBON-13 TRACERS VIA METHANE INJECTION ON THE DIII-D TOKAMAK." I have examined the final electronic copy of this dissertation for form and content and recommend that it be accepted in partial fulfillment of the requirements for the degree of Doctor of Philosophy, with a major in Nuclear Engineering.

David Donovan, Major Professor

We have read this dissertation and recommend its acceptance:

David Donovan, Lawrence Heilbronn, Ezekial Unterberg, Peter Stangeby

Accepted for the Council:

Dixie L. Thompson

Vice Provost and Dean of the Graduate School

(Original signatures are on file with official student records.)

DETERMINATION OF NEAR-SOL CARBON IMPURITY CONTENT DUE TO DIVERTOR TARGET LEAKAGE USING CARBON-13 TRACERS VIA METHANE INJECTION ON THE DIII-D TOKAMAK

A Dissertation Presented for the
Doctor of Philosophy
Degree
The University of Tennessee, Knoxville

Jonah David Duran
December 2022

This dissertation is dedicated to my wife, friends, and family who have all supported my journey through graduate school and instilled in me a passion for acquiring knowledge.

ACKNOWLEDGEMENTS

I would like to begin by acknowledging the support of my thesis advisor, David Donovan, for introducing me to the world of fusion energy research and providing me with a sound foundation for my career. With his introduction, there have been many other professionals that I have encountered and learned from along the way. I would like to thank Shawn Zamperini, Jake Nichols, Mike Zach, Zeke Unterberg, Peter Stangeby, and Lawrence Heilbronn. Thank you for the valuable discussions, the many ideas and innovations, mentorship and advisement, your many contributions to the field that have been foundational to this work, and for general support throughout my college career. For their surface characterization expertise and ion beam analysis support, I would like to acknowledge Bill Wampler and Kevin Woller. I would also like to thank Doug Fielden and Larry Smith for the many machining efforts that have made this work possible with tight deadlines and their valuable insights into diagnostic design. Finally, I would like to acknowledge the Stable Isotopes Division at ORNL as well as the DIII-D team in San Diego for their support.

ABSTRACT

Experiments with outer strike point injection of isotopically enriched methane ($^{13}CD_4$) in DIII-D L-mode discharges have demonstrated the ability to infer near scrape-off-layer (SOL) impurity density profiles based on: far-SOL collector probe (CP) measurements; a stable isotopic mixing model; and SOL impurity transport modelling. This work enables one of the first in-depth investigations on the source and transport of SOL impurities which could hinder performance of future fusion devices. Modelling by DIVIMP and 3DLIM of ^{13}C SOL evolution is consistent with diagnostic observations and indicates that the buildup of injected impurities on plasma-facing surfaces must be considered while inferring representative impurity distributions. Namely, ^{13}C deposits on the inner and outer targets are shown to contribute 50% at a minimum of the enriched ^{13}C deposition on CPs and to cause poloidal shifting of the impurity density peaks in the near-SOL. This analysis elucidates the importance of source location, connection length, poloidal diffusion, and radial convective velocity of impurities to accurately model and interpret SOL impurity behavior.

TABLE OF CONTENTS

LIST OF TABLES

LIST OF FIGURES

CHAPTER ONE
LITERATURE REVIEW

1.1 The Road to Fusion

The idea of obtaining the power of the stars for use on Earth goes back to the early 1900s when scientists developed theories that describe the nuclear fusion processes occurring within the sun. This work led to the ideas of confining a similar plasma in order to control a nuclear fusion reaction in an attempt to generate electricity. While there are no materials that can directly interact with the fusion reaction temperatures that reach over one hundred million degrees, fusion energy scientists have turned to magnetic and inertial confinement to control fusion processes. Initial fusion experiments encountered unforeseen instabilities which have led to a loss of plasma confinement, and research efforts since have focused on suppressing and mitigating these phenomena. These efforts have placed the toroidal magnetic chamber or tokamak (Figure 1) as the front runner device for generating fusion power and is the focus of a majority of international research [1].

The tokamak, however, still has issues of its own. As depicted in Figure 2, these devices take advantage of a divertor configuration in which there is a region outside of the core plasma referred to as the scrape-off-layer (SOL). This region is separated from the core by a boundary referred to as a ‘separatrix’ and comes into contact with a material surface of the device. Extreme plasma material interactions take place in this region [2]. Intense plasma material interaction events cause the atoms of the encountered material surface to eject from the wall and enter the plasma. Introduction of such non-fueling wall material species (impurities) contaminates plasma and leads to plasma energy loss through radiative power losses. While the divertor region is often equipped with vacuum pumps that strive to remove these disruptive impurities upon generation, the processes for doing so have not yet been perfected. Thus, there is additional need for dedicated research toward understanding the evolution of impurities throughout a tokamak plasma. With greater understanding of these processes, the fusion community may be better equipped to suppress, mitigate, or control impurities for the benefit of fusion power.

1.2 Plasma Material Interactions

Figure 3 depicts the complex reality that materials face in the environment of a fusion reactor. When a plasma strikes a material surface, the high energy flux of plasma particles interacts with the surface material atoms and transfer energy through collisions or chemical interactions. Ion impact can result in reflection, implantation, redeposition, fuel recycling, or even sputtering and ionization followed by long-range material transport throughout the fusion plasma. If the energy delivered to a surface atom exceeds that of the binding energy holding it within the material lattice, then the atom may eject from the surface through a process called physical sputtering. Different materials result in a variable number of ejected atoms per incident particle based on particle energy and type. This number of particles produced by incident ions is represented by the sputtering coefficient as seen in Figure 4. There is a threshold energy value to begin sputtering that is dependent upon the binding energy and the masses of both the incident and the surface atoms. Carbon surfaces exhibit enhanced chemical sputtering processes that occur due to the formation of C-H molecules at the material surface. These compounds have a reduced binding energy that may increase the sputtering yields by a factor of two or more. A third process called self-sputtering may also take place when the eroded surface particles become ionized and travel back to the material surface. Self-sputtering interactions are particularly detrimental to fusion devices as they may lead to an increased rate of material erosion well above tolerable limits.

As these eroded particles enter the plasma, they change the background plasma from a purely hydrogen base to a mixture of ionic species. This changes the effective charge, Z_{eff}, that is averaged over all plasma ions and results in the radiative cooling of the plasma. Bremsstrahlung, line, and recombination radiation cooling processes cause power loss in the plasma core. The collection of the three aforementioned radiative cooling mechanisms define the impurity radiative power loss. Such losses have been used to set thresholds on impurity concentrations that are permissible in the plasma in order to satisfy the fusion power balance without any external heating as seen in Figure 5 for different plasma energy levels. This ‘ignition’ condition is the motivation for preventing sputtered impurity ions from entering the plasma. If we can maintain the plasma’s heat at high enough energy for long enough periods of time, there is a theoretical feedback loop which causes the nuclear fusion reaction to become self-sustaining. Reduction of the various cooling mechanisms allows the fusion reaction heating of the fuel mass to become more efficient. Once this ignition point is reached, no more external energy is needed to heat the fuel and the energy gained from the reaction can become a viable electricity source. Of course, the materials that are currently available and used in fusion systems are not ideal and continue to cause deleterious effects to the ongoing experimental plasma fusion research. These effects have continued to prevent fusion experiments from reaching neither ignition or breakeven. Achieving breakeven ($E_{in} = E_{out}$) is paramount before we can tackle the bigger challenge of ignition that will lead to commercial fusion power plants.

Several mitigation schemes have been employed in current fusion experiments with some success. Limiting the energy of the plasma particles interacting with the wall below the threshold values listed in Figure 4 is one common technique for avoiding a breach of the impurity concentration threshold. Divertor configurations have also displayed the ability to significantly reduce the amount of impurities that make their way into the plasma. Unfortunately, these techniques are not a panacea for controlling impurities. Many modern fusion reactor designs that are under construction take advantage of the divertor configuration of Figure 2 that use pumps and gas puffing to increases plasma density and decreases plasma temperature within the divertor region. This will then reduce the impurity productions rates, as shown in Figure 1, and pump out particles that are liberated from the target surface.

1.3 Impurity Transport

The processes leading to the generation of an impurity source are well characterized within the fusion community. However, edge plasma transport as well as ion transport from the plasma edge into the main plasma (core) require additional research and support. A simplified model and schematic of these events is shown in Figure 6.

Edge transport processes and migration into the core are active areas of research for the fusion community; however, fundamental impurity transport theory has been developed and is well documented [3]. The transport of impurities is described as being primarily driven by the background plasma which is comprised of the fueling species of hydrogen isotopes. The direction of such impurity flows is generally referenced as parallel or perpendicular to the magnetic field lines with parallel motion greatly outweighing that in the perpendicular direction. Parallel impurity motion is determined by a balance of several forces as seen in Equation 1.1.

$$F_z = -\frac{1}{n_z}\frac{dp_z}{ds} + m_z\frac{(v_i - v_z)}{\tau_s} + ZeE + \alpha_e\frac{d(kT_e)}{ds} + \beta_i\frac{d(kT_i)}{ds} \qquad 1.1$$

The equation includes the impurity pressure gradient force in the first term, the friction force on the impurity ions exerted by the background plasma in the second term, the electrostatic force exerted by the parallel electric field E in the SOL in the third term, and finally the electron and ion temperature gradient forces respectively. Constants and variables in the equation include the impurity density (n_z), impurity pressure gradient ($\frac{dp_z}{ds}$), mass of the impurity (m_Z), parallel fluid velocity of impurity ions (v_z), background ion parallel fluid velocity (v_i), stopping time (τ_s), atomic number (Z), parallel electric field (E), electron temperature gradient ($\frac{d(kT_e)}{ds}$), ion temperature gradient ($\frac{d(kT_i)}{ds}$), and coefficients on the order of Z^2 (α_e, β_i).

As a result of the forces acting on the impurities, theory supports the idea that an impurity build-up or trap occurs near the crown (top of the plasma) of the SOL of single null plasmas that were shown in Figure 2. Thermal forces caused by plasma boundary temperature gradients tend to result in a force null in the plasma crown. With no parallel forces acting on impurities, they then accumulate and result in increased near-SOL impurity density profiles [4, 5]. The formation of an impurity stagnation region within the near-SOL can be detrimental to a plasma. With increased impurity densities directly adjacent to the plasma core, cross-field motion can cause the impurities to directly leak into the plasma core from the SOL impurity well. Again, this is an undesirable outcome due to the radiative power losses that occur when impurities enter the core.

Code predictions of SOL impurity motion, as is shown in Figure 7, also support the theory that an impurity accumulation exists close to the core of the plasma due to parallel forces [6]. The closest SOL region to the core containing the accumulated impurities is defined by the boundary plasma directly adjacent to the separatrix. The SOL is typically refined into two separate sections. The near-SOL, which extends a few mm from the Last Closed Flux Surface (LCFS), is often characterized as a 'complex SOL' with a steep gradient of the parallel heat flux radial profile. It has also been shown to hold the most dramatic plasma temperature gradients and largest target fluxes. The 'simple' far-SOL, typically several centimeters wide, is comprised of flatter heat flux profiles.

Recent experimental efforts have utilized two-faced collector probes which are inserted into the far-SOL of the experimental fusion tokamak, DIII-D, in order to collect traveling impurities [7]. These experimental studies are believed to provide indirect measurements of the long-theorized impurity accumulation region using collector probes at the outboard midplane of the device. Impurity content asymmetries between the two collector probe faces show greater levels of content on the collection face that is directed towards the plasma which flows from the accumulation region to the probe rather than from the direct source of impurities at the divertor target. This is asserted to be due to the complex combination of forces that include friction with the background plasma flows, ion and electron temperature gradient forces, forces from the electric fields, as well as a balance of momentum and cross-field flows, which are both drift and turbulence driven [8].

When considering perpendicular impurity motion in the SOL, a diffusive or convective assumption is often used for cross-field transport mechanisms depending on the SOL region of interest. However, particle drifts and turbulence have also shown to play a role in perpendicular transport of the edge plasma. Drift mechanisms in particular have been shown to motivate the change in asymmetry of the SOL. Several key drifts have been identified in a fusion environment [9]. These particle drifts arise when particles experience an electric field (E) perpendicular to the magnetic field (B) and is referred to as the $E \times B$ drift. In the presence of a magnetic field gradient that is perpendicular to the magnetic field, the $B \times \nabla B$ drift is also important to consider. There are some caveats to this drift depending on whether one is using upper single null or lower single null plasma shape. Lower single null plasmas are like those shown in Figure 1 and Figure 2 where the X-point is in the bottom of the device. Upper single null plasmas can be considered upside down where the X-point is instead in the top of the device. In upper single null and Forward directed toroidal magnetic field, B_T, as well as lower single null reverse B_T, the $B \times \nabla B$ drift is away from the target (Forward B_T is considered clockwise when viewed from the top of a tokamak while Reverse is counterclockwise). As an example, this is considered an unfavorable direction because the power access to H-mode is increased to ~3 MW in DIII-D when compared to the scenario of using a favorable direction. For forward B_T lower single null and reverse B_T upper single null plasma shape, where $B \times \nabla B$ is towards the target (favorable), the L-H mode transition is halved (~1.5 MW). Due to the natural curvature of the magnetic field, an additional drift affects the plasma in a toroidal device. As implied, the direction of the toroidal magnetic field may influence these drifts as well. Clockwise or 'normal' as opposed to counter clockwise field configurations have been shown to reverse several flow mechanisms.

DIVIMP-WallDYN modelling has recently investigated the consequence of ExB drifts on impurity transport [10]. The models have shown significant effects from both the magnitude and direction of the drifts. Within regions of the boundary plasma, it was found that drifts can dominate the net force balance on impurities and even affect the position of the theoretical impurity well (Figure 8). The resulting SOL transport due to these drifts is a bit more complex than a change of motion in one direction. Electric fields through the region disturb both parallel and perpendicular transport. These effects arise due to the poloidal $E_\theta xB$ drift that causes poloidal motion while the $E_r xB$ drift influences radial transport across the separatrix depending on the direction of the $Bx\nabla B$ drift. While these modelling results appear to significantly affect the boundary plasma, there are still other factors such as the Pfirsch-Schluter (P-S) flows which should be considered in future efforts.

It is also important to distinguish between to primary modes of operation in fusion plasma devices. Originally, a low-confinement mode of operation was used. As the community introduced additional plasma power schemes, a high-confinement mode was discovered to increase the confinement time of the machine. These are referred to as L-mode and H-mode, respectively. H-mode plasmas, however, was found to introduce edge localized modes that cause large particles and heat fluxes to escape from the plasma. As a consequence, these instability events often place constraints on plasma facing components. In addition, edge localized modes complicate the use of several diagnostics, unless viewing between edge localized modes. One good feature is that they also tend to flush impurities from the plasma periodically during the quasi-periodic relaxation of a transport barrier. For experiments and discussion presented in this dissertation, L-mode will be the primary mode of operation. H-mode plasma are more ideal for reactor relevant physics studies on core plasma. L-mode plasma still serve as excellent test-beds for studying edge plasma physics related to impurity transport.

1.4 Isotopes

In order to study the migration of impurities within a fusion plasma, it is important to distinguish the impurity of interest from the intrinsic materials used in the device. Many of the leading materials that are either currently in use or under consideration for use in fusion plasma facing materials (PFMs) include boron, graphite (carbon), beryllium, tungsten (W), molybdenum, lithium, and silicon. When these materials are chosen to be used in plasma facing components, they are made with standard abundance materials that are not enriched with any one isotope. For example, tungsten has natural abundance fractions for each isotope of 0.0012 ^{180}W, 0.2650 ^{182}W, 0.1431 ^{183}W, 0.3064 ^{184}W, and 0.2843 ^{186}W. The averaged mass of these isotopes is the value presented on the periodic table, but enrichment of any one isotope is one easy way to distinguish the material from the intrinsic background that may be already present in the experimental device. During the 2016 Metal Rings Campaign (MRC) at DIII-D, enriched tungsten was used with enrichment fractions of < 0.0005 ^{180}W, **0.9299 ^{182}W**, 0.0284 ^{183}W, 0.0279 ^{184}W, and 0.0138 ^{186}W. This allowed for enriched tungsten as well as tungsten of natural abundance to act as two unique sources of impurities which were later more easily characterized due to the use of unique isotopic signatures in a traditionaly all graphite device.

While solid forms of impurities are often of interest for impurity studies within fusion devices, gaseous species with isotopic enrichment are viable options to consider. It is also important to acknowledge some general criteria to follow when selecting such a tracer material. These include the selection of a tracer whose natural abundance is typically less than 1-2 atomic percent (at %) and behaves similarly to the main impurities of interest. The material should also be easily detectable by available isotopic surface analysis techniques. For fusion relevant systems, this typically limits the list to ^{13}C, ^{15}N, Si isotopes (from SiD_4) and tungsten isotopes (from WF_6) [11]. Unfortunately, special consideration is required to handle the toxic and corrosive WF_6. Of the remaining materials, it is then important to consider what type of material is of interest and what behavior it should exhibit along with what diagnostics can properly characterize the transport of the material in order to meet the experimental needs. For the purposes of the experiments to be presented herein, carbon is of primary interest. Carbon and materials such as tungsten exhibit a non-recycling nature which refers to the low back-scattering probability.

As described in the abstract and for the purposes of foreshadowing, presented experiments involve the injection and tracking of isotopically enriched ^{13}C throughout the DIII-D tokamak. Impurities are injected into upper single null plasmas in the form of $^{13}CD_4$ or methane. The ^{13}C disassociates, ionizes and is transported throughout the device. During the plasma discharge, a variety of diagnostics are used to observe the evolution of ^{13}C. In addition, collector probes are used to sample the enriched ^{13}C from the methane injection and natural carbon that is sourced from the plasma facing components of DIII-D. This presents a unique challenge for sample analysis due to carbon impurity tracers being injected into a predominantly carbon device while also being sampled using a carbon-based collector probe.

1.5 Injection of Non-Recycling Impurities

While investigating impurities, it is again important to consider which category of impurities are of interest. Figure 5 presents that the maximum allowable impurity concentration of a plasma scales dramatically with atomic number, therefore there is a considerable concern over heavy elements in a plasma which stems interest in studying heavier candidate PFMs such as tungsten. Metals are of the non-recycling impurity category, but they require substantial hardware development in order to introduce sufficient quantities of solid materials like tungsten into the main chamber of a fusion experiment. This was done during the 2016 metal rings campaign (MRC) where two toroidally symmetric rings of tungsten were installed in the lower divertor of DIII-D. As a proxy for tungsten and other heavy elements with non-recycling behavior, one can use carbon in the form of methane with no modification of a plasma device. Injection of non-recycling impurities also allows for simplification of the impurity transport scenario. The little and nearly negligible amount of impurity recycling of carbon allows for one to practically assume a once-through chance of contaminating the plasma before it become stuck to a physical surface with which it interacts. This refers to the previously described low probability to backscatter from a material surface. The point of injection and local versus symmetric injection of impurities has also shown to hold importance for similar studies. Later discussed experiments focus on axisymmetric, near-target injection of impurities, i.e. the ionization of impurities occurs near the target. This emulates sputtering of non-recycling impurities from the targets. Injection location can be modified without changing the inject port by simply moving the location of the plasma strike point around the divertor.

1.6 Beneficial Diagnostics

Impurities are often liberated from the plasma facing components of tokamaks and introduced to a high temperature environment. These temperatures tend to vary throughout various regions of a tokamak plasma. Depending on the temperature of the region through which an impurity is traversing, the impurity can evolve through a series of ionization states. Carbon, as seen in Table 1, may evolve through each of its ionization states as it progresses from the relatively cold divertor target temperatures to the hot core of the plasma. In order to keep track of these impurity states, multiple diagnostics are required. This section discusses a list of desirable diagnostics for observing the evolution of carbon impurities throughout DIII-D. Not all diagnostics were available during the experiments presented in later sections. If available, it would be ideal to use all mentioned in this section.

Modern tokamaks are equipped with a variety of diagnostics for monitoring and control of in-vessel conditions. In particular, General Atomics' DIII-D is one of the most heavily diagnosed magnetic fusion experiments with over 50 individual diagnostic systems. Electron temperature and density, ion temperature and velocity, core impurity concentration, radiated power, divertor monitoring, magnetic properties, plasma edge and all conditions, wave fluctuations and activities, particle monitoring, plasma current profiles, and other parameters or conditions are monitored using anywhere up to 10+ diagnostics each [12]. Multiple instruments are reviewed below with additional information specific to the DIII-D devices with a focus on carbon observation. Their specific experimental use will be described later.

Several of these systems are of particular interest for monitoring or even collecting impurities within a plasma. Penning gauges and ASDEX gauges are systems which may be utilized to detect impurity pressures. Penning gauges monitor the pressure of impurities in both the upper-outer and lower pump ducts of DIII-D. Measurements can be taken with 100 ms time-scales and are capable of measuring pressures from 0.01 mTorr to 15 mTorr. Line emission is filtered based on the impurity of interest and optical lines of sight exist in three locations per pumping duct. These are routinely used for Ne, N, Ar, He, and D/H, but additional hardware can expand this availability. ASDEX gauges are of interest for measuring neutral pressures with a time resolution generally between 1 and 10 msec. Additional gas injection monitoring on DIII-D is available through a CCD camera which is equipped with a band pass filter. For example, CD and CH molecules may be observed with a 430.5 nm filter in order to observe methane injection [13]. Alternatively, calculations of DIII-D plenum flow rates for toroidally symmetric sources are available for gas input rates.

Many spectroscopic systems are also useful in characterizing impurities within a fusion plasma device. SPRED spectrometers, for example, are often used to monitor low-Z impurities such as C, B, and O as well as medium-Z impurities within the core and divertor of DIII-D as seen in Figure 9. Depending on the grating that is used, the range of impurity line monitoring can extend from the extreme ultraviolet range into the visible ultraviolet wavelengths of ~170 nm. The SPRED spectrometers can also be calibrated using electron storage rings in order to produce response in terms of photons/count-cm^2-sr [14].

Charge-exchange excitation of spectral lines may also be observed using the Charge-Exchange Recombination (CER) diagnostic. This system is primarily used in tokamaks for measuring time evolved ion parameters such as temperature, density, and velocity. The diagnostic takes advantage of Doppler broadening, shift, and total intensity of the emissions lines in order to measure the ion characteristics. Typically, the species of interest for CER include low-Z impurities which are fully stripped. Boron and carbon data are often readily available with the system at DIII-D. Wavelength ranges for the CER are limited to spectral lines in the 300 to 800 nm range with the highest quality data in the visible and near IR portions of the spectrum from 400 to 800 nm. As partially seen in Figure 10, over 80 unique views are available within the DIII-D vessel both tangentially and vertically through the plasma at the midplane. DIII-D data analysis for CER is essentially automatic with a quick analysis performed between each shot and an improved automatic analysis performed overnight. Increasing the confidence of the data even further is available through a third analysis procedure that requires additional inspection by a diagnostician. The output from the automatic analyses are available in the MDSPlus data tree, but the final analysis option requires a user request.

Relating to boundary studies, another useful diagnostic includes the high-resolution Multichord Divertor Spectrometer (MDS). This instrument is capable of measuring low-Z impurities, deuterium, and even hydrocarbon fragment parameters. The ion temperature, parallel plasma flows, and impurity fluxes are available through view chords in both the upper and lower divertor strike points as well as additional tangential views directed toroidally in the lower divertor. Species having emissions within the spectral range of ~385 to 720 nm may be observed with frame rates up to 90 Hz. DIII-D is equipped with a McPherson model 209 Czerny Turner design spectrometer along with a 16-channel Princeton Instruments PI-MAX 1024i intensified charge-coupled device (CCD) camera. Data from these systems can be calibrated in a similar fashion as the SPRED systems in order to obtain intensity calibrations in units of photons/sr-cm^2-s-pixel. Only having to be calibrated once a year, readily available python tools at DIII-D allow for automatic application of calibration tools.

Tangentially viewing camera systems on DIII-D are comprised of three systems used extensively for gathering spatial distributions of radiation sources throughout the main chamber. Both the main chamber SOL as well as the two divertor regions are equipped with these diagnostics. Commonly the C^{3+} emissions are monitored within the VUV range at 155 nm in the divertor regions while the boundary views are line filtered in order to complement the bolometer arrays on DIII-D.

Spectral line monitoring filterscopes are also used in the divertor and outboard midplane regions of DIII-D in order to provide column-integrated measurements of impurities and deuterium. Lines of sight are oriented up and downward in a poloidal plane along with tangential lines of sight at the midplane. The current hardware has a sampling rate up to 100 kHz for simultaneous recording of CII, CIII, He II, D_α, and D_β signals. CII and CIII lines are available in the upper and lower divertor while the midplane view chords are limited to CIII. Calibration of the signal is again available in order to convert the signal into units of photons/(sr-cm^2-s).

In order to visually observe ion flow velocities throughout a plasma, coherence imaging spectroscopy (CIS) is used throughout the SOL and divertor regions of the DIII-D tokamak. Multiple analysis steps convert a wavelength-dependent interference pattern into a 2-D image of parallel ion velocities like the one shown in Figure 11. One camera is designed to have a wide field-of-view that includes the upper and lower divertors as well as the SOL while a second camera is aimed specifically at observing the ion flows in the lower divertor. Typically, CIII (465 nm) and HeII (468.6 nm) are the primary ions of interest around the divertor plates at temperatures of 10 to 40 eV. These measurements typically represent flows in the range of 0 to 40 km/s. The images produced come with a resolution of a few centimeters in the lower divertor view but can reach 1 cm with the upper, lower, and midplane camera.

For the purposes of observing an impurity accumulation region, the null point in the flow velocity measurements is critical to the development of an impurity stagnation region. With enough CIS data, the position of the accumulation could clearly be shown in the 2-D velocity maps as an area where there is a reversal of the flow velocity.

Collector probes are another diagnostic which are utilized in several tokamaks for the gathering of non-recycling impurities which travel throughout the outer edge of a plasma [7, 15, 16]. The exposed regions of such collector probes are inserted into the plasma edge during operation and then removed after the desired shot conditions. Characterization of the probes is performed through a variety of methods including laser ablation mass spectrometry as well as ion beam techniques including Rutherford backscattering (RBS) and nuclear reaction analysis (NRA). Laser ablation inductively couple plasma mass spectrometry (LA-ICP-MS or LAMS) is capable of producing high resolution 2-D surface maps of the deposited content while simultaneously determining isotopic ratios. RBS is best suited for determining the concentration of heavy or high-Z elements on low-Z substrates. This technique has been heavily used in fusion for the determination of tungsten areal densities across the surface of graphite collector probes. NRA is sort of the complementary technique that is best appropriate for measuring low Z elements and isotopes. Carbon isotopic analysis is available with the use of NRA through the ^{13}C (^{3}He, p) ^{15}N reaction. Further description of these techniques is presented in later sections.

There are multiple candidate locations for inserting collector probes into DIII-D; however, hardware requirements such as dwell time and drive distance limit the choices of currently available hardware to the Divertor Materials Evaluation System (DiMES) and the Midplane Material Evaluation System (MiMES) [17, 18]. These instruments have been used with success in order to understand plasma material interaction events such as erosion, retention, and material transport [19]. During the initial DIII-D Metal Rings Campaign in 2016, the MiMES station was used to introduce a triplet set of graphite collector probes into the outboard midplane SOL for shots 167173–167619. A schematic of this probe set may be seen in Figure 12.

Typically, half of the *connection* length determines the volume of plasma that is sampled by collector probes or the sampling length. Connection length is the distance to the nearest limiting surface when following a field line trace that begins at the collector probe sampling surface. However, various probe diameters were found to determine the parallel *sampling* length along the field lines during the Metal Rings Campaign. The *collection* length depends on the local sound speed of the background plasma, c_s, as well as the perpendicular diffusion coefficient, $D_\perp$. Exercising the following equation, we see that larger probes sample over a greater distance. For larger probes, the connection length is sufficient for determining the sampling length.

$$L_C \cong \frac{d^2 c_s}{4D_\perp} \tag{1.2}$$

DiMES probes had not previously been implemented, but the current design includes a 3 cm wide collector probe that was developed and implemented during the experiments presented here. Having multiple probing locations allows for more accurate determination of impurity transport within the SOL. With upper single null plasmas, the DiMES probe provides direct sampling of impurities near the plasma crown while the MiMES probe provides impurity information at the outer midplane of DIII-D. Each probe has two flat faces for collecting the far-SOL impurity content of DIII-D. Both flat collection faces are oriented such that they are approximately normal to the direction of the toroidal magnetic field. If one were to follow the field line trace from a flat collection face, it would terminate on the first limiting surface in either the inner or outer target direction. These are named accordingly as the inner target facing (ITF) and outer target facing (OTF) sides of the collector probes.

A number of unique probe designs have been used in previous experiments which include collector probe measurements. Fully exposed and windowed probes of pure graphite have been used and are shown in Figure 12. Other designs have incorporated material coatings and revolving sample exchange systems such as the design used by Emmoth et al. in Figure 13. When designing probes, the features presented are important to consider and the measurement techniques that were previously mentioned could benefit from design changes. Experience with collector probes during the Metal Rings Campaign has shown an interest in having wider probes that are not windowed e.g. solid wide faced probes. Solid and flat collection face designs are not complicated by the shadowing of a housing unit that is used with collection face inserts. In addition, ion beam analysis of the deposited materials has been shown to include a correction factor when accounting for the contribution of substrate material within the first 600 nm of the collection surface. Addition of a silicon layer that is ≥ 600 nm thick could therefore simplify the material characterization by NRA, but initial LAMS tests and SIMNRA modeling show that several microns worth of coating are necessary in order to eliminate the carbon signal contributions from the substrate material. There is the alternative of using a housing or probe that is completely comprised of a material that is not of interest such as the housing unit that is labeled ‘a’ in Figure 13. This may come at an extra cost but could again simplify any ex-situ analysis of the deposited materials across a probes surface. Many facilities such as the University of Tennessee’s (UTK) Joint Institute for Advanced Materials (JIAM) Micro-Processing Research Facility (MPRF) or Oak Ridge National Lab’s (ORNL) Nanoscale Science and Technology Laboratory (NSTL) have user based thin film deposition systems for this need.

1.7 Characterization Methods

While injected impurities can often be observed spectroscopically, the use of collector probes will require further *ex-situ* analysis. In order to evaluate the deposition of ^{13}C on collector probes made of graphite, a technique such as NRA or LAMS, which is capable of distinguishing low-Z isotopes is required. Bill Wampler of Sandia National Laboratory characterized the tungsten which deposited on graphite collector probes during the 2016 Metal Rings Campaign using RBS. This ion beam facility is also capable of running NRA experiments and has had success in distinguishing ^{13}C from ^{12}C for samples exposed to DIII-D discharges that included $^{13}CH_4$ injection [20-22]. Through the use of the ^{13}C (^3He, p) ^{15}N reaction, this technique is capable of measuring deuterium, boron, and both isotopes of carbon content at the sample surface. An example energy spectrum for tile measurements is shown in Figure 14. Here a graphite, ^{13}C, and D reference spectrum are plotted on top of DIII-D plasma facing component tile measurements. The ^{13}C reference spectrum has been scaled to indicate the yield from 10^{17} atoms/cm^2. The deuterium reference spectrum has been scaled to indicate the yield from 10^{18} atoms/cm^2. Above channel 400 data have been scaled down by a factor of 100 so that peaks from ^{13}C and deuterium can both be clearly seen.

In order to make these measurements, a specialized detector geometry is required for optimizing the resulting signal. With a 2.5 MeV ^3He analysis beam incident upon the sample surface, 10.6 MeV energy protons are measured with an annular detector as seen in Figure 15. A high solid angle for detection is obtained when implementing the large diameter annular silicon surface barrier detector that is 3 cm from the target. While the ^{13}C peak is quite narrow at 10.6 MeV, natural graphite still has a 1.1% natural abundance of ^{13}C. Therefore, in order to obtain a sufficient total quantity of ^{13}C, an ample injection of $^{13}CH_4$ is required. Depth resolved areal density measurements can be obtained through a series of steps. First, the ^{13}C yield is obtained through summing the ^{13}C values of corresponding channels. In Figure 14, this refers to channels 378-381. Then, a background subtraction of the 1.1% natural abundance ^{13}C and the offset from the tile spectra is used to correct the signal. The remainder is then converted to areal density based on the yield of an isotopically pure reference sample where the areal density is already known.

LA-ICP-MS is another technique capable of distinguishing isotopes while providing quantitative measurements of elemental and isotopic surface concentration measurements for deposited materials [23]. The technique has been used to map the surface content of various isotopic ratios. Enrichment fractions or a single isotope's contribution to the total elemental signature have also been provided by the technique. Quantitative mapping of elemental and individual isotopic areal densities is also possible with this technique if the proper calibration reference materials are available. The technique requires user selection of laser energy, frequency, ablation size, raster speed, as well as settings for the gas flow dynamics. Line scans of collector probes from MRC 1 have shown qualitative agreement with RBS trends across the surface of collector probes. Currently, ORNL's stable isotope group has a UP-213 nm laser ablation tool coupled with an Agilent 7700x quadrupole mass spectrometer which is accessible by our research group. With this system, sample preparation is not required unless the sample size exceeds the 6"x6"x1" dimensions of the large format cell that is installed on the UP-213.

1.8 Impurity Modeling

In order to support these measurements, simulations of impurity particles in steady state plasma conditions is available with the use of several codes. OEDGE (OSM+EIRENE+DIVIMP) and 3DLIM are two that are used to simulate impurity profiles throughout the SOL and to simulate impurity transport near collector probes respectively [6, 10, 24-31]. These models are constrained based on experimental measurements of the plasma temperature and density using upstream Thomson Scattering measurements as well as Langmuir Probe measurements at the strike points, see Figure 2. Electron temperature and density profiles from these diagnostics are used to reconstruct edge background plasmas. DIVIMP is able to launch impurity particles into these reconstructed plasmas in order to simulate and predict impurity density profiles throughout the SOL.

3DLIM is used to model impurity transport and the resulting deposition of impurities on nearby limiting surfaces. Collector probes act as limiting surfaces as they are inserted into plasmas. 3DLIM aims to recreate the experimental deposition patterns using experimental constraints. Additional tuning parameters then provide additional insight into the controlling mechanisms for impurity transport near collector probes.

1.9 Previous Tracer Experiments

Methane injection experiments for material migration has been carried out on a number of plasmas including DIII-D, JET, JT-60U, and TEXTOR [32]. These prior experiments locally injected $^{13}CH_4$ into the devices at various locations throughout the vessel. However, DIII-D is uniquely capable of injecting methane as a toroidally symmetric source through the use of multiple injection ports and a pumping plenum to the main vessel. These previous $^{13}CH_4$ experiments typically took place at the end of the run time campaigns in order to allow for tile removal and analysis after the methane exposures. This factor limits these sorts of experiments to only occur during a venting of the torus. Results from the experiments have focused on areas of large net deposition and studying co-deposition of fuel species. While most of the tile deposition studies were in forward oriented toroidal field configuration, the ^{13}C migration path was observed to result in inner divertor deposition.

Another method for tracking impurities involves particle conservation models such as AURORA [33]. These have been developed for a number of ion species that are common to divertor tokamaks. Main ion particle balance has been the primary interest for a number of studies in which a multi-reservoir model is used to study plasma flows. There has also been some work on the transport of recycling impurities such as nitrogen and neon using similar models. Model variables include the number of particles traveling throughout the reservoir system and their residence times within each reservoir. These values can be tracked with the host of diagnostics that are available on DIII-D. Coupled equations can be used to track the global migration of the particles of interest from one reservoir to the next.

CHAPTER TWO
RESEARCH DESIGN AND METHODS

2.1 Overview

Recent strategic planning reports by the US Department of Energy and the Office of Fusion Energy Sciences, place boundary and plasma material interaction solutions as major interests to the fusion community. In response to this need, DIII-D has recently placed increased emphasis on an attempt to understand the plasma-material interface and the plasmas response to plasma material interaction events. With this push, they are aiming to better understand the underlying processes that occur during the lifetime of an impurity. This includes how plasma material interaction events lead to erosion and sourcing of material in the divertor which then transports through the SOL of the plasma. Once impurities enter the plasma, there is then a question of the plasma variations that these impurities cause within the plasma edge and core along with identifying the parameters which control impurity transport processes. More experience with these topics provides a better understanding of global plasma material interactions and impurity transport physics that enable a predictive capability for material migration and mitigation.

PMI experiments at DIII-D have recently focused on installing tungsten tiles throughout the device as a method for introducing high-Z, non-recycling impurities. For example, tungsten tiles have most recently been installed in a small angle slot divertor in order to study the effects of unique divertor designs at the site of plasma material interactions. The dedicated focus towards using solid forms of high-Z materials is beneficial due to the contrast the carbon background that is used for the remaining plasma facing components in DIII-D and the likelihood of using tungsten in future fusion devices. The 2016 Metal Rings Campaign also provided utility in using isotopic tungsten particles in order to study plasma material interaction within DIII-D. With isotopic fractions from Table 2, a metal ring made of natural and another of enriched tungsten were used to provide impurity sourcing and transport information in conjunction with a stable isotopic mixing model [34]. While valuable for experiments, installation of metal tiles can require a significant investment of resources.

Other studies have shown that there are also a number of candidate gaseous materials which may be used for tracer experiments. Isotopically enriched methane is an ideal tracer for impurity studies because the natural abundance of ^{13}C only accounts for ~1 % of the natural elemental abundance. Using $^{13}CD_4$ that is isotopically enriched up to 99 atom percent ^{13}C will therefore essentially provide a second source of isotopically distinct material that is easily measurable by *ex-situ* characterization techniques such as NRA and LA-ICP-MS.

^{13}C has previously been used in tracer experiments at DIII-D and other devices in order to determine campaign integrated deposition patterns across wall surfaces along with co-deposition studies [32]. Presented herein is a unique opportunity with upper single null discharges at DIII-D where isotopically enriched $^{13}CD_4$ may be injected into the upper baffle of the device in conjunction with the vast arrays of spectroscopic diagnostics and collector probes. The outer strike point of the plasma may then be positioned over the injection location in order to introduce the isotopic methane tracer particles into the SOL of the plasma as shown in Figure 16.

General Atomics has equipped their device with some of the leading diagnostics for monitoring carbon density evolutions through spectroscopic devices. As seen in Figure 16, they also have at least two potential locations where collector probes may be inserted into the device in order to collect the dissociated ^{13}C that flows throughout the plasma. The divertor and midplane materials evaluation systems at DIII-D are located near the outboard midplane of the device (MiMES) and in the shelf of the lower divertor (DiMES) [18]. Probes may be inserted into the plasma SOL with these systems and exposed to single unique shots or sets of repeat and identical shots. Once exposed to a set of plasma conditions, they may be removed for *ex-situ* analysis.

Areal density measurements of isotopic ^{13}C measurements may be obtained through the use of ion beam techniques such as nuclear reaction analysis [20]. Alternatively, laser ablation mass spectrometry is capable of making qualitative measurements of the distributed ^{13}C content on collector probes, but quantitative measurements require additional research and development for calibration standards.

The experiments presented here provide novel data using a dual collector probe assembly in DIII-D to sample isotopically unique carbon tracer particles following methane injection into the device. Results focus on the near-SOL and far-SOL reservoirs. Near-SOL results and modelling offer additional evidence for near-SOL increase in impurity density that is supported and inferred by far-SOL measurements. These experiments also provide benchmarking opportunities for edge plasma codes such as DIVIMP and 3DLIM with additional support from the UTK research group under Dr. David Donovan. These experiments also lay the groundwork for future studies on DIII-D that will use a similar workflow along with the dual collector probe system that is developed for this dissertation.

2.2 Collector Probe Design

For this dissertation and future experiments, new collector probe designs were developed for both MiMES and DiMES in order to iterate and include beneficial design features from the probes used during the 2016 Metal Rings Campaign (Figure 12). The new probes are referred to as the MiMES Collector Probe (MCP) and the DiMES Collector Probe (DCP). Both the MCPs and DCPs include a solid design at ~3 cm in diameter and the full assembly for both can be seen in Figure 17. Analysis during the 2016 Metal Rings Campaign has motivated this design such that we are able to sample and characterize a wider region across the probe width in comparison to the windowed 3 cm probes of the past. The edges of the two fully exposed probes in the Metal Rings Campaign tended to have a higher content than the center of the probe width which is indicative of impurity transport processes in the SOL. This led to the belief that the 3 cm probe inserts could be improved in order to capture a wider view.

Originally, a set of flat collection plate inserts were designed to fit into a 3 cm diameter housing. Using inserts instead of a solid probe would allow for the housing assembly to be reused while insert plates would be swapped out when a fresh collection surface is required. The initially proposed collection plate insert design is presented in

Figure 18. The insert cross section is trapezoidal such that the holder captures the plate across the full length. The alignment hole seen at the base of the plate is offset from the center so that each collection face will use a unique set of inserts. Unfortunately, the plate inserts and housing designs suffered from cracking or mechanical failure during exposure in DIII-D. As a result, the solid 3 cm designs shown in Figure 17 were determined to be more robust and able to withstand the expected exposure conditions at the cost of more initial stock material as well as additional machining costs.

Collecting isotopically enriched and natural carbon on a graphite collector probe presents a unique challenge for sample analysis following the methane injection experiments. If ion beam techniques and LA-ICP-MS surface characterization are to be performed across the collector probe faces, some sort of depth marker is required to assist in distinguishing what is deposited on the collector probes from the carbon material within the probe stock material. Previous NRA analysis and SIMNRA simulations along with the material constraints for what is allowed in the vessel of DIII-D have been compiled to select silicon as the probe coating material. Simulations show that a minimum thickness of 4 µm is sufficient for characterization with NRA and LA-ICP-MS. It is expected that the NRA detection limit will be ~1e16 atoms/cm^2. Simulation results are shown in Figure 19 for a deposited layer consisting of 0.45:0.45:0.1 - C12:C13:D on a graphite substrate with and without the Si layer. The plot shows NRA measurements for a graphite surface with and without the silicon layer. As shown in the case with silicon, the peaks in the spectrum for carbon are thinner and lower in magnitude. This means that the background or stock material graphite no longer contributes to the carbon measurements of interest. Therefore, any measurements of the collector probes that are taken after exposure during methane injection experiments would be representative of the deposits collected during exposure at DIII-D.

A physical vapor deposition tool has been used to evaporate high purity silicon across the surface of both collector probe sets for the methane injection experiments. Following the ORNL 3500 cleanroom standard operating procedure for deposition originally resulted in delamination of the silicon coating across the graphite surface of the collector probes. Increased silicon adhesion was achieved through a series of surface preparation tests as well as using a newly purchase heating element to increase the collector probe surface temperature during thin film deposition. Newly machined collector probes now go through a series of processes that clean and prepare the collection surfaces for silicon deposition. Previously the probes were coated without any surface preparation. Probes that were delivered from the machine shop were simply coated in silicon. Plasma etching, sand blasting, and tape liftoff of the probe surfaces have all been shown to increase the adhesion properties of a silicon layer. Etching the probe surface using an oxygen plasma followed directly by tape liftoff has been shown to be the best combination for preparing the probe surface for thin film deposition. Energy Dispersive Spectrometry (EDS) has been used to evaluate the adhesion quality of the different surface preparation methods by measuring the surface silicon concentration following an attempt to remove the deposited silicon layer using tape liftoff. With the newly developed surface preparation methods, as high as 75% surface silicon concentrations have been measured with EDS. The previous methods which suffered from delaminated silicon resulted in less than 1% surface silicon concentrations. Examples of the new silicon coatings are shown in Figure 19.

After review with the vacuum committee specialists at DIII-D, no issues with using a silicon coating across the probe surface have been identified. Baking of the probes up to ~1000 ^{o}C, prior to in-vessel exposure, is required in order to remove any surface contaminants that may remain. This baking process is also believed to have the added benefit of relieving any residual stress in the silicon layer that result from the deposition process.

While the MiMES station has previously been equipped with collector probes, a design review was not necessary for the incremental changes made with the new collector probe design (MCP) in Figure 17. DiMES has never been adapted to insert collector probes into the lower divertor of DIII-D, so a more rigorous process was required to develop and certify the DCP design prior to the methane injection experiments. As seen in Figure 20 there is approximately 7 cm between the top of a standard DiMES sample and the bottom of the DiMES gate valve to the DIII-D vessel. Within this space, there are deductions from the 7 cm maximum for installation and removal of the collector probes and other samples that are installed on this station. What remains is 4.5 cm of available space above a standard DiMES sample to be used as a limiting dimension for the exposure length of the DCPs.

In order to expose a collector probe 4.5 cm above a standard DiMES samples, a new collector probe assembly is required as this is shorter than those which are exposed with MiMES. Any new diagnostics designs and concepts at DIII-D call for a design review process. As shown in Figure 17 and Figure 21, a new design was developed for this process. The proposed DCP assembly incorporates a standard DiMES head shape that is machined from 99.5 % alumina (Al_2O_3). This alumina ‘cap’ has threaded holes in the base of the design such that the insulation cap is fixed to a stainless-steel adapter that allows for installation of the assembly to the DiMES drive. Within the alumina, a 3 cm diameter solid ATJ collector probe is installed for insertion into the vessel during the methane injection plasma discharges. The design takes advantage of pre-existing DiMES operation procedures.

Concerns with this design include disruption induced forces causing stresses that would exceed ATJ tensile and compressive limits along with temperature evolution of the assembly during exposure to the plasma SOL. Estimates of the disruption forces have been provided by a disruption expert at General Atomics and they are summarized in Table 3.

Applying these forces in stress simulation software has shown that the probe can survive operation within DIII-D. However, in the case of insulation breakdown, the probe is likely to fracture. Thermal modeling of the probe surface has also been performed in ABAQUS. This software using finite element analysis to simulate the behavior of the collector probe assembly under representative plasma exposure conditions. Several simulated cases were performed on the DCP with heat fluxes which were previously measured during experiments on DIII-D. The results suggest that probe exposures would result in collector probe surface temperatures that are below the DIII-D administrative limits for ATJ graphite at 1600 ºC. Heat flux calculations using Thomson Scattering measurements near the crown result in 3.5 MW/m^2 impending on the probe tip between the 4-5 cm flux surfaces. After 5 seconds of exposure, the peak probe temperature is ~1100 ºC or well below the administrative limit. If the probe is exposed to a transient event, the thermal simulations show that the probe may exceed the 1600ºC limit. This has low impact on plasma operations considering it was agreed that probe sublimation is not a concern. Following the methane injection experiments, all probes survived exposure into the plasma. Even recently when the MCP design was inserted nearly into the core of DIII-D, the probe surface simply ablated. No probes exposed during this run campaign have failed mechanically and fallen into the device.

Additional details for the diagnostics review process are available at the DIII-D internal webpage under the system title “DiMES: Collector Probe”. Several documents were assembled to assist in this process as well as presentations. All are assembled including a conceptual, preliminary and final design review. Supporting notes and documents include a full description of disruption force analysis, material property data sheets for the various materials used in the design, references for graphite contact resistances, and references to assist in certifying the insulating alumina components.

2.3 Methane Injection

Isotopically tagged methane, $^{13}CH_4$, provides mass distinction from the natural carbon or graphite that is used in the construction of the first walls of DIII-D. As seen in Table 2, it fits the criteria for an ideal tracer material and provides insight into non-recycling material transport. Isotopically tagged methane can also include deuterium in place of standard hydrogen ($^{13}CD_4$) in order to match the main ion species used in experimental fusion plasmas. Bottles of this gas come at 99 % standard purity from Sigma-Aldrich. This determines the isotopic purity and means 99 atom % of the carbon is ^{13}C and 99 atom % of the hydrogen isotopes is deuterium. The vessel puffing system on DIII-D has a methane regulator and lecture bottle setup dedicated for methane use, so there is no need to provide any additional hardware modifications during the methane injection experiments.

There are many available gas injection locations around the DIII-D vessel including those seen in Figure 22. Single point or local injection of gasses has a largely perturbative effect on the plasma stability. Gas locations shown in the bottom half of the vessel are therefore not as attractive as those with multiple injection locations that are toroidally symmetric around the vessel. The Upper Out Baffle (UOB) gas puffing system was selected for these experiments. The UOB system injects methane into a pumping plenum at three equidistant toroidal locations around the top of the vessel. When the pumps are turned off in this plenum, gas fills the cavity and is introduced into the plasma vessel through an aperture as is shown in Figure 16 and Figure 23. Injection of methane in this manner introduces impurities near the outer strike point of upper single null plasmas as a toroidally symmetric source of impurities. This avoid local injection and mimics impurity introduction that is similar to the metal rings campaign where impurities were introduced through erosion of the metal tiles at the outer strike point location.

A goal during these experiments is to determine a methane injection rate which provides sufficient isotopic carbon content to the plasma and results in detectable deposition across a collector probe surface as measured by LA-ICP-MS and NRA while also minimizing plasma perturbation. These impurity source rates will also mimic plasma material interaction events and require a conversion of gas flow rates to the number of atoms/second that are introduced into the vessel. This will allow for the comparison of known sputtering rates to the calculated injection rate of methane.

Calculations for the upper outer plenum aperture are needed. First, the gas entrance area calculation requires the reactor coordinates for the plenum aperture. Through DIII-D's EFIT viewer, two points are selected at the furthest location in-vessel of the outer plenum aperture such that the height and radial location are obtained. These locations are $R1, Z1 = 1.373, 1.310\, m$ and $R2, Z2 = 1.373, 1.348\, m$. The radial location $R = 1.373\, m$, and the difference between $Z1$ and $Z2$ determines the height of the opening from the plenum at $0.038\, m$. The continuous toroidal extension of the plenum over $2\pi R \sim 8.627\, m$ leads one to find that there is an upper outer plenum aperture gas entrance area of $A_{uopa} = 0.328\, m^2$.

Using 5 Torr-L/sec as an example flow rate, we can now focus on the calculation of the injection rate through the entrance area A_{uopa} in order to establish the influx density of methane into the vessel. First, convert Torr-L/sec to molecules/sec with the simple conversion for throughput of 1 Torr-L = 3.239 x 10^{19} molecules at room temperature (PV=NkT) and a Boltzmann constant of k = 1.0356 x 10^{-22} Torr-L/K. With this conversion, 5 Torr-L/sec is equivalent to 1.620 x 10^{20} ^{13}C/sec. After combining this value with the A_{uopa} one obtains an influx density of ~4.94 x 10^{20} ^{13}C/m^2/sec.

Startup shots were needed in order to optimize the $^{13}CD_4$ gas flow rate for these experiments. During the startup shots, a maximum gas flow rate of 14.3 Torr-Liters/s was selected. This rate of gas injection maximizes the ^{13}C deposition on a collector probe while maintaining the plasma integrity. During startup, only the MCP was available to test the flow rates and collect impurities during gas puffing. The collector probes exposed were determined to collect a sufficient amount of enriched carbon deposits to be distinguishable from the natural carbon in the device. Spectroscopic systems also verified that the injected methane was introduced into the plasma and able to escape the divertor.

2.4 Experimental Planning

The experimental plan was developed to accommodate the needs of several proposals. Originally a single day was allocated for the experiments. This day would be split into two half days. One half day would operate DIII-D in forward B_T and the other half day in reverse. With an upper single null shape, similar to that shown in Figure 24, the four hours for each half day were dedicated to running a series of diagnostic shots that would assist in developing background plasmas for different modelling efforts. Following the diagnostic phase, a series of collection phases occurred. The collection phase exposed collector probes to methane injection using the plasmas developed in the diagnostic phase. Experiments were performed in this order to accommodate the diagnostic requirements for developing a background plasma while also performing strike point sweeps in the initial phase. During the second phase, the strike points were stationary and diagnostics were swapped to include collector probes.

The experimental upper single null shape was originally based on an elongated plasma shot 179658 with the shape control points modified in order to limit the gap between the plasma crown and the lower divertor. With the plasma closer to the DiMES drive, there is a greater probability of the DiMES collector probe being able to sample impurities in the crown of the SOL. Considering we wish to collect as much of the puffed $^{13}CD_4$ as possible, closing this gap is vital. The 2016 Metal Rings Campaign has shown that exposing collector probes at a distance of 5-7 cm from the separatrix (at the outboard midplane) is optimal for collecting impurities within the far-SOL. This experience with MiMES collector probes produced a measurable amount of impurity content along the face of the probes while minimizing the surface exposed to the re-erosion zone. As we see in the EFIT reconstruction for the example shot of Figure 16, the 2-3 cm flux surfaces are brought down in these experiments in order to intersect the DCP collection surface. Therefore, the 5-7 cm surfaces can also easily be positioned over the collection area by reducing the plasma elongation in the crown. One should note that it is desirable to produce an upper single null plasma where the flux surfaces in the SOL crown do not limit on the lower divertor of DIII-D. Instead, the flux surfaces intersecting the collector probes should be shaped in a manner that allows for the field lines to clear the lower divertor and limit on the targets in the upper divertor. This clearance allows for the DCP to have a larger plasma sampling volume that is not immediately limited due to the geometry of DIII-D. Several dedicated shots were also dedicated to developing this shape.

With shape and puff rates established, background plasma ‘diagnostic’ shots are run at the beginning of each experimental half-day in order to reproduce the plasma in OSM for DIVIMP simulations of the impurity density profiles during the methane injection experiments. Strike point sweeps combined with Langmuir probes and divertor Thomson scattering measurements provide electron temperature (T_e) profiles at the target surface as well as plasma density and temperature measurements above the target. These measurements are direct inputs into the OEDGE and OSM models in order to reproduce the background plasma for the experiments where target conditions from Langmuir probe measurements are used to match the upstream Thomson profiles.

Following the diagnostic phase, reciprocating probes are retracted and equipped with collector probes on both the MiMES and DiMES systems. This hardware exchange requires accounting for an approximate forty-minute period between the diagnostic set of shots and the collector probe shots. From this point, plasma discharges occur at a pace of twenty minutes in-between shots. This will allow for the DiMES and MiMES collector probe inserts to be replaced with new collector probes while transitioning to new plasma conditions. There is also a need to optimize density control during the collection shots. This means that during the time between shots, glow discharge cleaning (GDC) is performed before the next plasma. In theory, the glow discharge removes potential contaminants from the wall and ensures a clean plasma for each collection pulse. This translates into six or seven shots with twenty-minute gaps and twelve-minute glow discharges that are all preceded by a set of background shots with a forty-minute gap time.

To summarize, the shot shape during the methane injection experiments is defined as upper single null with L-mode characteristics. The first day of shots will be in forward B_T which correlates with unfavorable ∇B drift in upper single null. This will result in the $E_r x B$ drifts directed towards the high field side or inner stack of DIII-D. Proposals incorporated in the experiments requested a consistent electron density (n_e) across all shots while others have requested a range of injected powers as well as varying outer strike point positions. This decision places the outer strike point at the outer corner that is closest to the puffing location for a majority of the shots with the final plasma discharges holding the outer strike point at the inner corner near the dome.

Day two is comparable to day one, however, the direction of B_T was be reversed in order to have an H-mode favorable set of data. As we reverse the flow, the $E_r x B$ drift also changes and is directed towards the low field side of the device. During day two, the outer strike point is at the outer corner and inner corner, but the general goal was to match conditions from day one while changing the toroidal magnetic field direction. Density control is also accomplished through the deuterium puff rate and cryopump rate in order to match the density of day one.

Further experimental planning was required outside of the original proposal. While plasmas were completed in both forward and reverse B_T, the power scan was not completed on days one and two. DIII-D director’s reserve time was made available to fill this gap resulting in an additional day of run time for the methane injection experiments. During the director's reserve shots, plasma conditions were in forward B_T or the unfavorable direction. The experiments on this day were performed with L-mode plasmas at electron densities of $n_e = 2.5x10^{19}\ m^{-3}$. Injected power was varied from 2.5 – 4.5 MW. Collector probes during the initial set of experiments suffered from delamination of the deposited silicon surfaces which caused issues with sample analysis. A new set of collector probes were developed for the director's reserve experiments using techniques that resulted in improved adhesion of the surfaces. This second set of experiments also planned to use a control probe which was exposed without any injection of methane. This new series of shots and probe inventory has proven to be critical to the analysis presented in the results section of this dissertation.

2.5 Future Considerations for Helium Plasmas

Traditionally, DIII-D plasma discharges are run with a main ion gas of deuterium. As mentioned in earlier sections, sputtering due to ion collisions with plasma facing components results in material liberation. In the case of a carbon environment (DIII-D) being bombarded by hydrogen, chemical sputtering is heavily responsible for the introduction of carbon impurities. There are, however, other options for plasma fuel on the DIII-D device. Helium is an example of a gas that has been used previously and one that could provide several advantages over deuterium.

Several experiments on JET and DIII-D have tested the changes in plasma behavior when using helium fueling [35-38]. Figure 25 highlights the findings of DIII-D discharges that used helium and deuterium fueling without any other changes to the plasma operating conditions. Spectroscopic measurements at various poloidal locations show that the carbon density dramatically drops when using helium plasmas. This drop-in background signature would assist the measurements for the proposed $^{13}CD_4$ measurements. Helium operation would also remove the complicated molecular processes of deuterium plasmas which may cause discrepancies in the fluid models used for these experiments. While the signatures decrease, physical sputtering will also contribute to the carbon background but at a much lower level compared to the chemical and physical sputtering combination.

L-mode operating space has also been found to increase with helium plasmas. In particular, the L-H mode transition threshold power increases by ~50% with helium. Low charge exchange rates and L-mode density limits also increase by a factor of 2-3 in helium when compared with equivalent deuterium fueled plasmas. This is another major advantage to the proposed experiments due to the request for a density sweep in L-mode.

While there are several pros of using helium, there are of course some caveats. A higher main ion mass will change transport terms in simulation, but it has not been evaluated as to how much of an impact this will have. Careful wall conditioning is also required which has previously included a 16 hour bake prior to running experiments on DIII-D. The bake ensures that helium is the dominant fueling species (~90%) in the plasma discharge through removal of wall retained deuterium. Neutral beam injector (NBI), which are used to provide plasma heating, should also be converted to use helium during operation in order to maintain high helium purity. These steps are only necessary when it is of interest to have a pure helium plasma. There may still be benefit to running a helium plasma without the beams and only some baking. This 'dirty-helium' scenario could still assist in the measurements during the $^{13}CD_4$ campaign. While this operating scheme was not folded into the experimental plan, it is worth consideration for future experiments that plan to use carbon impurities for isotopic tracer experiments.

2.6 Diagnostic Preparation for Impurity Measurements on DIII-D

Collector probes are valuable tools for evaluating non-recycling impurity transport within the SOL, and they have shown to be successful in sampling isotopic impurities in the far-SOL of DIII-D. This work uses a pair of collector probes in order to infer regions of increased impurity density within the near-SOL. With two collector probes, we are able to increase the poloidal resolution of our direct SOL sampling experiments when compared to the 2016 Metal Rings Campaign. Collector probes used in these experiments have a wider collection face in order to improve the width profiles upon the collector probe surface while still having the capability for the collection of deposited impurities along the length of the probe. The MiMES and DiMES collector probes that are discussed in this dissertation are of a solid design based on the design reviews at DIII-D.

Personnel are required during the use of the collector probes in order to exchange the DCP and MCP during a pit run between shots. Twenty minutes between collection phase shots allows for this transfer to a new sample and has proven to be straightforward and efficient when enough forethought is in place. An inventory of ten collector probe sets, including both an MCP and DCP for a unique plasma condition, were prepared and shipped to DIII-D. The probes were etched with a unique identifying number in order to assist in keeping track of the probes. Adjustable length shipping tubes were purchased from McMaster-Carr to protect the individual probes while in transit (product number 21081T147). Stickers were places on the shipping containers to match the etched value on the probes. Foam was also placed into the ends of each container in order to protect the ends of the probes and hold the probes centered while in transit. This protected the deposited silicon layer when shipping to DIII-D as well as the deposited impurities following exposure. Four-liter clear containers from the Really Useful Box ® company were used to ship the inventory of collector probes once prepared.

A spreadsheet was made in Google Sheets to keep track of the probe exposure conditions, probe location, and remaining inventory. There is also a flat orientation face at the base of each collector probe maintains the proper position of the probes during exposure. When analyzing the results from the DiMES and MiMES collector probes, the centerline scans provide valuable insight into the carbon deposition profiles. Scans of the carbon profiles and the associated contributions from both ^{13}C and 12C to the elemental profiles are of great interest. Areal density measurements provided by NRA have assisted in providing calibrated estimates for the deposition magnitude across the probe surfaces. Results from this set of experiments continue the valuable work completed during 2016 Metal Rings Campaign and provide new tools for the upcoming impurity transport experiments such as SAS-VW.

The theoretical impurity trap can be better characterized with a pair of collector probes in the SOL. Figure 26 describes three potential regions for an impurity accumulation that these probes sets would be able to infer. Each region is noted by a colored section of the SOL. According to simulations and theory, the orange and yellow portions are potential locations for the SOL impurity accumulation in an unfavorable $B \times \nabla B$ drift configuration when operating an upper single null plasma. If an accumulation were to occur in the orange region, then one would expect greater content on the ITF sides of both the DiMES and MiMES collector probes. This expectation is supported by the results from the initial metal rings campaign. In the yellow region, the MiMES collector probe would again have greater content on the ITF side; however, the DiMES collector probe ITF/OTF total content ratio would likely drop below 1 due to the greater levels of impurity deposition that would appear on the OTF side. It is expected that the accumulation region will shift to somewhere between the outboard midplane and the outer target when the direction of the magnetic field is changed from forward to reverse in upper single null; this region is indicated in green. A change in accumulation position can be seen on the probes via greater content on both OTF portions of the probe. Therefore, having two collector probes can allow us to hone in on the position of the accumulation with greater fidelity. The challenge lies in positioning the relevant SOL flux surfaces onto the exposed 4.5 cm of the DiMES collector probe. The flux expansion is much greater in the crown plasma, so the impurities that travel along the flux surface will be sparser in comparison to the probe counterpart at the MiMES location.

Once removed, the probes are analyzed with LA-ICP-MS in order to characterize the collected carbon on the probe surfaces. Previous method and techniques have been developed so that we can obtain 2-D surface maps of both elemental and isotopic tungsten content along the probe. This method development has proven to translate well to carbon analysis when using the same techniques. Initial measurements of carbon indicated that the ^{12}C and ^{13}C background is relatively constant within the ICP-MS detectors during data collection with low relative standard deviation (RSD%) of ~3%. This background can be subtracted during a time resolved analysis as shown with tungsten isotopes in Figure 27.

The background is averaged across the initial time period and then subtracted from the signal obtained in the 'valid data' region of the plot. This can be repeated across each isotope and then a time resolved elemental signature can be generated by summing the intensity from each of the isotopes together in the individual time bins. 2-D maps are produced by repeating line scans across the surface of a probe's collection face. An example of both elemental and isotopic 2-D plots is shown for tungsten in Figure 28 [23].

LA-ICP-MS measurements of samples that were exposed on August 13, 2008 during DIII-D methane injection experiments confirm that the technique is capable of distinguishing enriched deposits of ^{13}C across a sample surface. The probes were exposed to shots 134580-134597 for a total of 18 repeat exposure shots. These were upper single null H-mode with ~7MW of NBI power. The tip of the probe shield was at R=232 cm, which equates to 8 cm outside of the LCFS. Figure 29 shows that the fraction of enriched ^{13}C is quite low in the measurement, nonetheless enrichment is still detected across the probe surface. There was no barrier between the deposited material and the probe graphite, so a uniform pre-exposure coating will assist in distinguishing the ^{13}C that was deposited versus the naturally abundant ^{13}C in the probe material. Addition of a coating will increase the enrichment fraction value considering there would be less contribution of the naturally dominant ^{12}C (Table 2) to the measured signal of the deposit by LA-ICP-MS.

Additional assessments of the deposited material across the probe surfaces are provided by Ion Beam Methods. NRA is the ideal method for detecting low-Z isotopes. The added capability of distinguishing ^{12}C from ^{13}C is attractive for these studies. SIMNRA is a software capable of providing analysis of the NRA spectra. UTK, MIT, and Sandia National Laboratory have ion-beam laboratories that have previously provided tungsten measurements using RBS. Unfortunately, some labs do not allow for tritium contaminated samples into their laboratories. Therefore, carbon measurements via NRA are limited following exposure in DIII-D. Sandia National Laboratory (SNL) is able to provide the measurements with their ion beam facility. The 2016 Metal Rings Campaign collector probe measurements by RBS were completed at this laboratory, and publications by Wampler et al. have also shown they are experienced in NRA measurements and analysis of ^{13}C [20-22]. Considering the LA-ICP-MS measurements will locally ablate the probe surface material, NRA measurements should occur prior to those with LA-ICP-MS.

Spectroscopically, there are diagnostics whose data is indicative of increased impurity density throughout a plasma on DIII-D following methane injection. MDS measurements at various locations in the crown of DIII-D were originally of particular interest. The lower divertor or crown of an upper single null plasma has several lines of sight that could provide time evolved density measurements of CV. The significant indicator of an accumulation would be to compare the relative intensities of side by side CV measurements in order to show an increase in the measured CV signature that then decreases in the neighboring lines. This local maximum in the density profile would indicate an accumulation of impurities in the crown SOL of DIII-D and confirm the long-standing hypothesis in cooperation with the asymmetry measurements on the collector probes.

While the collector probes are a fantastic method for isolating the position of the impurity accumulation, there has been a recent focus that emphasizes how ion flow velocities play a role in determining the position of an impurity accumulation. This sort of theory would greatly benefit from additional spectroscopic measurements in the SOL by CIS. While the accumulation is typically thought to exist in the near-SOL, modeling reconstructions of edge flow suggest that a force null in the far-SOL occurs in the same poloidal position as in the near-SOL. XGCa simulations (Figure 30) show kinetic simulations with poloidal alignment of the near and far-SOL stagnation points. While flows are opposite in direction in the two regions of the SOL, the parallel accumulation is again in the same poloidal position.

Using CIS measurements, one could see the poloidal position of the impurity accumulation and compare to the relative intensities of the deposited content on the two collector probes in order to verify the existence of the impurity accumulation. However, this measurement is dependent on observed brightness. Typically, in the vessel crown, brightness can be an issue. Therefore, 2-D velocity maps are typically limited to regions closer towards the divertor. Increased density has intuitively been observed to increase the brightness in the measurement. Fortunately, the proposed shot plan includes several high-density shots in both Forward and Reverse B_T . In the case where there is not enough brightness in the crown region, one can often infer the location of the flow reversal through the velocity measurements in other regions. The faster lower divertor camera was expected to be available during the experiments and this has not yet been used in great detail with upper single null configuration plasma discharges that are interested in impurity flows. This measurement along with the two others would make a strong case for impurity accumulation. Comparisons between the various planned plasma conditions will provide indications of scenarios that are favorable for this accumulation as well.

2.7 Non-Recycling Impurity Particle Balance

The near-SOL impurity content is of primary interest to the fusion community due to the boundary condition that it sets for impurity content in the plasma core. For future fusion reactors, it is ideal that we minimize the concentration of impurities in the near-SOL. Our set of experiments modify plasma conditions and drift parameters so that we may observe changes in the impurity profiles. Through these modifications it is expected to observe variations in the SOL impurity profiles. In an attempt to characterize the changes produced in the impurity profiles, a non-recycling impurity particle balance is often used. This balance is presented here as a conceptual walkthrough of how one may consider impurity transport from one portion of plasma to another. This particle conservation balance considers the previous plasma particle balance work and uses reservoirs in order to model the movement of impurities from one distinct region of plasma volume to the next [39-42]. These reservoir models are based more on experimental observations rather than fundamental theory as described in section 1.4. Therefore, this section will focus on carbon evolution following methane injection near a divertor target and some experimental observations which would be of interest in analysis for individual reservoirs. The results and discussion chapter of this dissertation focus on the two SOL reservoirs and the relationship between the two. Codes such as 3DLIM and DIVIMP are used along with collector probes in order to elucidate details of the impurity transport processes through these reservoirs.

Five reservoirs are considered for this balance in the form of the vessel targets, near-SOL, far-SOL, vessel walls, and plasma core reservoirs. The particle balance models often take the observed residence times and densities for different carbon emission lines in order to solve a system of equations that relate one reservoir to another. This accounts for the number of particles that are injected using the upper outer baffle gas puffing valves and then follow the particles as they are passed from the point of injection to throughout the plasma before interacting with a solid surface or pump. A simplified depiction of these processes is shown in Figure 31.

Measurements of carbon can support these models and are provided by the suite of diagnostics that are available on DIII-D. Table 1 shows there are six possible ionization states of carbon, and in the tokamak environment, temperatures are high enough to expect each throughout the plasma. DIVIMP modeling in Figure 32, has shown the different regions where each of the carbon charges states are expected to occupy throughout a representative plasma on DIII-D. The simulations are based on lower single null plasma shapes with 3 MW L-mode conditions in reverse B_T, and models for CH molecular dissociation as well as impurity ExB drifts were turned on in the simulations. Methane was fed into the simulation at the outer strike point with a rate of 10 Torr-L/s, which is equivalent to ~3 x 10^{20} ^{13}C atoms/second. When puffing $^{13}CD_4$ into the plasma outer strike point, the models predict that neutral carbon and carbon ions up to C3+ predominantly populate the divertor region. Throughout the SOL plasma, C4+ is the dominating charge state near the core. C5+ and C6+ require an extreme jump in energy to reach these ionization states. Threshold energies of 392.087 and 489.993 eV are needed to generate these forms of carbon, and this is relatively high compared to the C3+ and C4+ energies of 47.888 and 64.494 eV. As seen in the simulation, the high carbon charge states are generated in the most intense portions of the plasma. These regions are the core as well as segments of the near-SOL.

The color bars on the plots in Figure 32 give one a sense of how the puff signal will compare to the background carbon that is generated from a full graphite device such as DIII-D. All color bars list 1e17 as the relative maximum across each plot. This leads us to expect a nearly 50 % difference between the background carbon signatures and the carbon that is puffed into the system at 10 Torr-L/sec. In the simulation, the puffed carbon rate should increase the signal within the plasma at a linear rate. Now that we know which charge states of carbon exist in the various regions throughout the device, we can establish which diagnostics are best suited to monitor carbon in various reservoirs.

Beginning at the point of introduction for impurities, there is the divertor region. Injection of methane in a toroidally symmetric fashion will complement modeling using DIVIMP considering the code utilizes toroidal symmetry. The injection scheme will also mimic the erosion processes that occur in the divertor regions of the plasma. The equation for this region is shown in the following:

$$\frac{dN_{div}}{dt} = \Phi_0 + \frac{N_{nSOL}}{\tau_{nSOL}}\left(2f_{\parallel,nSOL}\right) + \frac{N_{fSOL}}{\tau_{fSOL}}\left(2f_{\parallel,fSOL}\right) - \frac{N_{div}}{\tau_D} - \frac{N_{div}}{\tau_{pump}} \qquad 2.1$$

The original source of impurities (ϕ_0) is injected into the upper outer plenum aperture of DIII-D through the UOB puffing system in order to introduce an isotopically tagged source of non-recycling impurities into the outer leg of the SOL. Gas injection during our experiments of interest is achieved at a rate of 14.3 Torr-L/sec which is equivalent to ~5 x 10^{20} ^{13}C/second. Considering UOB's aperture dimensions, this is equivalent to ~15 x 10^{20} ^{13}C/m^2/second. This source (ϕ_0) will then leave then leave the divertor region based on the divertor residency time (τ_D). In order to quantify this parameter, DIII-D is equipped with mass flow controllers that will modify the input flow rate to the user specification. Time evolution of the divertor methane inventory can then be monitored using the gauges available on DIII-D [13, 43]. Pumping at the divertor (Figure 23) may be used for plasma density control, so a term for the removal of particles by pumping is added to the divertor equation based on the pump time (τ_{pump}). This term is zero when the cryopumps in the gas puffing baffle are turned off. During the methane injection experiments, it is assumed that the outer cryopumps next to the UOB puffing system are not operating during the experiments in order to allow the injected impurities to enter the plasma. These particles may also encounter regions of flow that are directed back towards the divertor. These near and far-SOL terms ($\frac{N_{nSOL}}{\tau_{nSOL}}\left(2f_{\parallel,nSOL}\right)+\frac{N_{fSOL}}{\tau_{fSOL}}\left(2f_{\parallel,fSOL}\right)$) are added to account for such instances. Each term has a near and far-SOL fraction that accounts for parallel motion along the field lines, which will eventually terminate in the divertors. Considering the parallel motion is towards both the inner and outer targets of the plasma, a factor of two is included in the equations. Further discussion of these remaining terms is presented in subsequent sections.

Once impurities are introduced into the plasma via gas puffs at the divertor target, it is assumed that the impurities disassociate and ionize in the near-SOL, but this needs to be characterized. In effect, the gas puff efficiency (η_{puff}) may be determined by observing the low charge state densities in the reservoir which would tell us how much of the gas puff is effectively entrained in the plasma relative to what is injected. This reservoir is closest to the core of the plasma and has a high temperature gradient that typically dominates the impurity force balance. The gradient results in parallel flow that is believed to drive the impurities up and away from the targets. Eventually, there is a null point in the forces acting on impurities. This null causes impurities to accumulate in the direction of parallel motion causing increased impurity density in the near-SOL reservoir. This dissertation uses the DIVIMP code to again simulate the SOL impurity density profiles described here. Diffusion and turbulence are thought to control the perpendicular motion that results in core contamination and radially outward motion towards the far-SOL and walls. Inward motion may also have contributions due to an inward 'velocity pinch' [44]. Considering the near-SOL is the first line of defense against contamination of the core that causes cooling, it is of interest to reduce the near-SOL impurity density. Equation 2.2 describes this set of processes.

$$\frac{dN_{nSOL}}{dt} = \frac{N_{div}}{\tau_D} + \frac{N_{core}}{\tau_p} + \frac{N_{fSOL}}{\tau_{fSOL}}(f_{\perp,fSOL}) - \frac{N_{nSOL}}{\tau_{nSOL}}(2f_{\parallel,nSOL} + 2f_{\perp,nSOL}) \quad 2.2$$

As has been previously referenced, injected impurities can travel to the SOL after introduction through the divertor reservoir ($\frac{N_{div}}{\tau_D}$). These particles will have some probability to exit from the SOL into three different regions of the plasma volume. These regions include the core, divertor reservoir, or far-SOL. After impurities spend time in those sections, additional SOL contributions from such reservoirs are accounted for in the model. The most deleterious option on plasma performance is for SOL impurities to enter the core of the plasma and cause cooling through radiative processes ($\frac{N_{nSOL}}{\tau_{nSOL}}(f_{\perp,nSOL})$). SOL impurities could also travel back to the divertor regions via a 'watershed' effect ($\frac{N_{nSOL}}{\tau_{nSOL}}(2f_{\parallel,nSOL})$) where flow between the target and watershed formation due to over-ionization drives impurities towards the target. Upstream of the 'watershed' impurities are driven away from the target or further upstream. Alternatively, transport could even be radially outwards towards the far-SOL and wall ($\frac{N_{nSOL}}{\tau_{nSOL}}(f_{\perp,nSOL})$) where collector probes are used to sample impurities in transit during the methane injection experiments, another key focus of this dissertation. The share of particles which leave the SOL via core and wall routes may re-enter the SOL ($\frac{N_{core}}{\tau_p} + \frac{N_{fSOL}}{\tau_{fSOL}}(f_{\perp,fSOL})$).

In order to account for these paths of travel as well as the magnitude of each relative to one another, they require this weighting parameter, f, that can modify the terms through experimental observation. Parallel motion of impurities directed up the temperature gradient and along flux surfaces is believed to greatly dominate over the cross-field motion in the near-SOL. Therefore, it is traditionally assumed that parallel motion is much greater than perpendicular contributions on impurities. Impurities are still entering the plasma, however. This means that perpendicular motion cannot be unaccounted for in this particle balance description.

As noted in the literature and Figure 33, perpendicular anomalous diffusion is low in the first few mm of the SOL but grows further into the far-SOL [45]. This helps us define the boundary between the two and can determine the width of each reservoir. The near-SOL is further characterized by a steep gradient of the parallel heat flux profile while the far-SOL has flatter heat flux profiles. The near-SOL is typically only a few cm from the separatrix while the far-SOL extends several cm in length out to the limiting walls. One example from determining the reservoir width may see seen on C-MOD. The radial density profile is used to define the point of division between the near and far-SOL. Typically, the break in slope of the density is used to distinguish between the two as shown in Figure 34 [46].

Similar radial measurements are available on DIII-D using the midplane reciprocating probes during the shots that are prior to those which will utilize collector probes. Radial density profiles may define the width of the near and far-SOL for the models. Diffusion coefficients may also be used to estimate the cross-field velocity through the relationship in the following equation.

$$v_{\perp} \cong D_{\perp}/l_{\perp} \tag{2.3}$$

Using Alcator C-Mod as an example, the cross-field velocity is estimated with $l_{\perp} = 0.005\,m$ and $D_{\perp} = 0.1\,m^2/s$ in order to evaluate $v_{\perp} \cong 20\,m/s$. In comparison, the relative magnitude of the parallel velocity should be considered. Mach probe measurements are one of the tools that may provide this sort of data in the near-SOL and measurements up to 40 km/s are not unusual in this reservoir. While these velocities are quite different in magnitude, so is the distance over which the particles will travel in each respective direction. Perpendicular distances have already been evaluated to be on the scale of several millimeters, but the parallel distance is going to be on scales that are synonymous with the connection length. Typical values for the connection length are on the order of several tens of meters in the plasma edge. One must realize that the ‘parallel’ direction is a bit more complex than simply following the separatrix on a 2-D plasma reconstruction such as those in Figure 32. Instead, this problem requires 3-D consideration. One must look at field line reconstructions similar to those in Figure 35. Here we see the connection length, or the distance along B in the SOL that is required to reach a solid surface for a collector probe at the outboard midplane of DIII-D. Connection length profiles may be calculated using the MAnifold and FOotprint Tracer code, MAFOT [47]. This code is able to take a plasma from DIII-D and other devices to perform field line traces from a given launch point towards the nearest limiting surfaces. This provides the distance between a collector probe and the walls which is shown to be strongly correlated with the impurity deposition profile.

For the purposes on the reservoir model, we can use the fundamental equation for estimating the connection length as follows.

$$L \cong \pi R q \tag{2.4}$$

Where q is evaluated as:

$$q \cong \frac{rB_{\phi}}{RB_{\theta}} \tag{2.5}$$

Standard divertor configuration on DIII-D would then result is typical connection length values of ~20 m which is 4000 times longer than the 5 mm width that is used to define the near-SOL. So, in order to travel 20 m at 40 km/s, it would take ~500 µs. Similarly, in order to travel 5 mm at 20 m/s, 250 µs is required. But, the parallel motion we just calculated is only moving particles through the reservoir and not out. The flow reversal near the targets that occurs due to a watershed requires consideration of the flows near the target and an estimate of how many particles are directed towards the target versus up the ion thermal gradient. With this in hand, each weighting factor, f, may be established. For now, the perpendicular portions are considered equal due to isotropy. Parallel motion due to the watershed requires a bit more thought on how to weight the motion in comparison to the cross-field, near-SOL motion.

In order to track this reservoir on DIII-D, DIVIMP simulations in Figure 32 show that the near-SOL content may be observed with measurements of C4+. When referring to the NIST atomic spectra database for CV lines (spectroscopic notation), there are 149 lines with available data. Of these 149 lines, 11 have been observed and recorded; the other lines are theoretical. MDS, SPRED, and CER can all provide the needed measurements of CV, and their view chords are shown in Figure 36 on top of an upper single null plasma at DIII-D, shot #171553.

Several issues arise with the CV lines of sight and available emission lines. The DivSPRED line of sight is only limited to looking directly over DiMES, through the core, and near the outer edge of SAS. Line integrated measurements will view C4+ throughout the whole line of sight and will be limited to observing CV or an accumulation that happens to fall directly within this region. The CER lines are a bit more promising for measuring time evolved densities of C4+ and C6+ at the outer midplane SOL and edge plasma. The 16 lines of sight can be split into 8 woven measurements of each emission line simultaneously. Finally, the best chance of directly measuring CV and a parallel accumulation of impurities at the crown of DIII-D, or throughout the main-SOL, would entail the MDS views. The tangential array coupled with the lower poloidal lines of sight are attractive because of their wide range of view that could isolate a peak in C4+ throughout the SOL crown. The emission line of interest would be CV at 494.4 nm, but this is one of the theoretical emission lines rather than a previously observed line. Additionally, this spectral range may include emission from oxygen and iron along with other impurities that could interfere with the carbon line emission. Grating availability within these ranges are also of concern for other diagnostics. One hope is for a grating that could measure the 494.4 nm line. If we can obtain gratings that are capable of observing this emission line, we can effectively use tangential cameras and other systems to all measure the CV emission. Testing of the line emission in order to evaluate the merit of using spectroscopy for monitoring C4+ in the SOL is still required. The natural background carbon from the walls of DIII-D provides the background startup signature. Following shots should incorporate methane puffing in order to evaluate if there is a difference in the background subtracted spectrum versus the methane injection shot. Observation of the C4+ line emission is critical to the success in measuring the impurity accumulation as well as the time evolution of carbon throughout the near-SOL. With these measurements in hand for the carbon time evolved density in the near-SOL, we can then look closer to the mechanisms of transport from the near-SOL reservoir.

$$\tau_{SOL} = (n_{SOL}L)/(\frac{1}{2}n_0 c_s) \approx L/c_s \qquad 2.6$$

Traditionally, on can estimate the average dwell-time in the SOL, $\tau_{SOL} \approx L/c_s$. In the equation, the terms refer to the connection length and the plasma sound speed. Typically, edge temperatures are in the range of 1-100 eV, so the sound speed is often on the order to 10^4-10^5 ms^{-1}. With L on the order of 20-40 m, the resulting SOL residency time is around 1 ms. This is very short relative to the ~1 second core energy confinement times that are typical of large tokamaks. The SOL particle confinement time can also be defined as the SOL particle content divided by the particle outflux as seen in the previous equation. Remaining in the equation for the near-SOL reservoir, there are terms for core plasma and far-SOL contributions. These will be discussed in the following sections.

Next, the far-SOL reservoir will be discussed. This portion of the plasma is boxed between the near-SOL, the vessel walls, and the divertor targets. Impurity particles will likely enter this reservoir via cross-field diffusion from the near-SOL unless the plasma strike point is such that the far-SOL intercepts the $^{13}CD_4$ gas puff. Carbon is traditionally thought of as non-recycling, but low recycling is often considered more appropriate in the literature. Impurities exit the reservoir via parallel motion towards the divertor targets, but in the far-SOL we find that perpendicular motion still plays a major role in the motion of impurities. These processes combine in order to define the reservoir equation seen in the following:

$$\frac{dN_{fSOL}}{dt} = \frac{N_{nSOL}}{\tau_{nSOL}}\left(f_{\perp,nSOL}\right) + \frac{N_{wall}}{\tau_{wall}}(R) - \frac{N_{fSOL}}{\tau_{fSOL}}\left(2f_{\parallel,fSOL} + 2f_{\perp,fSOL}\right) \qquad 2.7$$

Similar evaluation of this reservoir, in comparison to the near-SOL, may be made. However, there are some differences. For example, the wall recycling fraction (R) may be set quite low in order to account for the once through nature of non-recycling impurities. This effectively removes the wall source term from the equation and is similar in effect to turning off the pumps in the divertor reservoir. We have already evaluated the other contribution to the far-SOL ($\frac{N_{nSOL}}{\tau_{nSOL}}\left(f_{\perp,nSOL}\right)$) in the previous section. Now, we are left with measuring the time evolution of the far-SOL particles and weighting the relative contribution of parallel and perpendicular flow. In order to monitor the far-SOL, CER has some tangential view chords using the 30LT beam on DIII-D that is capable of monitoring carbon lines. Tangential filterscopes are another option for viewing CIII in the far-SOL using the midplane views that are available. Finally, SPRED is capable of looking at low-Z impurities within DIII-D. With these three options, we can monitor the far-SOL reservoir time evolved impurity density.

What then remains in the reservoir equation are the weighting factors that will be used on the perpendicular and parallel impurity flows. Perpendicular flow is again based on the diffusion processes that may occur throughout the SOL. Referencing to Figure 33, we see that the diffusion coefficient saturates to ~10X larger in the far-SOL when compared to the near-SOL. As an example, we can continue to use the available Alcator C-Mod data in order to use 1 m^2/s as the reservoir diffusion coefficient. The far-SOL width, however is not properly defined in the figure. Specifically, on DIII-D, there has been previous work that has looked in detail at the far-SOL plasma parameters and their dependence on density or the confinement regime [48]. Midplane reciprocating probes can again be used to provide this width at the outboard midplane while using the electron density profiles. Using another important tool in this reservoir, collector probes can help interpret the dimensions of the far-SOL when combined with flux surface reconstructions using DIII-D's EFIT data. When looking at 2016 Metal Rings Campaign data on DIII-D at the outboard midplane, we can see that the SOL width is typically on the order of several cm in length. This is based on the amount of deposition that is on the collector probes. The reciprocating probes show similar values depending on the limiting surfaces along the field lines. Based on these observations, here we will take an assumed far-SOL width ($l_{\perp,fSOL}$) at the midplane of 10 cm. Depending on the Greenwald fraction (empirical density limit) that is measured, the radial profile of the SOL can vary [49]. The effect is low on the electron temperature, but there is a strong correlation with the parallel velocity. The flow in the far-SOL is also often proportional to the temperature and is inversely proportional to the poloidal magnetic field. We find that the friction forces typically dominate over the thermal gradient forces and therefore, the particles are directed with velocity, parallel to B, that is towards the nearest target. For the sake of developing this particle balance, we will for now use an estimated parallel velocity that is less than 20% of that used in the near-SOL reservoir. Following a similar procedure for evaluating the weighting factors in the previous portion of the model, we can calculate the parallel and perpendicular travel times through the reservoir for particles. Perpendicular motion throughout the now wider reservoir in combination with a larger diffusion coefficient estimates the time to be on the order of 1 ms. Parallel motion towards the target remains to have a connection length that is comparable with the near-SOL; however, the far-SOL parallel velocity is now much lower and produces a parallel travel time of nearly 4 ms. Since it requires less time for particles to travel across the field lines, that is perpendicular, the number of particles that will pass in a given time step is related inversely to this calculated value. Thus, the weighting factor is more heavily in favor of cross-field motion over a given time step in the reservoir model. In this dissertation, the 3DLIM code will be predominantly used to model the far-SOL reservoir and the transport of impurities near collector probes. The coupling of the far-SOL and near-SOL is accomplished through using DIVIMP impurity distributions (near-SOL estimates) as an input into 3DLIM (far-SOL simulation).

Next, we have the core reservoir. Considering the core only has direct contact with the near-SOL, the equation that is proposed is quite simple. There is a term for the contribution of particles from its neighbor, which has previously been discussed. There is also a term for particles that will leave the core as is shown in the following:

$$\frac{dN_{core}}{dt} = \frac{N_{nSOL}}{\tau_{fSOL}}\left(2f_{\perp,nSOL}\right) - \frac{N_{core}}{\tau_p} \qquad 2.8$$

The core density changes with time as a function of its contribution to and from the SOL. The core impurity density will give up particles to the SOL based on the core impurity residency time (τ_{core}). The main plasma includes the confined portion that is within the bounds of the separatrix. Traditionally, within the LCFS, the core particle confinement time is dependent on the minor radius and the perpendicular diffusion coefficient for the plasma core as shown below.

$$\tau_{core} = \frac{a^2}{D_\perp^{core}} \qquad 2.9$$

These particles are transferred into the SOL, *which has not often been considered a reservoir but rather an outlet for particles to enter the divertor*. DIII-D has a minor radius of 0.67 m. The core perpendicular diffusion coefficient can be approximated as 0.5 m^2/s but closer to 0.1 m^2/s or less [50]. For the purposes of the particle balance, the core term may be observed through the use of spectroscopy that monitors the highest carbon charge states. CER, for example, is able to monitor C6+ density evolution with time at various points throughout the core. Charge exchange recombination spectroscopy is a measurement of the intensity or spectral distribution of photons that are emitted from a charge exchange reaction between an injected neutral atom with the plasma ions. High energy neutral beams on DIII-D provide the neutral particles which interact with fully stripped low-Z impurity ions such as C6+. These measurements are localized based on the point in which spectroscopic line of sight intersects the neutral beam. Carbon is one of the most commonly monitored species on DIII-D using CER, so the data should be readily available after each experiment.

Gas puffing experiments have another particular advantage over other impurity transport experiments in that they give the user direct control over the external source of impurities. This allows for independent study of the screening process. Several experiments for non-recycling impurities have locally injected methane and nitrogen in order to measure the penetration factor of the impurities and its dependence on the plasma density along with injection location. Penetration factor (PF) is defined here as the core impurity density normalized to the external source of impurities. The experiments have found a weak dependence with electron density and a nearly linear relationship with the impurity puff rate. For the $^{13}CD_4$ experiments, this quantity could be obtained by measuring the core impurity density through CER measurements of C6+ along with a calibrated puff rate of the isotopic methane gas through the UOB puffing valves. The non-recycling impurity particle balance parameter τ_{SOL} may also be used to describe the SOL sink-action strength or SOL screening effectiveness, and may be obtained directly through MDS time evolution of the CV signature at ~494 nm. Comparing opposite B_T effects on the SOL sink action would be a useful set of new experimental results. Future efforts would likely benefit from digging further into this topic and looking into the coupling of the AURORA code with this workflow for solving the radial transport equations for impurities that enter the core.

Last but not least, the walls of DIII-D are the final reservoir in the model that requires consideration. However, this reservoir acts more like a particle sink than a reservoir. Carbon, being a non-recycling impurity has a low probability of backscatter from the surfaces that it comes into contact with while in transit. If the particles were to backscatter, then we could account for this with a low recycling fraction that could provide particles radially back into the SOL plasma. As for particles that will enter the reservoir, we expect cross-field particle motion to dominate. The proposed equation for this portion of the particle balance is shown below.

$$\frac{dN_{wall}}{dt} = \frac{N_{fSOL}}{\tau_{fSOL}}\left(f_{\perp,fSOL}\right) - \frac{N_{wall}}{\tau_{wall}}(R) \tag{2.10}$$

Carbon that encounters the wall is expected to have a long wall residency time. This is a simplification due to the once through nature of the impurity and essentially converts the ‘wall reservoir’ into a particle sink. Non-recycling species are considered to be removed once they hit the wall or any solid surface. At this time, the wall residency time is set to a large value and the recycling fraction is low in order for the model to account for this behavior.

This section simply aimed to walk through a thought experiment on how impurities travel throughout a tokamak plasma with examples of how to monitor that flow through various diagnostics. Several codes including MAFOT, DIVIMP, and 3DLIM are included in this dissertation for simulating the near and far-SOL impurity density profiles as well as transport near collector probes. The focus here is therefore on the near and far-SOL reservoirs which have previously been ignored in this sort of analysis. Discussion in this dissertation will focus on results from the methane injection experiments in this context and reveal how the non-recycling nature of carbon impurities assumption may not hold true.

CHAPTER THREE
RESULTS AND DISCUSSION

3.1 Overview

In this section, a chapter overview is presented. Section 3.2 re-iterates the planning process for the methane injection experiments and introduces the mini-proposal that was submitted for the experiments. Sections 3.3-3.8 are an adaptation of a publication submitted to the Nuclear Materials and Energy Journal for the 2022 PSI Conference. The paper focuses on collector probe deposition measurements in the far-SOL. Results highlight isotopic analysis of the surface deposits on the collector probes using the LA-ICP-MS technique for carbon isotopes. Using the isotopic measurements, a stable isotopic mixing model has been developed for carbon isotopes and has identified a re-eroded wall source of enriched ^{13}C that contributes to collector probe deposition profiles along with enriched ^{13}C from the methane injection puff. The paper adaptation looks only at a select portion of the collector probe inventory that was exposed at DIII-D during methane injection experiments.

3.2 Experimental Mini-Proposal and Shot Plan

Preparation for these experiments began as far back as 2019. In June of that year, startup time was dedicated to our group for plasma scenario development. Sixteen (16) shots were used to develop the upper single null shape that was needed for methane injection and proper SOL positioning. These were plasma shots 178335 through 178351. Students traveled to DIII-D for these startup tasks and began with a test shot that was based on 171553. With the initial success of this discharge, we then attempted to shift the plasma vertically by 20 cm using the DIII-D ‘Zp’, ‘Zx’, and ‘GapBot’ options. The machine was having issues, so some of the 16 shots were considered failures. However, there was success in developing a shape that was limiting on the shelf of the lower divertor. This is an extreme case that should not be used for DiMES experiments. The heat flux in the crown would exceed the operational constraints that have been placed on the DiMES CP. This shift was still useful for shape development.

Knowing that we could successfully operate down to the Z extreme gives one a better sense of the operating space and where the plasma crown may be positioned in relation to DiMES. Now, instead of performing a rigid shift of the plasma, elongation was tested. This requires a stagnant X-point while again shifting the crown of the plasma. Therefore, the core is *elongated* rather than rigidly shifted. This increases plasma volume, but also allows for X-point control when injecting the methane as well as sweeping the strike points. This series of shape control experiments, provided a launchpad for additional tweaks prior to experimentation. With a better-defined plasma shape, the injection of methane using the Upper Outer Baffle (UOB) valve system was tested. Standard methane was used for these series of startup shots and the most recent neon calibration was used to set the voltage for the UOB valves. This was the only option considering we still needed a methane calibration to be performed. This calibration allows for translating the voltage to gas injection rate. During the injection tests, it was found that lower flow rates of ~10 Torr-L/second performed as expected. Higher flow rates were not as favorable. When flow rates were increased to 20 and 30 Torr-L/second, the plasma was unable to complete a full discharge. This outcome suggested a softer ramp to the higher flow rates or sticking to lower gas introduction rates would be required.

Following the startup days at DIII-D, a shot plan was developed in time for experiments (experimental number 51-01) that were to occur during the week of October 14th, 2019. However, there were some last-minute issues at DIII-D that forced the cancellation of the experiments. This gave the team additional time to fine tune the mini-proposal and prepare additional hardware.

Several other delays, including a global pandemic, forced the experiments to be pushed back to 2021. With a few more control days to figure out the UOB issues that were discovered in 2019, the experimental plan evolved from the original idea that was on the slate for 2019. The additional hardware production also enhanced the investigative capabilities past the original proposal. In addition, the plasma discharge that was produced during the startup tasks was modified even further with the assistance of simulation. All of these modifications culminated into a shot plan for experiments that would eventually occur in 2021.

Explicit details for the mini-proposal and shot plan may be found in the appendix. Note that this mini-proposal was a collaborative effort between the listed co-authors that was prepared by Dr. J.H. Nichols. These documents are designed to act as an experimental proposal for experiments that have been approved at DIII-D. They outline the goals of the experiments, background, experimental approach, required resources, a detailed experimental plan as well as the final plans for presenting the work. With the proposal prepared, enriched methane on site, diagnostics ready, and collector probes ready to collect, the experiments commenced.

Due to the nature of running experiments on DIII-D, not all experiments were run as planned. These methane injection shots occurred over four days. The first day was January 18th, 2021 for shot range 184164 - 184184. The second was run on January 22nd, 2021 for shot range 184262 – 184274. The third was February 4th, 2021 for shot range 184524 - 184540. The final was during director's reserve time on June 17th, 2021 for shot range 187098 - 187123. Additional details for these shots are available on the DIII-D internal website under their associated physics summary pages. The results and discussion presented here is focused primarily on the director's reserve time.

3.3 ^{13}C Characterization of Midplane and Crown Collector Probes on DIII-D

Many of the ideas in this section and it's subsections have been introduced in Chapter 1 and Chapter 2. However, this section aims to emphasize the important points. Impurities within a tokamak plasma are known to degrade performance by reducing core temperatures through radiation and fuel dilution. In order to achieve a burning plasma, stringent core impurity concentration thresholds of ~ 0.02% for tungsten impurities have been established [51]. Many impurities are sourced from the divertor target as a result of the intense plasma interaction with a material surface. Graphite and tungsten are common high-durability materials used to armor these target regions, but these materials still can be released into the edge plasma by sputtering, melting, or ablation. As a result, the eroded impurities travel along the plasma scrape-off-layer (SOL) and enter the plasma core through motion perpendicular to plasma flux surfaces. The resulting core contamination can be unacceptable; thus, SOL transport needs to be studied further in order to develop mitigation techniques for core pollution by impurities.

Many methods have been developed to study impurity transport processes. However, there are limited options for direct sampling of the impurities in the SOL. Graphite collector probes are diagnostics that allow for direct contact with the edge plasma. These probes provide shot-integrated measurements of the impurity flux in the far-SOL. While the probes may survive insertion into the near-SOL, they do not provide interpretable impurity deposition measurements when inserted into this plasma region due to re-erosion of deposited materials. As collector probes are inserted deeper into the SOL and closer to the separatrix, the sputtering and erosion rates of deposited materials increases with the associated rise in electron temperature and parallel particle flux of low-Z ions such as hydrogen. Thus, near-SOL use of collector probes compromises the measurements being made; therefore, collector probes are considered far-SOL diagnostics for measurements of impurities e.g. in regions where the electron temperature $T_e \leq 10$ eV. Use of a single collector probe in the far-SOL has been shown to provide valuable insight into the transport of tungsten impurities as they traverse the plasma boundary [7, 16, 52]. The following sections introduces a dual collector probe system for DIII-D, investigates the transport of isotopic ^{13}C impurities, and discusses the intricacies involved in surface analysis of the collector probes.

3.3.1 Crown and Midplane Collector Probes

Newly designed collector probes were installed in the crown (lower divertor of upper single null plasma) and at the midplane of DIII-D. The crown probe is installed on the Divertor Materials Evaluation System (DiMES) and the midplane probe is installed on the Midplane Materials Evaluation System (MiMES) [17, 18]. Each probe is referred to as the DiMES Collector Probe (DCP) and MiMES Collector Probe (MCP) respectively. Probe designs are shown in Figure 17. Dashed lines on the alumina and steel components mark boundaries of internal features. The flat collection faces of each collector probe have been coated with 4-6 µm of silicon, which assists in surface characterization and provides a boundary between the underlying graphite and the deposited carbon impurities. Silicon coating was performed using an e-beam evaporator at ORNL. The technique is slow at ~1-10 angstroms/second but provides a uniformly coated surface. Impurity collection regions of interest are the flat graphite (dark grey) surfaces on each probe. The flat faces collect impurities and are also marked with red spots down the center where characterization scans are performed. These flat faces are mirrored with a second collection surface being on the opposite side of each probe. Both flat collection faces are oriented such that they are approximately normal to the direction of the toroidal magnetic field. If one were to follow the field line trace from a flat collection face, it would terminate on the first limiting surface in either the inner or outer target direction. These are named accordingly as the inner target facing (ITF) and outer target facing (OTF) sides of the collector probes. Experimental measurements are presented in the following sections. Figure 17 shows that each collector probe requires a unique assembly due to the dimensions of the reciprocating drives on which each is installed. The designs expand on those employed during the 2016 Metal Rings Campaign [7, 53].

3.3.2 Methane Injection Experiments

The two collector probe diagnostics, shown in Figure 17, have been designed and implemented to gather impurities flowing through the SOL in the DIII-D tokamak during a set of methane injection experiments [7, 54]. Isotopically enriched and deuterated methane ($^{13}CD_4$) is injected near the outer strike point during these experiments as shown in Figure 37. The methane disassociates and the resulting ionized ^{13}C traverses the plasma. While in transit, the impurities are sampled using the MCP and DCP. Collector probes are plotted as black bars in Figure 37 in order to show the relative size and position of each probe in the tokamak. The exact position of the MCP tip is variable in the radial direction due to the MiMES reciprocating drive and depicted at (R, Z, ϕ) = (2.325 m, -0.188 m, 235°). The DCP tip is located at (R, Z, ϕ) = (1.4859 m, -1.205 m, 150°), where ϕ marks the toroidal coordinate within DIII-D. Collector probe impurity sampling length along the collection area of the probes are marked by the shaded flux surfaces in Figure 37. The sampling length was calculated based on the methods described in Section 1.6. These shaded regions are the result of field line traces across the fully exposed length of each probe from the MAnifold & FOotprint Tracer code, MAFOT [47]. **For the first time on DIII-D, these probes are used in tandem to obtain simultaneous, spatially localized measurements of impurities in the far-SOL [55]**. The first use of a dual collector probe system is a major engineering accomplishment of this work.

While there were ten sets of collector probes exposed to various conditions for these experiments, this paper focuses on the two detailed in Table 4. Experiments are performed in two stages. First, a diagnostic phase is performed for a single plasma shot. The diagnostic phase employs the MiMES reciprocating Langmuir probes where SOL density and temperature profiles are gathered at the outboard midplane and used to provide heat flux estimates throughout the SOL, see Figure 38 [54, 56]. Common practice is to insert the collector probes to where $q_{\parallel}$ ~1-2 MW/m^2, and this was followed in this experiment. This threshold ensures that the probes are inserted deep enough for impurity deposition measurements, but not deep enough to exceed the administrative limits.

Following the diagnostic phase, a collection phase is performed for a series of two shots of nearly identical conditions to the diagnostic phase discharge. However, during this collection phase, both the DiMES and MiMES reciprocating drives are equipped with the collector probes. Both probes are inserted for the full duration of the plasma discharges and are retracted between shots to prevent exposure during bakeout. During the plasma discharge, in both diagnostic and collection phases, isotopically enriched methane ($^{13}CD_4$) is puffed into the upper outer pumping plenum (with cryopumps off) from 2200-4500 ms at a rate of 14.3 Torr-L/sec, see Figure 37. Puffing into this plenum distributes the methane as a toroidally symmetric source of impurities. Isotopic methane was chosen in the form of $^{13}CD_4$ (99 atom % D and ^{13}C) so that the isotopic carbon can be distinguished from natural carbon that is sourced from the first wall of the device and any underlying graphite that has been exposed due to erosion of the silicon layer. Use of enriched ^{13}C enables interpretation of the transport pathway of the injected methane throughout the device as it deposits on collector probes and other limiting surfaces. Carbon is a non-recycling impurity due to its low backscatter probability once it interacts with a material surface, though chemical erosion of deposited carbon is possible. The ‘once through’ nature of non-recycling impurities, such as carbon and tungsten, enables the use of collector probes in impurity transport studies, though recent studies on ASDEX-U have reported success using isotopically enriched nitrogen with collector probes [57]. Impurity collection also requires that the deposition probe not be inserted into a region with too high electron temperature and heat flux to avoid re-erosion of the deposits, i.e. that it be deployed in the far-SOL. The DCP cannot extend further than 4.5 cm above the tile surface due to engineering and administrative safety constraints relating to the operation of the gate valve, so plasma shape control is the only option for positioning the DCP in the plasma crown. MCPs are installed on a reciprocating drive and can be adjusted to an appropriate distance following the diagnostic phase. Following plasma exposure and impurity collection, the collector probes are removed for ex-situ for surface analysis.

3.4 Surface Characterization of ^{13}C

Following plasma exposure, the methane injection experiments used Laser Ablation Inductively Coupled Plasma Mass Spectrometry (LA-ICP-MS or LAMS) to measure ^{12}C and ^{13}C down the centerline of each probe exposed to conditions presented in Table 4 [23]. Each centerline measurement is presented in Figure 39.

The four plots on the top of Figure 39 show ^{12}C as measured by LA-ICP-MS while the bottom four plots show ^{13}C. The legend shows that both a set exposed to methane injection and a control set exposed without methane injection are plotted. As noted by the y-scales on the axes, ^{12}C is shown to dominate the CP measurements. Natural carbon is abundant in the graphite tiles that comprise the first walls of DIII-D. This material likely eroded and significantly contributed to the carbon deposition that is measured on the collector probes. NIST isotopic composition values for carbon are 98.93 % ^{12}C and 1.07 % ^{13}C. When calculating the isotopic composition of the collector probe measurements, these values are shown to deviate from the NIST standard. The isotopic fraction of ^{13}C is presented in Figure 40 for collector probes exposed to the methane injection and control set conditions.

Figure 40 shows that the methane injection experiments successfully measured enriched carbon deposits upstream of the injection location on both the MCP and DCP sets. Any positive deviation from the natural 1.07 % ^{13}C concentration suggests enrichment in the ^{13}C measurements by LA-ICP-MS, which was introduced with enriched methane injection. The OTF side of the MCPs show significant enrichment up to R-R_{SEP} OMP = 11 cm. Conversely, the ITF side of the probe show low levels of enrichment at R-R_{SEP} OMP < 10 cm. Low ^{13}C enrichment on the MCP ITF is a result of measuring the underlying graphite that is used as stock material (ATJ Graphite) for machining the CPs, which is the same type of graphite from which the first wall of DIII-D is constructed. The silicon layer along with any deposited material has eroded on the MCP ITF up this point. Erosion of the MCP ITF surface decreases with increasing distance from the separatrix. With this decreasing effect of erosion, there is an associated increase in the ^{13}C concentration to a maximum R-R_{SEP} OMP = 12 cm. ITF ^{13}C concentration then decreases when moving further along the MCP centerline. If erosion were *not* to occur, it is expected that the ^{13}C concentration would be greatest at the lowest R-R_{SEP} OMP values and then decrease as the connection length decreases. When observing the DCPs, ^{13}C enrichment is greater than that measured on the MCPs. The ITF profiles for DCPs are approximately level across the collector probe surface while the OTF faces tend to increase with R-R_{SEP} OMP until ~ 6.5 cm. This is likely due to the significant flux expansion in the crown region, meaning plasma conditions at the DCP have minimal radial variation.

The methane injection set is used in Figure 39 and Figure 40 as a representative set of the CPs exposed to methane injection. The control probe set was exposed to matching conditions, but methane injection was turned off. Results show that ^{13}C has built up on the walls of DIII-D. Re-erosion of these enriched deposits then acts as a secondary source of enriched ^{13}C along with the methane puff at the outer strike point. The relative contributions of each source to the measured deposits on the DCP and MCP surfaces may be distinguished using a basic Stable Isotopic Mixing Model (SIMM) for carbon isotopes [34].

3.5 A basic Stable Isotopic Mixing Model for Carbon Isotopes

As shown in previous sections, the collector probe measurements by LA-ICP-MS yield a unique isotopic fingerprint that is a combination of a natural source of carbon as well as an enriched carbon source. Stable isotopic mixing models may be adapted for carbon isotopes to distinguish between these two sources and provide the fractional source contributions to the measurements made by LA-ICP-MS. The enriched source fractions of deposition for the control probes will then identify the fraction of enriched ^{13}C deposits from the re-eroded wall deposits of ^{13}C. Subtracting this value from the probes exposed to plasma with a methane puff will provide an estimate of the enriched source fraction that is from the injection of enriched methane. The SIMM analysis for two sources of natural and enriched carbon reduces to the following equation set:

$$f_{enriched} + f_{natural} = 1 \tag{3.1}$$

$$(\delta^{13}C_{mix} - \delta^{13}C_{natural}) \cdot f_{natural} + (\delta^{13}C_{mix} - \delta^{13}C_{enriched}) \cdot f_{enriched} = 0 \tag{3.2}$$

While f_j is the fraction of each source in the sample, the $\delta^{13}C_x$ values are the degree of isotopic concentration deviation from a baseline standard, calculated using the following equation set:

$$\delta^{13}C_x = 100\left(\frac{[R_{12}^{13}]_x}{[R_{12}^{13}]_{standard}} - 1\right) \tag{3.3}$$

$$R_{12}^{13} = C^{13}/C^{12} \tag{3.4}$$

Source fraction, for the measurements in Figure 39, is determined using the four equations above along with data presented in the previous sections. Isotopic concentrations for a given sample, C^{13} and C^{12}, are used to calculate the isotopic ratios R_{12}^{13}.The denominator, $[R_{12}^{13}]_{standard}$, in the parentheses of each $\delta^{13}C_x$ term is a constant value calculated using the natural isotopic concentration values from NIST such that $[R_{12}^{13}]_{standard} = 0.0107/0.9893 = 0.01082$. The numerator, $[R_{12}^{13}]_x$, in the parentheses of Equation 3 is variable based on the source or sample of interest: $mix, natural, enriched$. For example, $\delta^{13}C_{enriched} = 914872.27$ and is calculated using the isotopic ratios of the enriched methane source puffed into DIII-D. High δ is expected for a source enriched ~98 % above the isotopic concentration found in natural carbon. $\delta^{13}C_{natural} = 0$ because $[R_{12}^{13}]_{sample} = [R_{12}^{13}]_{standard}$ when considering a source of carbon with natural isotopic ratios which match the NIST standard. $\delta^{13}C_{mix}$ is variable based on the position along the collector probe surface characterization scan and is calculated using the values in Figure 40 for C^{13} along with C^{12}. Using these values and equations, $f_{enriched}$ is then calculated and presented in Figure 41.

3.6 Discussion and Conclusions

Carbon has been characterized across the surface of collector probes exposed to DIII-D plasma discharges during a series of methane injection experiments. Collector probes have been exposed both with and without methane injection under matching conditions. Measurements of probe sets from both cases show enriched carbon deposits across the surface that accounts for less than 0.1% of the total measured carbon deposits, see Figure 41. Trace levels of impurities in this range give credence to using a SIMM for analysis of the carbon deposits. Both MCP and DCP probes show higher levels of enrichment and total deposition than those exposed without a $^{13}CD_4$ puff into the outer strike point of the plasma. The fact that enriched ^{13}C signals are found on the control set of probes suggests that ^{13}C has accumulated on the first wall components of DIII-D, and is then re-sputtered during subsequent discharges. It is likely that the highest ^{13}C concentrations would be found at the inner strike point with generally lower concentrations across the rest of the main wall plasma facing components [32]. During plasma exposure, these deposits re-erode and act as a secondary source of ^{13}C that contributes to the fraction of enriched deposits, $f_{enriched}$, that was measured on the control probe set by LA-ICP-MS. These contributions are quantified using the SIMM and control probe measurements such that $f_{enriched}$ is distilled into two components. The control probe set was exposed to plasma without methane injection. Therefore, any enriched ^{13}C in the measurements are from the re-eroded wall source. $f_{enriched}^{control}$, in Figure 41 is therefore considered the component of the enriched deposits that comes strictly from this re-eroded wall source, f_{wall}. The injection set in Figure 41, $f_{enriched}^{injection}$, is a measurement of the combined effects of the enriched re-eroded wall source as well as the enriched methane puff. We can then perform similar analysis and assume the fraction of enriched ^{13}C deposits from the methane puff, $f_{puff} = f_{injection}^{enriched} - f_{injection}^{control}$. The results from these calculations are displayed in Figure 42.

Enriched carbon measurements on MCPs are found to be comprised of an average of 60% material that is re-eroded from the walls following injection and deposition from previous $^{13}CD_4$ injections into DIII-D. The remainder of the enriched deposits is sourced directly from the $^{13}CD_4$ puff. Enriched ^{13}C deposits on the DCPs appears to be primarily from the re-eroded wall source of ^{13}C across the full length of the ITF face with a small puff dominance at lower R-R$_{SEP}$ OMP on the OTF face.

These results lay the ground work for additional analysis and modelling efforts that will be presented. Understanding the source of impurities feeding the collector probe measurements allows for accurate models to be developed for ^{13}C impurity transport. SIMM analysis and a dual collector probe system suggests that simulation of methane injection into the outer strike point alone will not be sufficient for simulation of the methane injection experiments. Instead, a re-eroded wall source must be considered along with the puff of enriched impurities in order to accurately model SOL impurity profiles of ^{13}C that feeds a dual-collect probe system on DIII-D. The control probe set presented has proven to be vital to this analysis and will be used for further analysis in Chapter 4.

CHAPTER FOUR

POWER SCAN EFFECTS ON IMPURITY TRANSPORT AND IMPURITY DEPOSITION PATTERNS

4.1 Overview

This chapter expands the collector probe inventory of interest to include those exposed to various levels of injected power while all other conditions were held the same. The stable isotopic mixing model from chapter three is applied to these collector probes and a trend emerges with the increase of injected power related to the deposited material on the probes. This is particularly interesting in understanding the effects of the different source materials on the SOL reservoirs, as defined in Section 2.7, and the impurity density profiles within those reservoirs. Spectroscopic observations of various carbon charge states are also introduced in this chapter to round off the experimental and diagnostic observations of carbon impurities throughout the plasmas.

Chapter four then transitions into the modelling efforts involved with the analysis and interpretation of the methane injection experiments. Results and discussion are both presented for DIVIMP modelling that was prepared for the various sources of enriched ^{13}C impurities that are believed to contribute to the collector probe deposition patterns. In this chapter, two sources are identified and simulated to produce unique DIVIMP impurity density profile estimates for the enriched carbon sources.

Following the development of impurity profile estimates in DIVIMP, these are used to inform simulations of impurity transport near collector probes using the code 3DLIM. This section utilizes the most recent developments in 3DLIM where the full geometry of DIII-D is used to constrain the boundaries of the simulations in the code through coupling with MAFOT. In this section, several key physical parameters are noted to hold the greatest impact on accurately reproducing the impurity deposition patterns that are found on collector probes using simulations in 3DLIM.

4.2 Experimental Observations with Varying Injected Power

A select portion of the collector probe inventory was used in the previous section to emphasize the importance of the control collector probe that was exposed without methane injection. **Without measurements provided by this probe, it is unlikely that the details discussed below would have been discernable.** This section then expands the inventory of collector probes to not only include those previously presented but now considers those exposed to conditions listed in Table 5. As noted in the table, the amount of power injected into the plasma discharge was varied across the probe inventory in this section. Models predict that injected power into the system may act as an actuator for the temperature gradient forces acting on impurities that leads to changes in impurity leakage.

The broader inventory of collector probes was successful in measuring enriched ^{13}C upstream of the injection location. This is apparent when characterizing the deposition on collector probes exposed to the plasma discharges listed in Table 5. These data, for the DCPs and MCPs exposed during the director's reserve shots, are presented in Figure 43. Note that Set 3 and Set 4 in these cases are the same Injection and Control cases presented in the previous chapter. The remaining two sets, Set 1 and Set 2, show similar deposition patterns across the collector probe faces as those previously presented. In Figure 43, LA-ICP-MS measurements display a relative standard deviation on the order of 8% with error peaks when approaching the sensitivity limits of the technique. This associated error is overlaid as shaded error bands on top of the experimental measurements. The laser ablation scans shown in Figure 43 have been remapped to R-R_{SEP} OMP which assists in visualizing the sampling volume overlap introduced in Figure 37 by the shaded regions. To compare the magnitude of each deposition profile, these measurements were taken in immediate succession. Reduced time between measurements minimizes errors produced by detector drift when using LA-ICP-MS and allows for comparing the relative counts from one face to the other. Long warm-up periods for the ICP-MS are also beneficial for reducing detector drift. Typically one is interested in reducing the background oxygen signatures present during a system tune. This can take ~30 minutes to an hour with the LA-ICP-MS system at ORNL. Data obtained prior this time much more susceptible to the effects of drift. Data for each probe face is presented in separate plots with unique ordinate scales in order to adequately display the features of each deposition profile.

One of the shortcomings of LA-ICP-MS is the lack of reference materials that enable quantitative measurements. In order to address this limitation, areal density measurements of the deposited ^{13}C and ^{12}C has been provided by nuclear reaction analysis (NRA) for a set of collector probes exposed to enriched methane injection experiments. Areal density measurements of the surface carbon isotopes were obtained using, 2.5 MeV He-3 nuclear reaction analysis at Sandia National Laboratory. NRA analysis has calculated the enriched impurity contributions to the collector probes using a different method when compared to the stable isotopic mixing model in Section 3.5. Carbon impurity deposition data analysis needs to account for the graphite from wall erosion in DIII-D. The potential deposition from this carbon source is natural carbon at 99% ^{12}C and 1% ^{13}C. Carbon from the puffed impurities is enriched to 99% ^{13}C and distinguished from the natural carbon by measuring the ^{13}C coverage in excess of the 1% natural abundance of the deposited ^{12}C. Measurements of this '^{13}C excess' deposition from the injected ^{13}C are presented in Figure 44. These measurements correlate with the centerline scans marked in Figure 17. ^{13}C excess deposition was measured by NRA at a maximum value of ~1.75 x 10^{16} atoms/cm^2. This value is well within the measurement range of the system and is lower than previous W deposition measurements during the 2016 DIII-D Metal Rings Campaign and near the lower sensitivity limit of the technique which is in the range of 0.5 x10^{16} atoms/cm^2. The uncertainty for NRA measurements is the same as this limit of detection. Overlaid are Savitzky-Golay filtered LA-ICP-MS measurements that are fit to the calibrated NRA measurements [58]. LA-ICP-MS measurement error bands are calculated using standard detector counting statistics. While the profiles presented in this figure are not included in the set of exposures listed in Table 5, the deposition shows quantitatively similar LA-ICP-MS response to those probes. However, this ^{13}C excess calculation is likely not as accurate in calculating the enriched deposit contributions as the stable isotopic mixing model. Unfortunately, a control probe is not available for the set measured by NRA, so the stable isotopic mixing model cannot further distill $f_{enriched}$ into contributions from each enriched source as was performed in Chapter 3.

One can assume that the control probe presented in Chapter 3 is representative of the f_{wall} value for the collector probes exposed during the power scan. Approximately 340 Torr-Liters of enriched methane was injection prior to exposure of the control probe. This inventory of enriched ^{13}C is likely the culprit for producing the source that contributes to f_{wall}. With this assumption and when applying the stable isotopic mixing model to the inventory listed in Table 5, trends begin to emerge in the deposition profiles with changes in the level of injected power. Following the same procedure described in Chapter 3, the fraction of enriched deposits from both the re-eroded, enriched wall source as well as the enriched methane puff has been calculated for the full collector probe inventory. These are synonymous to those presented in Figure 42 and are shown in Figure 45 and Figure 46 for the MCPs and DCPs respectively. Considering the deposition profiles for each probe face share many of the same features with one another, there are similar caveats for all sets that determine where the data and calculations are most accurate and representative. Magnitude of deposited materials, level of enrichment, and effects from erosion must all be considered in determining what regions are qualified for analysis and further consideration.

Consider the ITF profiles of the MCP inventory shown in Figure 45 and the associated magnitude profiles shown in Figure 43. In Figure 43, the magnitude of the measurements is greatest between 20 and 60 mm from the tip of the collector probe. Prior to 20 mm, the collector probes eroded due to plasma interaction. This causes the increase in the MCP ITF measurement magnitudes because the underlying graphite is exposed following removal of the silicon layer. The magnitude of impurity deposition on collector probes has been shown to correlate with connection length profiles. In the ITF direction, the connection length is greatest at the tip of the probe and then decreases as one moves along the probe centerline out towards the wall. Therefore, if no erosion were to occur, greater deposition would be expected on the MCP ITF before 20 mm. Additionally, the isotope enrichment profiles in Figure 40 suggest that the deposition of interest is also correlated with the greatest level of isotopic enrichment. Therefore, the peaks in the magnitude and enrichment profiles at ~30 mm are likely where the qualified region begins for this collector probe face.

For the other collector probes and faces, erosion does not impact the deposition as strongly compared to the MCP ITF faces as seen during visual inspection of the probes post exposure. Therefore, magnitude and enrichment profiles are best for determining the qualified regions across the remaining probe faces. Moving to the other MCP face, MCP OTF, one finds high enrichment and impurity magnitude beginning at the tip of the probe. Therefore, the probe tip is likely the beginning of the qualified region on this face. This region of interest continues across an increasing plateau that then dramatically declines between 30 and 45 mm along the probe face depending on the set of interest. This steep fall in deposition magnitude marks where the connection length profiles decline due to field line traces limiting on the near-wall surfaces in the outer target direction. Data past this point is near the detection limits and is therefore no longer considered qualified.

The DCP profiles are unique compared to the MCPs. First consider the ITF profiles in Figure 43, Figure 46, and Figure 40. While the DCPs show the highest level of ^{13}C enrichment, the low magnitudes of deposition likely outweigh these measurements in determining a qualified region, particularly on the DCP OTF. When observing the DCP ITF, deposition magnitude tends to remain flat across the full length of the probe. For this face, the entire plateau length is likely representative of the qualified region. The flat profiles are expected to be observed in the plasma crown due to the flux expansion as well as the flat connection length profiles observed with MAFOT calculations. While the DCP OTF profiles again show high levels of enriched deposits, the magnitude of deposition is very low and near the limits of detection for the analysis technique. Therefore, it is difficult to pinpoint a qualified region for this face and one may not even consider this data to be reliable.

With the reliable data regions defined for each collector probe surface, one can then revisit the stable isotopic mixing model results for the collector probe inventory presented in Figure 45 and Figure 46. With this approach, the level of injected power into DIII-D appears to increase the contributions of the enriched deposits from the re-eroded wall source of enriched impurities. This is most obvious on the DCP ITF, Figure 46. Here, the low power (2.5 MW) case is shown to have approximately equal contributions from both the enriched wall source as well as the enriched puff source. As power increases to 3.4 and 4.5 MW, the fraction of impurities from the enriched wall source begin to dominate the impurity deposition profiles. By contrast, the enriched puff source becomes less dominant. This is likely explained by increased heat flux to the targets with increasing power into the plasma that results in an increase in the contributions from the re-eroded wall source of enriched ^{13}C impurities. Considering the magnitudes of deposition on the DCP ITF faces are approximately equal, the increased contributions from the enriched wall source also means a decreased contribution from the ^{13}C impurities from the methane puff. This trend also appears to occur on both faces of the MCPs, shown in Figure 45.

The ratio of deposition between the ITF and OTF faces of a probe set are often of interest in informing where increased impurity density is likely present in the SOL. When comparing the portion of the qualified regions with the highest magnitude of deposition, the ITF/OTF deposition ratio is shown to favor the ITF for the DCPs and the OTF for MCPs. This suggests increased impurity densities in between the DCP and the inner target in addition to higher density between the MCP and the outer target. This is a unique situation not originally predicted in the mini-proposal, see appendix, or the discussion presented in section 2.5. However, with these observations in mind, one may begin to guess at what the impurity density profiles may look like within the SOL.

For example, begin with the DCP. The ITF and OTF of this probe have flat connection length profiles that are ~20 m to the nearest limiting surface across the full length of each probe. We were fortunate in the director's reserve experiments in that the ITF of the probe was not immediately limited by the lower divertor tile shelf. Instead, the crown of the plasma was shaped such that the field line tracers were able to pass the shelf and instead limit on the center stack. Having approximately equal connection lengths on both faces greatly simplifies analysis because now both probe faces have very similar sampling volumes. With connection lengths of ~20 m, we know that each probe face therefore samples ~10 m, half of the connection length, in their respective directions. It is within this 10 m distance from the DCP ITF that we would expect greater impurity density relative to the OTF. With very low deposition of enriched impurities on the OTF side of the collector probe, we would expect little to no impurities within the 10 m sampling volume on that side of the probe.

For the MCPs, the ITF tip has a much greater connection length than the OTF. However, when looking specifically in the ‘qualified regions’, both collector probe faces have connection lengths of ~10 m. So again, we have a simplified case where we are able to easily compare probe faces. The MCP faces both show enriched impurity deposits along the collector probe faces. Therefore, the expected impurity profiles are not as obvious. However, the OTF face of the MCP does appear to have greater enriched impurity deposition. Therefore, impurity profiles should have higher impurity densities within the 5 m sampling volume of that face relative to the MCP ITF.

An example of what these impurity profiles is expected to look like is shown in Figure 47. The plot shows expected impurity distribution along a flux surface that feeds the collector probe impurity deposition. In this figure, we see that the impurity distribution is plotted against distance along the flux surface. This distribution begins at the outer target and moves poloidally around the plasma clockwise until reaching the inner target. The relative positions of the MCP and DCP have been overlaid along with the shaded sampling regions that are limited by the connection lengths described above. DIVIMP estimates will be shown in future sections that align with this expected profile.

One may further constrain these expectations with other experimental observations obtained during the methane injection experiments. Many spectroscopic systems were used to observe the evolution of carbon impurities throughout the plasma SOL. CER, WiSE, SPRED, and MDS spectrometry systems were used to observe various charge states of carbon throughout the plasma. Shots with and without methane injection were used to compare the relative change of a signal across matched shots due to the $^{13}CD_4$ puff. This is similar in concept to the stable isotopic mixing models where an injection and control case were used. In order to quantify the relative change in signal due to the puff, a gas enhancement factor (GEF) was developed [59]. This factor was calculated for the power scan shots at various locations around the device and observed a clear increase in the spectroscopic signals. The strongest GEF and relative increases in the signals were near the outboard midplane of the device and were significantly lower in the plasma crown.

It is important to note that the GEF is modified by the introduction of enriched carbon impurities from the methane injection puff. Therefore, any variations in the wall source of enriched impurities would be incorporated into the control cases and would not modify the spectroscopic signals when methane is puffed. Considering these measurements are uncalibrated, they cannot therefore provide any indication of changes in the wall source. They can only support variations seen in the injection cases. While the stable isotopic mixing model and isotopic measurements suggest that the contributions from the enriched wall source increase with increasing power into DIII-D, this means that the contributions from the puffed impurity source decrease. One would expect the GEF to therefore decrease throughout the SOL with increasing power. Generally, little variation was observed in the GEF across the power scan from 2.5-4.5 MW. However, this is not always the case. For example, SPRED measurements of CIV, CIII, and CII at the midplane decreased across the power scan from 1.33-0.62, 0.79-0.60, and 0.81-0.48 respectively as power increased. CER measurements of the C6+ density at ψ_N~1.05 also decreased from a GEF of 0.29 to 0.20. Lower divertor MDS measurements of CIII in the SOL crown decreased with increasing power along with novel WiSE measurements of CV in the near-SOL crown with increasing power. This is consistent with the expected observations obtained with the stable isotopic mixing model and suggests that increasing power contributes to greater enriched impurity contributions from the re-eroded wall source and may suggest enriched puff source suppression with increasing power [59].

4.3 DIVIMP Simulations of Enriched ^{13}C Sources.

DIVIMP simulations of impurity density profiles throughout the SOL of DIII-D have been developed to support the interpretation of the methane injection experiments. While this is ongoing work within the research group at UTK, this section presents the early results from those simulations and uses them to support observations obtained by the collector probe measurements. More detailed descriptions of the DIVIMP code are available in the references listed in Section 1.9.

Simulations of the carbon impurity densities during the methane injection experiments are based on the diagnostic shot 187111 in Set 2 of Table 5. These simulations use a non-extended/standard plasma grid. The models are constrained by target Langmuir probe measurements as well as upstream Thomson scattering profiles. The experimental observations presented in the previous section have informed the simulations and provided further experimental constraints that assist in determining the background parameters that are shown to control impurity transport. Drift effects have been used in the simulations as well as a methane module that is able to simulate the introduction, disassociation, and resulting transport of carbon impurities throughout the SOL following introduction as molecular methane. Perpendicular diffusion coefficients have been shown to provide a key parameter for tuning the impurity density profiles and are between 0.3 and 1 m^2/s.

Two simulations are believed to be required for accurately reproducing the impurity profiles from the methane injection experiments. These include first a source at the outer strike point that is representative of the methane injection at the upper outer baffle aperture. This simulated source may also be representative of a portion of the re-eroded wall source. Previous experiments with methane injection, see reference in section 1.10, have found that carbon impurities from methane puffs are often redeposited near the source of injection. Those deposited impurities for this set of experiments are likely to be found on the plasma facing components that are near the upper outer baffle aperture and therefore near the outer strike point.

These previous methane injection studies have also found that injected carbon impurities often redeposit near the inner strike point of the plasma in addition to the area of injection. Unfortunately, tile measurements of enriched carbon impurities were not available following the methane injection experiments, so these estimates are strictly based on previous literature. With enriched deposits at the inner strike point as well, a second simulation for the enriched impurities has been developed to simulate the evolution of those impurities during the methane injection experiments. A combination of these two sources is used to provide SOL impurity profile estimates that may be used to inform 3DLIM simulations.

Inner strike point (ISP) and outer strike point (OSP) source simulations are shown in Figure 48 and Figure 49. The profiles shown in these figures represent the total carbon impurity densities during steady state conditions. The density values in each simulation grid cell are the summation of all carbon charge state densities in the plasma. While the profiles are informative, it is often the far-SOL flux surfaces or ‘rings’ at the outermost portion of the simulation, those that are closest to the walls, that may be used to inform the collector probe impurity measurements in the far-SOL. For example, consider the grid ring that is ~3 cm radially inwards from the MCP tip at the outboard midplane of the device. ISP and OSP impurity source profiles along this ring are shown in Figure 50 and Figure 51. In these figures, the number of impurity ions is presented rather than impurity density. Number of impurity ions is calculated by taking the impurity density along the ring and multiplying by the cell volume at a given distance along the ring. The raw data is plotted in black with a Savitzy-Golay filtered data set overlaid in red. These impurity number profiles are what feeds the far-SOL where the collector probes are located. It is a combination of these profiles that appears to match that shown in the expected profile, Figure 47.

When mapping the collector probe coordinates to distance along the ring from the OSP target, the DCP is located at 24.919 m along the field line from the outer target and the MCP at 9.733 m. Knowing then that the plasma volume, which is sampled by the collector probes is limited to half of the connection length, we find that both faces of the MCP and DCP have sampling lengths on the order of ~5 m and ~10 m respectively in the qualified regions of deposition. A visual representation of this concept is again presented in Figure 52 and Figure 53 for both the ISP and OSP sources. When considering the ITF source, the ITF face of the DCP is expected to sample a significantly larger number of impurities than the OTF. This is consistent with the experimental measurements for impurity deposition by LA-ICP-MS in that the ITF face of the DCP measured significantly higher impurity densities than the OTF. Note that the MCP was not affected as strongly as the DCP by the ISP source of impurities. However, the magnitude of the impurity number near the MCP is on the same order as that of the OSP source contributions to the MCP.

Now consider the OSP source simulation with the collector probes overlaid, Figure 52. This figure shows that the ISP source struggled to provide impurities upstream where the DCP is able to sample. Note that the spectroscopic GEFs were also lower in the crown where the DCP is sampling impurities. The GEFs were higher at the midplane where the MCP is able to collect impurities from the OSP source. This is consistent with the modelling in DIVIMP which show higher impurity concentration from the puffed source of impurities near the outboard midplane.

These impurity profiles agree with the magnitude of deposition that is found on the collector probes, and one can go further than saying that it is likely that these impurity profiles would result in the expected deposition patterns on the MCP and DCP. The impurity profiles may be used to constrain the impurity source definition in the 3DLIM code that simulates impurity transport near collector probes.

4.4 Introduction of 3DLIM Simulations

The 3D Monte Carlo code for far-SOL impurity transport, 3DLIM, has previously been used to replicate deposition patterns measured by ion beam techniques including Rutherford backscattering and LA-ICP-MS for the MCPs [31]. With 3DLIM, the near-SOL impurity source position can be modeled by placing the impurity source feeding into the far-SOL in different positions relative to the collector probe in the far-SOL. This section uses the DCP and a simple simulation geometry as an example of how to localize the impurity source relative to a single collector probe.

An example of the simulation source geometry is introduced in Figure 54. As the code name suggests, there are three dimensions to the simulation. The origin for the simulation is at the tip of the collector probe shown in the center of the volume. The absorbing boundaries of the simulation may be defined by the user or constrained by field line calculations of connection length. That length then defines the distance from a probe face to the absorbing boundary which is the nearest limiting surface. The axis along the center of the collector probe is synonymous with where the collector probe is located in the machine. For example, this axis would be the radial coordinate when simulating an MCP and would be the Z coordinate when simulating a DCP. The distance to the wall is defined by the collector probe exposure length, 100 mm for MCP and ~40 mm for DCP. Simulation volume along this axis that is towards the plasma core or away from the wall is typically 3 cm. In this portion of the simulation, the impurity source geometry is defined. The final dimension is the perpendicular direction relative to a field line. This is typically user defined as 6 cm in both directions.

Using 3DLIM, the far-SOL crown of the plasma during methane injection experiments can be simulated along with the DCP for a very simple geometry. In this example, the connection length is user defined to be equal in both directions towards the absorbing boundaries. By moving the poloidal position of the impurity source in the near-SOL, the relative carbon deposition on the ITF of the DCP can be compared to what is collected on the OTF in order to provide the ITF/OTF deposition ratio. Three scenarios are plausible for the outcome of the ITF/OTF deposition ratio based on the position of the impurity source position. This is similar to the discussion originally presented in section 2.6. As shown in Figure 54, there are three unique impurity source positions that vary parallel to the field lines.

Scenario 1: When this ratio is greater than 1, the accumulation is expected to be poloidally bound between the inner target and the DCP. If an accumulation is on the ITF side of the crown probe, the far-SOL flows are going to be from the accumulation region to each target. At the DCP, this flow is towards the outer target because the DCP is poloidally downstream from the stagnation point in the direction of the outer target. Therefore, a greater amount of deposition is expected on the inner target facing side of the DCP. This then drives the ITF/OTF ratio above 1. Results for this simulation are marked in blue on Figure 54.

Scenario 2: When the deposition ratio falls below 1, an accumulation poloidally bound between the DCP and the outer target is expected. As described above, it is expected that the impurities will then experience cross field transport into the far-SOL. Once the impurities radially transport further into the far-SOL and are in the poloidal portion of the plasma between the outer target and the DCP, they will then travel towards the targets due to the dominant friction force. For the DCP, impurities will now collect on the OTF in greater numbers resulting in an ITF/OTF ratio that is less than 1. Results for this simulation are marked in red on Figure 54.

Scenario 3: When this ratio is approximately equal to 1, the impurity stagnation point is expected to be centered in the near-SOL directly above the DCP. This impurity accumulation extends to both the inner target and the outer target regions resulting in transport of impurities in equal amounts to the ITF and OTF of the DiMES probe. Experimentally, the cutoff for an ITF versus OTF source might not correspond exactly to ITF/OTF=1 when the connection lengths are not equal, thus motivating further detailed analysis with 3DLIM past this simplified geometry.

Following the Metal Rings Campaign, an ITF/OTF ratio of less than 1 (Scenario 2) was the expectation when operating in an unfavorable toroidal magnetic field configuration during the methane injection experiments. During the 2016 Metal Rings Campaign, it was theorized that the near-SOL impurity accumulation would form at a poloidal position that was bound between the outboard midplane and the plasma crown when operating in an unfavorable toroidal magnetic field configuration for H-mode access [6]. While the MCP alone could not isolate this location, the addition of a DCP could assist in doing so by looking to the ITF/OTF impurity deposition ratios for each probe exposed to an accumulation in this region. If a parallel impurity accumulation were to form in the near-SOL at this location when using an unfavorable toroidal magnetic field configuration, the ITF/OTF ratio for the MCP would be dominant on the ITF or greater than 1. Conversely, this ratio would then be less than one, or OTF dominant, for a DCP when measuring a crown accumulation in an upper single null plasma using an unfavorable toroidal magnetic field.

4.5 3DLIM Simulations of ^{13}C Impurity Transport near Collector Probes

Section 4.4 describes how 3DLIM can be used to interpretively model collector probe deposition patterns based on a simple simulation volume and varying impurity source locations. The simple example may be expanded to include more detailed simulations that are based on experimental parameters. Interpretive simulations are built on a foundation of experimental constraints including the experimental deposition profiles (Figure 44 and Figure 43), electron density, and electron temperature measurements (Figure 38). In this section, additional parameters have been included and scanned in order to find a best fit reproduction of the experimental ^{13}C deposition profiles from Set 2 in Table 5. Several critical variables have been identified as those which control the shape and magnitude of far-SOL collector probe impurity deposition profiles. These include impurity source location and distribution, connection length profiles, diffusion, and convective radial velocity of the impurities. Each variable is tuned independently and with one another until not only the shape of the deposition profiles but also the relative quantities of deposited carbon on both the ITF and OTF side of the simulated collector probe match the experimental profile. Through an iterative simulation process, these variables have been varied to find best fit cases to match with the experimental patterns.

The experimental deposition patterns for the MCPs have been qualitatively recreated in 3DLIM, see Figure 55 and Figure 56. Temperature and density profiles for the simulated plasma are built using data from the reciprocating probe measurements taken during the diagnostic phase, Table 5. Connection length is determined through field line trace measurements provided by MAFOT. Connection length profiles along the length of each probe face are found to have strong correlation with the shape of each deposition profile. For example, the connection length varies across the length of each probe as the field line traces in Figure 37 are limited by different first wall surfaces. The MCP OTF plot presented in Figure 43 shows a dramatic step in the deposition measurement at R-R_{SEP} OMP ≅ 10 cm. The connection length is steady at $L_c \cong 10$ m until this point because the connection length is limited on the upper portion of the vessel as shown in Figure 37. When moving down the length of the probe, the connection length becomes limited by the wall and the MiMES port at the outboard midplane of the device and drops to L_c = 0. In 3DLIM, these steep changes in connection length are approximated by placing the absorbing boundary as shown in Figure 54, closer to the probe.

Finer tuning of the simulated deposition patterns along with the relative magnitude of carbon deposition is best matched by tuning other parameters. Impurity transport by the convective radial velocity of carbon has been scanned between 0 and 400 m/s and set to 200 m/s in the direction of the outer wall for the best fit scenario. This variable increases the rate at which particles will move in the direction of the parameter and produces a smearing effect on deposition in the same direction. Purely convective transport of impurities in the radial direction has been shown to be an adequate approximation when simulating far-SOL collector probe deposition profiles for tungsten and is further supported here for carbon impurities [30]. A rectangular source of impurities has been centered ~1.25 meters away from the collector probe towards the direction of the outer target. This is similar to scenario 2, described in section 4.4 and is aligned with the expected impurity profiles shown in Figure 47. The rigid and rectangular impurity source position was scanned on both the ITF and OTF side of the probe from half the distance to each nearest target and the space between. Source position has been shown to affect the relative deposition on the ITF and OTF. Perpendicular diffusion coefficients have been scanned from $D_\perp$ = 0 to 3.2 m^2/s. The best fit match to the experimental deposition profile has been reproduced using $D_\perp$ = 1.6 m^2/s for this case. In 3DLIM, the perpendicular direction is the same as the poloidal (θ) direction shown in Figure 54 where poloidal is described as perpendicular to $B_\parallel$. When increasing $D_\perp$, impurities are able to deposit more uniformly over the collector probe collection surface due to greater forces imposed on the impurities in the perpendicular or poloidal direction. Low $D_\perp$ simulations show higher carbon deposition at the poloidal extremes of each collector probe. Increasing this parameter forces impurities deposited at the edge more towards the centerline of the collector probe. This effect is presented in Figure 56 to show the centerline variations that are observed with 3DLIM parameter scans. This poloidal variation in the deposition profile has been experimentally observed and discussed in [23, 31]. In Figure 56, the experimental profile is the same MCP OTF profile presented in Figure 43. The best fit simulated deposition profile at $D_{\perp}$ = 1.6 m^2/s is fit to the experimental data. The remaining simulated patterns are overlaid as well in order to show the relative changes in centerline deposition with varying $D_{\perp}$. While the simulated pattern deviates from the experimental pattern at R-R_{SEP} OMP = 9 cm, increasing deposition is expected with decreasing R-R_{SEP} OMP in order to match the shape of the L_C pattern.

Tuning parameters listed above have reproduced the shape of the deposition profiles on both the ITF and OTF faces of the collector probes as well as the ITF/OTF deposition ratio for the MCPs exposed to collection phase plasmas in Table 5. Again, each 3DLIM parameter was scanned independently and in a matrix with the others until the best fit profile in both Figure 55 and Figure 56 were produced. When comparing deposition profiles for individual collection phases listed in Table 5, each of these have ^{13}C deposition profiles that are similar in shape to those in Figure 56 but different in magnitude and ITF/OTF deposition ratios. When calculating the ITF/OTF ratio, it is important to compare data where erosion is not a significant factor. Therefore, in order to calculate the ITF/OTF deposition ratio, the impurity deposition directly following the erosion point at R-R_{SEP} OMP ≅ 9 cm is most qualified for comparison. See 4.2 for further discussion on qualified analysis regions. MCP impurity deposition profiles, for those listed in Table 5 have an ITF/OTF deposition ratio in this qualified region that is less than one. These results differ from the initial expectations following the observations made during the DIII-D Metal Rings Campaign and 3DLIM is used to interpret these results below. Variations in these ratios have also been observed with changes in injected power as well and variations in the contributions from different enriched sources. For the MCPs these ratios were more OTF dominant with increasing power. Results shown in Figure 57.

When looking to Figure 43, the ITF/OTF deposition ratio is clearly ITF dominant across the full length of the DCP. This supports the concept of an ITF dominated source that is feeding the deposition to collector probe in the crown. Unlike the trend found with the stable isotopic mixing model, there do not appear to be any clear trends in the magnitude of tracer impurity deposition with injected power for the DCP. As a result, a trend in the deposition ratio is not observed or presented in Figure 57 for the DCPs. Using the expected source profiles to simulate deposition patterns in 3DLIM, we find good agreement between the experimental deposition profiles and the simulated patterns. The simulated impurity deposition patterns are shown in Figure 58. The ITF appears to have greater deposition along the ITF of the probe when using the expected impurity source in 3DLIM. With little to no impurity content bound between the MCP and the DCP, the OTF face of the DCP shows little to no deposition relative to the ITF.

When considering both ITF/OTF ratios for MCPs and DCPs together, a bifurcated impurity source feeding the far-SOL collector probes may be present in the methane injection experiments when following the description in Chapter 3. Increased impurity density in multiple regions aligns with the expected source as well, Figure 47. This is because the ITF/OTF ratio for each probe is suggesting a source of impurities that is poloidally bound between each probe and the nearest target i.e. the DCP deposition follows scenario 1, while the MCP most resembles scenario 2.

4.6 Methane puff suppression discussion

When combining the results from this chapter, it appears as though increased power into DIII-D plasmas results in suppression of the methane injection puff. In fact, it is as if there are two sources at the outer target of enriched impurities that are actuated with increasing power. There is the near strike point source that is comprised of enriched deposits from the previous injections of enriched methane. Then there is also the puff of methane that accounts for a far strike point source as it is introduced at the location of the upper outer baffle plenum aperture. While power increases, the near strike point source increases in contribution to the upstream impurity density profiles throughout the plasma SOL and simultaneously the far strike point source from the puff is suppressed.

3DLIM has also been used to reproduce the ITF/OTF ratios that have been observed to become more OTF dominant with increasing injected power. Rigidly shifting the simulated impurity source towards the outer target has best reproduced the ITF/OTF trend seen in the MCP experimental deposition profiles of Figure 57. An example of this

ITF/OTF trend with a shifted source is presented in Figure 59. The ITF/OTF ratio is shown for a series of simulations that shift the location of the impurity source as is described in Chapter 3. However, the source of impurities for this case is shifted poloidally or along $B_{\|}$ and away from the MCP in the direction of the outer target. This source shift in 3DLIM has the effect of increasing deposited carbon impurities on the outer target face of the MCP while simultaneously decreasing the source of impurities feeding the ITF of the MCP. The further the source is shifted towards the outer target and away from the MCP, the more dominant the OTF deposition becomes in the simulated deposition profiles. Experimentally, these 3DLIM results suggest a relative increase in the amount of ^{13}C feeding into the far-SOL from between the outer target and the MCPs compared to the region poloidally bound between the two probes.

When looking to the results from the stable isotopic mixing model, it is again the contributions from each enriched source that vary with injected power. For the DCP, the re-eroded wall source contributes greater to the upstream impurity density profiles compared to the puffed source. However, when looking to the impurity density profiles for the OSP source, the impurities to not appear to reach the plasma volume on the ITF of the DCP that feeds the deposition profiles. The SIMM model shows that low power cases should have a nearly 50-50 mixture of deposits from puffed impurities as well as re-eroded wall impurities. Simulations for DIVIMP like those shown in Figure 60 and Figure 61 may help explain this feature. Notice this profile is similar to that of the OSP source previously presented. However, now the impurities are introduced in the simulation directly adjacent to the strike point at the outer target. Impurities in the near-SOL are again driven by strong parallel temperature gradients. Therefore, if impurities from the puff are able to leak and ionize in the near-SOL, it is likely that they are then able to reach upstream and contribute to the impurity deposition profiles on the ITF of the DCP.

However, with increasing power, impurities from the puff are believed to be suppressed and the re-eroded wall source again contributes more to the upstream impurity density profiles. How can this be so? It could be that the impurities from the wall have a higher erosion rate with increasing power as is expected. This again likely accounts for the increased wall source. There could also be changes in the perpendicular transport with increasing power that causes the impurities in the plenum to be more and more suppressed such that they are not able to reach the inner strike point where the strong parallel temperature gradients drive the impurities upstream and into the crown accumulation. Drifts and perpendicular diffusion are likely both knobs that we can tune to see the effects on the impurity profiles. This then aligns with the experimental expectations where the MCP and DCP have more and more enriched wall deposits with increasing power because the puffed source is being suppressed.

Assuming the distribution of the impurity source is above the midplane and moves towards the target with increasing power, as is suggested by the ITF/OTF deposition on the MCP, there are several mechanisms which may explain these results. Methane gas has been used for these experiments and is expected to behave differently in comparison to tungsten impurities that were introduced by sputtering during the DIII-D Metal Rings Campaign. Devices such as JET have previously shown an increase in divertor carbon sources with increased heating power during methane injection experiments [60]. At lower temperatures, there may be stronger coupling with the impurity ions and the fuel species that results in increased divertor retention of the impurities. As power is increased, the collisions are no longer as effective in retaining carbon and may release additional impurities as a near-SOL/near target source that contributes to the upstream impurity density profiles. Therefore, the MCP OTF ratios would increase with increasing injected power as is shown in Figure 57 while also suppressing the puffed source.

This concept of puff suppression with increasing power is under further investigation. With increased re-eroded impurities, there may also be change in the pressure that causes competing forces with the puffed impurities. Impurity-impurity collisions, effects of diffusion, and effects of drifts are all open avenues of research that could explain why this phenomenon is occurring. This is ongoing work, but we now have a better grasp on what is likely occurring based on empirical evidence through spectroscopy and collector probe measurements that is consistent with simulations in DIVIMP and 3DLIM.

CHAPTER FIVE
CONCLUSIONS AND RECOMMENDATIONS

5.1 Overview

The work here has addressed impurity sourcing and transport throughout the scrape-off-layer of DIII-D. There are many avenues going forward for additional research that can build on the work completed for this dissertation. Additional studies should consider coupling with the core reservoir. Additional studies using DIVIMP/3DLIM may be used to inform the radial transport description in AURORA using an outside in approach. Additionally, upcoming experiments on DIII-D will again have the opportunity to work with tungsten. This is easier to use as a tracer impurity rather than carbon impurities in a carbon device. With tungsten and the new tile geometry in DIII-D for the SAS divertor, there are opportunities to assess the effect of divertor closure and detachment. The new MCP and DCP designs may also be used in these configurations and early results are favorable for impurity transport studies.

5.2 Future Efforts and Recommendations

AURORA is another useful tool for evaluating the plasma impurity characteristics. The code is one dimensional in that it solves the radial continuity equation for each ionization stage of the observed impurity. ADAS ionization and recombination rates are used for each state in order to provide time evolved impurity densities. There are options for full neoclassical handling of the transport if desired. Input into the code is required, but with DIII-D this process has been streamlined through OMFIT. With the OMFIT, background plasmas can be imported directly from DIII-D MDS+ discharge data. Shots and time stamp inputs are required to build an equilibrium profile. Plasma kinetic profiles of T_e and n_e are also needed for input into the code. Conveniently there are input options for time-dependent impurity sources that are injected through the gas puffing valves. These may also be user defined based on observed impurity sourcing rates. This code may be used to couple the core impurity transport and reservoir with the SOL and source reservoirs. This then begins to introduce a full particle balance and impurity transport description.

The penetration factor or effective screening of impurities may also be considered in future efforts. This term is the ratio of the impurity content inside the closed flux surfaces to the impurity influx from the divertor target [61-63]. The term is quite simple and is able to provide an estimate of how well impurities are retained within the divertor. For example, a low penetration factor implied good divertor retention. For non-recycling impurities, like tungsten, it is the injection rate rather than the number of introduced impurity particles that is used in the calculation. Previous work has shown this to be important for non-recycling materials [62]. One example of a study could consider the ∇B effect on the penetration factor with a symmetric source of impurities that are sourced at the divertor [63]. For these studies, similar impurity source rates would be important to match from one shot to the next. This means the strike point location, density, current, injected power, and plasma parameters should match with the primary difference being the direction of the toroidal magnetic field. Fortunately, DIII-D now offers a shot to shot B_T switch.

In order to obtain the tungsten impurity sourcing rates from the tungsten coated tiles, spectroscopic measurements are needed to provide these estimates. Recent work has developed these capabilities at DIII-D and within the group at UTK [64, 65]. Filterscopes are a diagnostic set capable of measuring spectral line emissions of W-I at 400.9 nm. Using the S/XB coefficient for a given n_e and T_e measurements at the strike point location, tungsten erosion rates may be estimated for these calculations. While these estimates are typically for a given area of the tile surface in using of atoms/cm^2 s, the tile annulus may be easily calculated and used to provide the number of atoms/s. These methods work with both L-mode and H-mode plasmas in that they typically have a time resolution of 0.1 ms which allows for intra-ELM and inter-ELM rates. However, different S/XB coefficients are required for this analysis.

For penetration factor calculations, core impurity measurements are typically interested in the number of core impurity particles, N_W. This term is not as straight-forward to obtain. However, one could multiple the readily available core electron inventory by the core tungsten concentrations in order to estimate the number of tungsten ions in the core [66]. There are several methods to obtain core tungsten concentrations. The first uses

AURORA as described above. Perhaps a simpler approach is to use SXR analysis using pyTomo [67, 68]. As stated in the code description, “pyTomo is an advanced code for tomographical inversion from various integrated diagnostics like SXR or bolometers. The main advantages are a simple GUI, very fast inversion and a high accuracy (depends on the quality of the input data). Details can be found on the DIII-D software page https://diii-d.gat.com/diii-d/PyTomo. SXR and bolometry measurements are automatically incorporated into the code. Kinetic profiles must be developed as input as well. The output is a time varying, radial profile of impurity concentration within the core. These profiles may then be used to provide the number of core impurity estimates for calculating the tungsten penetration factor. Often, L-mode shots do not produce sufficient tungsten sourcing and this analysis is often limited to H-mode conditions.

Collector probes should also be used at both the midplane and crown locations when possible. Experiments for the 2022-2023 run campaign already plan to use the new collector probe designs developed in this dissertation. Early shots in the campaign have used the collector probes during startup shots where the strike point was placed on tungsten rings in the upper divertor. The collector probes used during these shots revealed significant levels of tungsten deposition across all faces of the collector probes. Deposition was several orders of magnitude greater than during the DIII-D Metal Rings Campaign. This is good news for collector probes and impurity transport studies. Many of the analysis methods and work developed during the analysis of the metal rings campaign experiments will once again be applicable to these upcoming experiments studying tungsten transport on DIII-D [23].

As mentioned in Chapter 3, LA-ICP-MS often suffers from a lack of available standard reference materials that may be used to provide high-resolution areal density measurements of the individual tungsten isotopes across a collector probe surface. While not applicable to carbon isotopes, tungsten reference materials have been developed to address this need when using the LA-ICP-MS technique and will again be of use in the coming campaign. A technical manuscript on this work has been submitted for review at

ORNL and is titled, “Development and Qualification of Tungsten Reference Materials for LA-ICP-MS”.

5.3 Lessons Learned During the Methane Injection Experiments

There were many experimental results related to the physics of impurity transport presented within this work, but there were also many technical accomplishments that come with cautionary tales for future experiments of similar design. This section reviews some of those issues so that others may avoid the pitfalls involved with similar studies.

Carbon did not behave like a “Non-recycling impurity” in the Methane Injection Experiments: Perhaps the most glaring issue is related to the use of the term non-recycling impurities when describing carbon. Several times throughout the earlier sections of this dissertation, we find references to carbon as a non-recycling impurity. Sections 1.5 and 2.7, which are based on existing literature, describe carbon as non-recycling with a low probability to backscatter into the plasma following interaction with a material surface. This description states that we could expect to assume a once-through nature of carbon impurities before they become stuck to a physical surface. Additionally, the non-recycling nature is also defined with a low wall recycling fraction that is expected to again be representative of the sink action of the walls that does not allow re-deposited carbon back into the system. These early descriptions of carbon impurities obviously disagree with the major findings of this work that are described in the abstract and restated here, “Modelling by DIVIMP and 3DLIM of ^{13}C SOL evolution is consistent with diagnostic observations and indicates that the buildup of injected impurities on plasma-facing surfaces must be considered while inferring representative impurity distributions. Namely, ^{13}C deposits on the inner and outer targets are shown to contribute 50% at a minimum of the enriched ^{13}C deposition on CPs and to cause poloidal shifting of the impurity density peaks in the near-SOL.” While this hysteresis effect of carbon impurities was not previously predicted, this highlights an area of improvement that has been emphasized throughout the results of this work and should be considered during future impurity transport experiments. For additional clarification, if one is only injecting natural carbon, rather than isotopically enriched carbon isotopes, in a device like DIII-D that is comprised of natural graphite tiles, then for all practical purposes carbon is non-recycling. In this scenario, there is no way to distinguish the natural injected carbon ions that deposit, sputter, and re-enter the plasma from the carbon sputtered from the tiles themselves. For the methane injection experiments, where enriched ^{13}C is injected into a vessel armored by natural carbon tiles, carbon is effectively a 'recycler'.

Use of methane requires detailed understanding of molecular dissociation: Carbon also has other intricacies that complicate the impurity transport picture when introduced as a molecular species. The use of methane injection introduces the issue of needing to understand the complex processes involved with molecular dissociation. While there are modules in code packages designed to simulate the evolution of methane to carbon and hydrogen ions, it is much simpler to install solid material surfaces for impurity transport experiments in a similar fashion to the 2016 DIII-D Metal Rings Campaign and like that of the 2022 DIII-D SAS-VW experiments. While future fusion systems plan to use low-Z materials like carbon and beryllium, tungsten is currently the leading candidate material for divertor plasma facing components and will be used in the divertor cassette systems in the ITER tokamak that is currently under construction. That is to say tungsten and nearby metallic elements on the periodic table such as molybdenum, rhenium, and other could be valuable substitute source materials that come with advantages over carbon sourced via methane injection. This is especially true if enriched isotopes of the elements can be acquired affordably and there are well characterized spectroscopic lines of the impurity which may be observed in different regions of the plasma while in transit.

More controlled impurity injection is preferred: Future experiments on impurity transport may also benefit from removing the divertor sourcing component from the experiment all together. If one can instead locally deposit unique isotopic impurities within the plasma core and then observe the evolution of those impurities throughout the plasma through similar methods presented here, one would no longer have to concern over the complex divertor mechanisms discussed in Chapter 4. Impurity pellet experiments are another possible evolution of this work. Development of methods for producing pellets that are comprised of impurities encapsulated in some ablation layer would be a major boon to this type of experiment. Some recent efforts have attempted to coat natural tungsten with Kapton. These pellets were then injected into DIII-D while collector probes were exposed to collect the tungsten impurities. Unfortunately, a control probe was not used to characterize the background signal of tungsten impurities, so it is difficult to say for certain that the collector probes measurements were strictly from tungsten sourced within the plasma core. Well-designed experiments using a control case and even isotopically enriched tungsten impurities that is confirmed to ionize and source within the plasma core are an excellent next step series of experiments following this work.

Ensure overlapping sampling lengths for dual collector probe system: There are valuable lessons to be learned from these pioneering experiments with a dual collector probe system. It is important to ensure that the probes at the outboard midplane and the crown are sampling similar portions of the SOL. This requires mapping the position of the collector probes to R-R_{SEP} OMP positions and ensuring overlap. The position the collector probes has additional requirements which involve a delicate balance of avoiding insertion of the collector probes too close to the plasma separatrix while also ensuring adequate sampling lengths on both faces of both probes. Insertion of the collector probe too deep into the plasma (too close to the separatrix) often results in ablation of the deposited materials which eliminates any usefulness of the diagnostic. Past designs which used the plate inserts had thin features which would likely have cracked and could have introduced graphite fragments into DIII-D. Solid probes with 3 cm diameter have not encountered this issue to date. Instead, the solid probe typically just ablates, resulting in loss of the deposited impurities. This mechanical failure was a major concern during the diagnostic approval process at DIII-D. If the probe were to fracture and a portion were to enter the device, there are scenarios where the graphite could damage other components within DIII-D. This is why a diagnostic phase prior to use is essential in preventing over extension of the collector probes into the plasma. Field line traces of the probes should also be performed using the MAFOT code in order to establish the connection lengths from each probe face. This may be performed using the magnetic equilibria of the diagnostic phase prior to exposure of the collector probes. To date, there are now several examples of upper-single-null plasmas that are ideal for using the collector probes (note that the DiMES Collector Probe was not designed for and is not appropriate for lower single null plasma configurations without conducting a new engineering/design review and approval). Those presented in this work for example were fantastic in providing field line traces from both faces of the probes that cleared nearby limiting features of the wall geometry within DIII-D. Of course, these plasma shapes may not be possible to recreate when using the small angle slot divertor on DIII-D or any wall changes that may occur in the future.

5.4 Conclusions

This work addresses the near-SOL and far-SOL reservoirs and the impact of multiple sources on SOL impurity profiles. The combined efforts of both experiments and simulations are found to be consistent with one another in interpreting near-SOL impurity density profiles. Through the use of multiple collector probes, our ability to interpret near-SOL impurity profiles based on far-SOL impurity deposition measurements has been enhanced. Using dual collector probes has elucidated important information that would have otherwise been impossible to observe with a single probe at the midplane of the device. 3DLIM is shown to be a useful tool for predicting near-SOL impurity behavior and interpreting experimental results when coupled with collector probes.

Future experiments which use the MCP and DCP combination should take extra steps in ensuring the probes are in plasma that will not compromise the deposition measurements. H-mode plasmas may be beneficial for inserting probes closer to the separatrix due to their steeper radial temperature gradients. However, the effects of edge localized modes should be investigated for the DCP considering MCPs were used in H-mode plasmas during the DIII-D Metal Rings Campaign. H-mode would also introduce greater injected power levels and may therefore show an increase in the carbon that is able to contact the collector probes. The upcoming experiments involving the SAS-VW campaign at DIII-D are especially interesting for expanding on this work with a midplane and crown collector probe assembly.

DIII-D presents unique opportunities for understanding impurity transport throughout a tokamak plasma. Tokamak divertors and scrape-off-layers introduce new issues that result in impurities contaminating the core of the plasma. We must better understand the mechanisms that lead to this process. Isotopically tagged methane injection studies using axisymmetric introduction offers a valuable solution for characterizing what happens during the lifetime of an impurity on the timescale of a single plasma discharge. Previous methane injection studies on the device have looked at campaign integrated results and observed tile deposition patterns along with co-deposition. Here the goal was to utilize my newly designed DiMES and MiMES collector probes in order to directly sample the DIII-D SOL during the $^{13}CD_4$ injection experiments at DIII-D. Using non-recycling impurities, this offers a unique solution for no longer looking at campaign integrated information that pertains to impurity transport. Instead, this offers a shot integrated look at impurity migration directly throughout the plasma edge. Methods such as LA-ICP-MS, developed at ORNL, assist in characterization of the sample deposition between shots in conjunction with ion beam measurements. Collector probe asymmetries shed light on processes that we believe result in an impurity accumulation well in the SOL that feed these collector probe deposition patterns. With the wide array of diagnostics that are available on DIII-D we have also monitored the time evolution of various carbon charge states that are consistent with collector probe observations and simulated impurity profiles. These combined efforts forward the understanding of impurity transport in the SOL and bring the community closer towards the goal of understanding the impurity transport process that may lead to mitigation techniques of core cooling via radiative processes.

LIST OF REFERENCES

1. Sheffield, J., *The physics of magnetic fusion reactors.* Reviews of Modern Physics, 1994. **66**(3): p. 1015-1103.
2. Federici, G., et al., *Plasma-material interactions in current tokamaks and their implications for next step fusion reactors.* Nuclear Fusion, 2001. **41**(12): p. 1967-2137.
3. Stangeby, P.C., *The Plasma Boundary of Magnetic Fusion Devices*. 2000: Taylor & Francis.
4. Neuhauser, J., et al., *Modelling of impurity flow in the tokamak scrape-off layer.* Nuclear Fusion, 1984. **24**(1): p. 39.
5. Stangeby, P.C. and J.D. Elder, *Impurity retention by divertors. I. One dimensional models.* Nuclear Fusion, 1995. **35**(11): p. 1391-1412.
6. Elder, J.D., et al., *Evidence of near-SOL tungsten accumulation using a far-SOL collector probe array and OEDGE modelling in the DIII-D metal rings L-mode discharges.* Nuclear Materials and Energy, 2019. **19**: p. 287-294.
7. Donovan, D.C., et al., *Utilization of outer-midplane collector probes with isotopically enriched tungsten tracer particles for impurity transport studies in the scrape-off layer of DIII-D (invited).* Review of Scientific Instruments, 2018. **89**(10): p. 10I115.
8. Zamperini, S., et al., *Transport of tungsten to collector probes in DIII-D.* Nuclear Materials and Energy, 2019. **18**: p. 87-92.
9. Wesson, J., *Tokamaks*. 2011, Oxford : Oxford University Press: Oxford.
10. Nichols, J.H. *DIVIMP-WallDYN modeling of W migration in the DIII-D divertor*. in *60th APS-DPP*. 2018. Portland, OR.
11. Hakola, A., et al., *Global migration of impurities in tokamaks.* Plasma Physics and Controlled Fusion, 2013. **55**(12): p. 124029.
12. Boivin, R.L., et al., *DIII-D Diagnostic Systems.* Fusion Science and Technology, 2005. **48**(2): p. 834-851.

13. Ding, R., et al., *High-Z material erosion and its control in DIII-D carbon divertor.* Nuclear Materials and Energy, 2017. **12**: p. 247-252.
14. Wood, R. and S. L. Allen, *Absolute calibration of a SPRED (Spectrometer Recording Extended Domain) EUV (extreme ultraviolet) spectrograph for use on the DIII-D tokamak*. 2019.
15. Wasa, T., et al., *Collector probe measurements in T-10: Results and prospects.* Journal of Nuclear Materials, 1989. **162-164**: p. 51-62.
16. Rubel, M., et al., *Overview of wall probes for erosion and deposition studies in the TEXTOR tokamak.* Matter and Radiation at Extremes, 2017. **2**(3): p. 87-104.
17. Wong, C., et al., *Divertor materials evaluation system at DIII-D*. Vol. 196. 1992. 871-875.
18. Wong, C.P.C., et al., *Divertor and midplane materials evaluation system in DIII-D.* Journal of Nuclear Materials, 2007. **363-365**: p. 276-281.
19. Rudakov, D.L., et al., *DiMES PMI research at DIII-D in support of ITER and beyond.* Fusion Engineering and Design.
20. R. Wampler, W., et al., *Measurements of carbon, deuterium and boron deposition in DIII-D*. Vol. 337. 2005. 134-138.
21. R. Wampler, W., et al., *Transport and deposition of 13C from methane injection into partially detached H-mode plasmas in DIII-D*. Vol. 363. 2007. 72-77.
22. Wampler, W.R., et al., *Ion beam analysis of13C and deuterium deposition in DIII-D and their removal byin-situoxygen baking.* Physica Scripta, 2011. **T145**: p. 014025.
23. Duran, J.D., et al., *Multiple Analytical Approach to Isotopic Transport Analysis in Magnetic Fusion Devices*. Fusion Science and Technology, 2019. **75**: p. 493-498.
24. Stangeby, P.C., et al., *Interpretive modeling of simple-as-possible-plasma discharges on DIII-D using the OEDGE code.* Journal of Nuclear Materials, 2003. **313–316**: p. 883-887.
25. Elder, J.D., et al., *OEDGE modeling of 13C deposition in the inner divertor of DIII-D.* Journal of Nuclear Materials, 2005. **337-339**: p. 79-83.

26. Elder, J.D., et al., *OEDGE modeling of the DIII-D H-mode 13CH4 puffing experiment.* Journal of Nuclear Materials, 2007. **363-365**: p. 140-145.

27. McLean, A.G., et al., *DIVIMP modeling of the toroidally symmetrical injection of 13CH4 into the upper SOL of DIII-D.* Journal of Nuclear Materials, 2005. **337-339**: p. 124-128.

28. Stangeby, P.C., et al., *Measurements of the average energy of carbon atoms released from breakup of methane in the main SOL of DIII-D compared with DIVIMP code modeling.* Journal of Nuclear Materials, 2007. **363-365**: p. 201-205.

29. Makkonen, T., et al., *DIVIMP simulations of 13C puffing experiments in ASDEX Upgrade L-mode plasma.* Journal of Nuclear Materials, 2011. **415**(1, Supplement): p. S479-S482.

30. Zamperini, S.A., et al., *The role of B T-dependent flows on W accumulation at the edge of the confined plasma.* Nuclear Fusion, 2022. **62**(2): p. 026037.

31. Zamperini, S.A., et al., *Reproduction of collector probe deposition profiles using the far-SOL impurity transport code 3DLIM.* Nuclear Materials and Energy, 2020. **25**: p. 100811.

32. C. Stangeby, P., *Assessing material migration through 13C injection experiments*. Vol. 415. 2011.

33. Sciortino, F., et al., *Modeling of particle transport, neutrals and radiation in magnetically-confined plasmas with Aurora.* Plasma Physics and Controlled Fusion, 2021. **63**(11): p. 112001.

34. Unterberg, E.A., et al., *Use of isotopic tungsten tracers and a stable-isotope-mixing model to characterize divertor source location in the DIII-D metal rings campaign.* Nuclear Materials and Energy, 2019. **19**: p. 358-363.

35. Brooks, N.H., et al., *Carbon influx in He and D plasmas in DIII-D.* Journal of Nuclear Materials, 1999. **266-269**: p. 732-738.

36. Canik, J.M., et al., *Testing the role of molecular physics in dissipative divertor operations through helium plasmas at DIII-D.* Physics of Plasmas, 2017. **24**(5): p. 056116.

37. Samuell, C.M., et al., *2D imaging of helium ion velocity in the DIII-D divertor.* Physics of Plasmas, 2018. **25**(5): p. 056110.

38. Pitts, R.A., et al., *Comparing scrape-off layer and divertor physics in JET pure He and D discharges.* Journal of Nuclear Materials, 2003. **313-316**: p. 777-786.

39. Roth, J., K. Krieger, and G. Fussmann, *Divertor retention for recycling impurities.* Nuclear Fusion, 1992. **32**(10): p. 1835.

40. Loarer, T., et al., *Particle balance modelling in ergodic divertor experiments on Tore Supra.* Journal of Nuclear Materials, 1997. **241**: p. 505-510.

41. LaBombard, B., et al., *Cross-field plasma transport and main-chamber recycling in diverted plasmas on Alcator C-Mod.* Nuclear Fusion, 2000. **40**(12): p. 2041.

42. Sakamoto, M., et al., *Global particle balance and wall recycling properties of long duration discharges on TRIAM-1M.* Nuclear Fusion, 2004. **44**(7): p. 693-698.

43. Wade, M.R., et al., *Impurity enrichment studies with induced scrape-off layer flow on DIII-D.* Nuclear Fusion, 1998. **38**(12): p. 1839-1859.

44. Elder, J.D., et al., *Indications of an inward pinch in the inner SOL of DIII-D from 13C deposition experiments.* Journal of Nuclear Materials, 2009. **390-391**: p. 376-379.

45. LaBombard, B., et al., *Cross-field plasma transport and main-chamber recycling in diverted plasmas on Alcator C-Mod.* Nuclear Fusion, 2000. **40**(12): p. 2041-2060.

46. Terry, J.L., et al., *The Scrape-Off Layer in Alcator C-Mod: Transport, Turbulence, and Flows.* Fusion Science and Technology, 2007. **51**(3): p. 342-356.

47. Wingen, A., T.E. Evans, and K.H. Spatschek, *High resolution numerical studies of separatrix splitting due to non-axisymmetric perturbation in DIII-D.* Nuclear Fusion, 2009. **49**(5): p. 055027.

48. Rudakov, D.L., et al., *Far scrape-off layer and near wall plasma studies in DIII-D.* Journal of Nuclear Materials, 2005. **337-339**: p. 717-721.

49. LaBombard, B., et al., *Toroidal rotation as an explanation for plasma flow observations in the Alcator C-Mod scrape-off layer.* Journal of Nuclear Materials, 2003. **313-316**: p. 995-999.

50. Dux, R. and A.G. Peeters, *Neoclassical impurity transport in the core of an ignited tokamak plasma.* Nuclear Fusion, 2000. **40**(10): p. 1721-1729.

51. Pütterich, T., et al., *Calculation and experimental test of the cooling factor of tungsten.* Nuclear Fusion, 2010. **50**(2): p. 025012.

52. Schustereder, W., et al., *Discharge resolved impurity flux measurements in the edge plasma of ASDEX Upgrade by exposure of collector probes.* Journal of Nuclear Materials, 2007. **363**: p. 242-246.

53. Unterberg, E.A., et al., *Localized divertor leakage measurements using isotopic tungsten sources during edge-localized mode-y H-mode discharges on DIII-D.* Nuclear Fusion, 2019. **60**(1): p. 016028.

54. Watkins, J.G., et al., *A fast scanning probe for DIII–D.* Review of Scientific Instruments, 1992. **63**(10): p. 4728-4730.

55. Duran, J.D., *13C surface characterization of midplane and crown collector probes on DIII-D.* Nuclear Materials and Energy, (In Review).

56. Watkins, J.G., et al., *Fast reciprocating Langmuir probe for the DIII-D divertor.* Review of Scientific Instruments, 1997. **68**(1): p. 373-376.

57. Bock, L., et al., *Comparison of the influence of 2D and 3D geometry of the main chamber on plasma parameters in the SOL of ASDEX Upgrade.* Nuclear fusion, 2022. **62**(2): p. 26020.

58. Savitzky, A. and M.J.E. Golay, *Smoothing and Differentiation of Data by Simplified Least Squares Procedures.* Analytical Chemistry, 1964. **36**(8): p. 1627-1639.

59. Nichols, J.H., *Spectroscopic observations of carbon transport in the near scrape-off-layer following controlled axisymmetric injection of methane in DIII-D*, in *63rd Annual Meeting of the APS Division of Plasma Physics*. 2021.

60. Strachan, J.D., *Jet carbon screening experiments using methane gas puffing and its relation to intrinsic carbon impurities.* Nuclear Fusion, 2003. **43**(9): p. 922-941.
61. Janeschitz, G., et al., *Divertor performance on carbon and beryllium targets in JET.* Journal of Nuclear Materials, 1992. **196-198**: p. 380-385.
62. Granetz, R.S., et al., *A comparison of impurity screening between limiter and divertor plasmas in the Alcator C-Mod tokamak.* Journal of Nuclear Materials, 1997. **241**: p. 788-792.
63. West, W.P., et al., *Methane penetration in DIII-D ELMing H-mode plasmas.* Journal of Nuclear Materials, 2003. **313-316**: p. 1211-1215.
64. Abrams, T., et al., *Advances in Low-Temperature Tungsten Spectroscopy Capability to Quantify DIII-D Divertor Erosion.* IEEE Transactions on Plasma Science, 2018. **46**(5): p. 1298-1305.
65. Abrams, T., et al., *Experimental validation of a model for particle recycling and tungsten erosion during ELMs in the DIII-D divertor.* Nuclear Materials and Energy, 2018. **17**: p. 164-173.
66. Neu, R., et al., *Impurity behaviour in the ASDEX Upgrade divertor tokamak with large area tungsten walls.* Plasma Physics and Controlled Fusion, 2002. **44**(6): p. 811-826.
67. Odstrcil, M., et al., *Modern numerical methods for plasma tomography optimisation.* Nuclear Instruments and Methods in Physics Research Section A: Accelerators, Spectrometers, Detectors and Associated Equipment, 2012. **686**: p. 156-161.
68. Odstrčil, T., et al., *Optimized tomography methods for plasma emissivity reconstruction at the ASDEX Upgrade tokamak.* Review of Scientific Instruments, 2016. **87**(12): p. 123505.
69. Wirth, B.D., et al., *Fusion materials modeling: Challenges and opportunities.* MRS Bulletin, 2011. **36**(3): p. 216-222.
70. Stacey, W.M., *Fusion Plasma Physics*. 2012: Wiley.

71. *Spectral Lines*. 2017 [cited 2019 March 5]; Available from: https://diii-d.gat.com/diii-d/Divspred_lines.

72. Emmoth, B., et al., *In-situ measurements of carbon and deuterium deposition using the fast reciprocating probe in TEXTOR.* Journal of Nuclear Materials, 2009. **390-391**: p. 179-182.

73. *CRC Handbook of Chemistry and Physics, 84th Edition Edited by David R. Lide (National Institute of Standards and Technology). CRC Press LLC: Boca Raton. 2003. 2616 pp. $139.95. ISBN 0-8493-0484-9.* Journal of the American Chemical Society, 2004. **126**(5): p. 1586-1586.

APPENDIX

APPENDIX 1: FIGURES

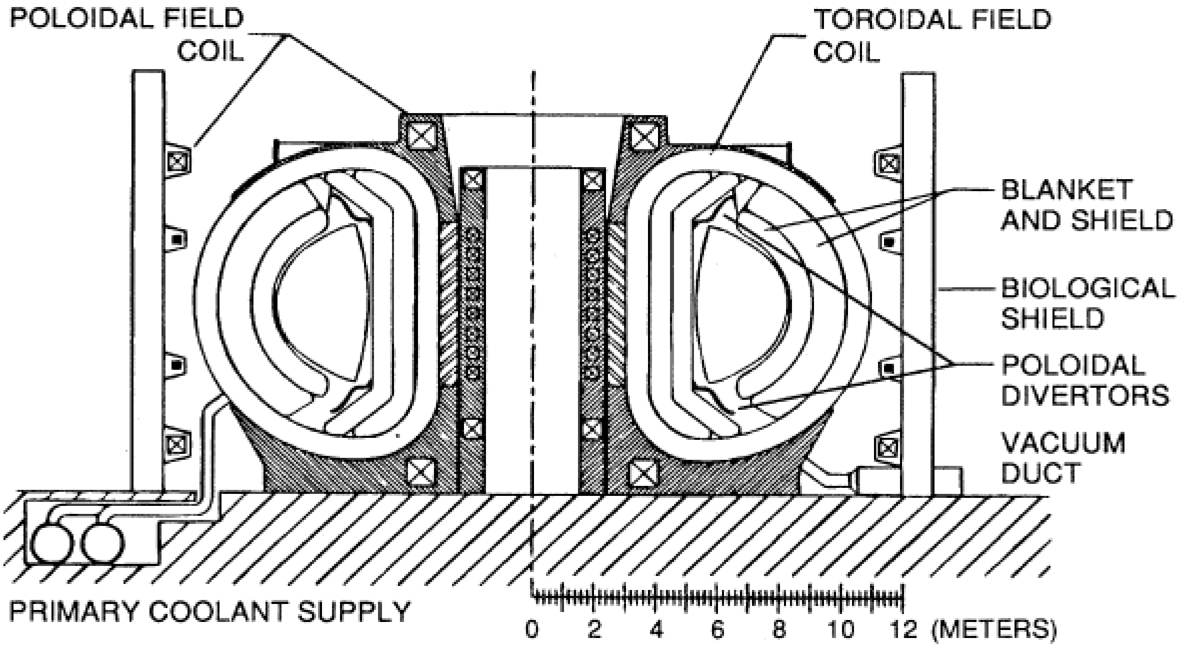

Figure 1. Cross section schematic of a representative tokamak reactor

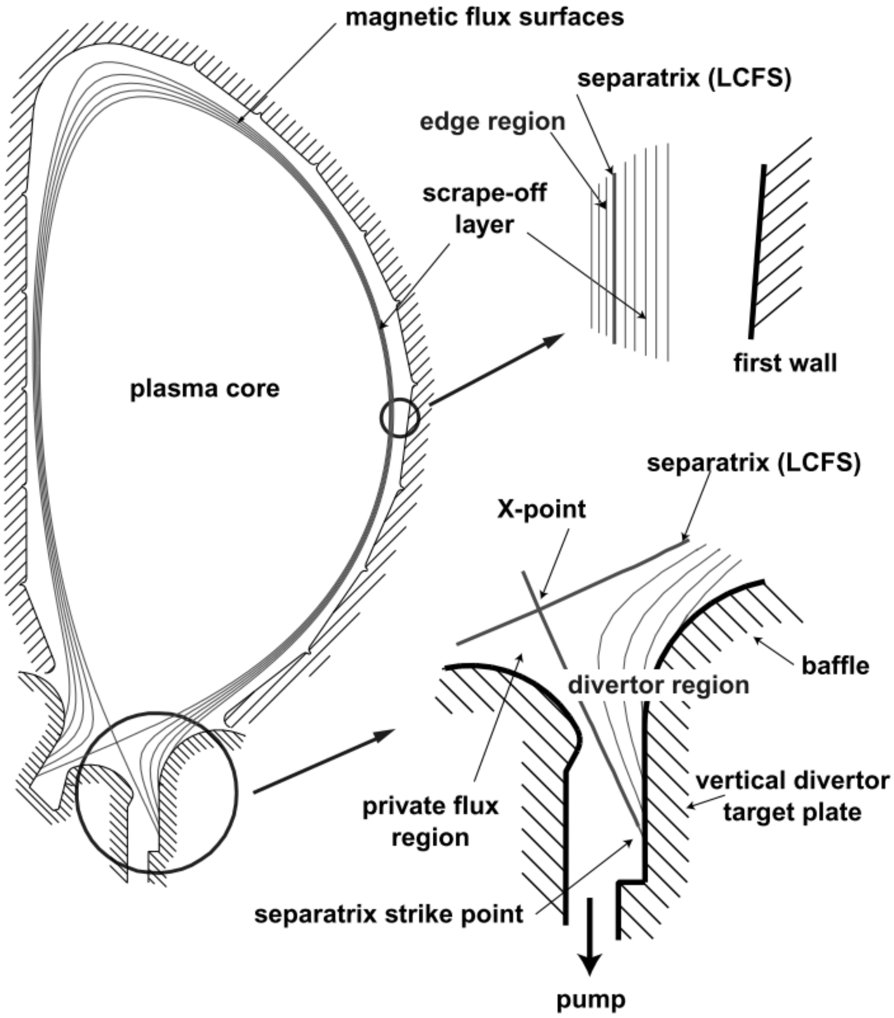

Figure 2. Poloidal 2-D cross-section of a tokamak plasma in single null configuration which emphasizes the divertor region [2]. The plasma intercepts the divertor target plates, resulting in a plasma material interaction.

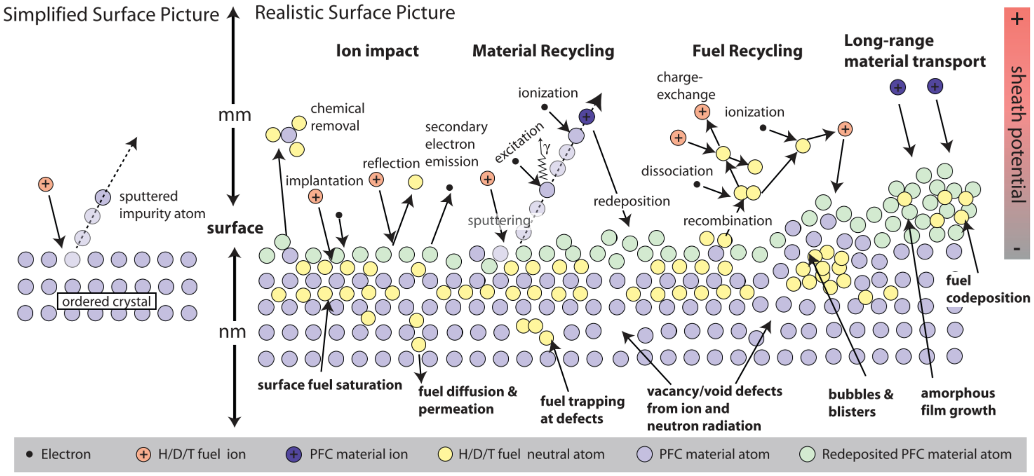

Figure 3. Schematic illustration of the complex surface interactions that occur at the material surface of a fusion plasma environment [69].

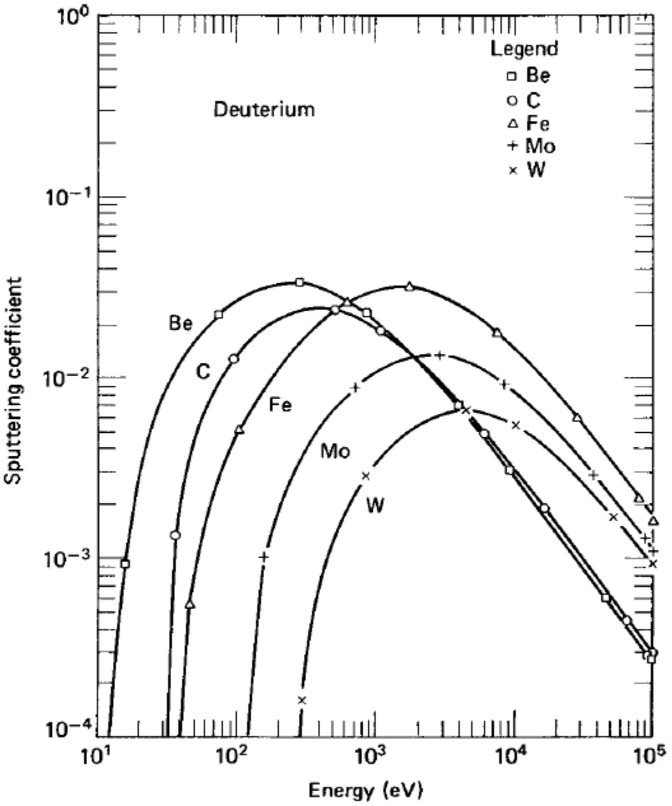

Figure 4. Physical sputtering coefficient for various materials under deuteron bombardment [70].

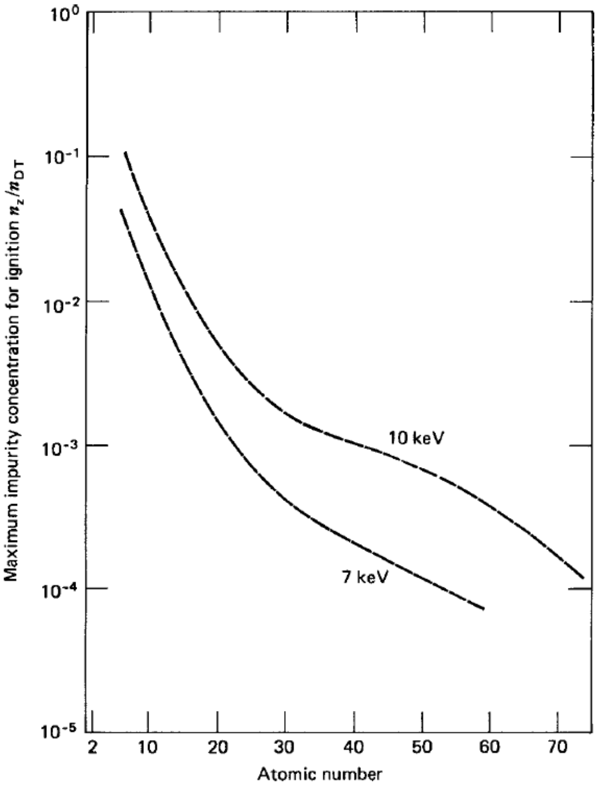

Figure 5. Maximum impurity concentration for which ignition can be achieved [70].

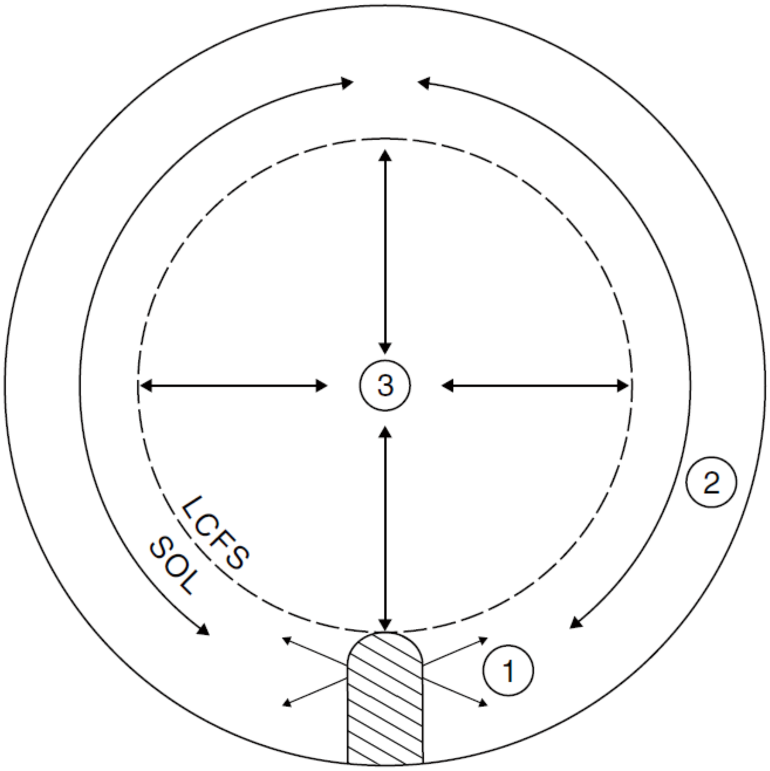

Figure 6. The three principal links in the impurity chain with a limiting surface source: (1) the source, (2) edge transport, (3) transport in the main plasma [3].

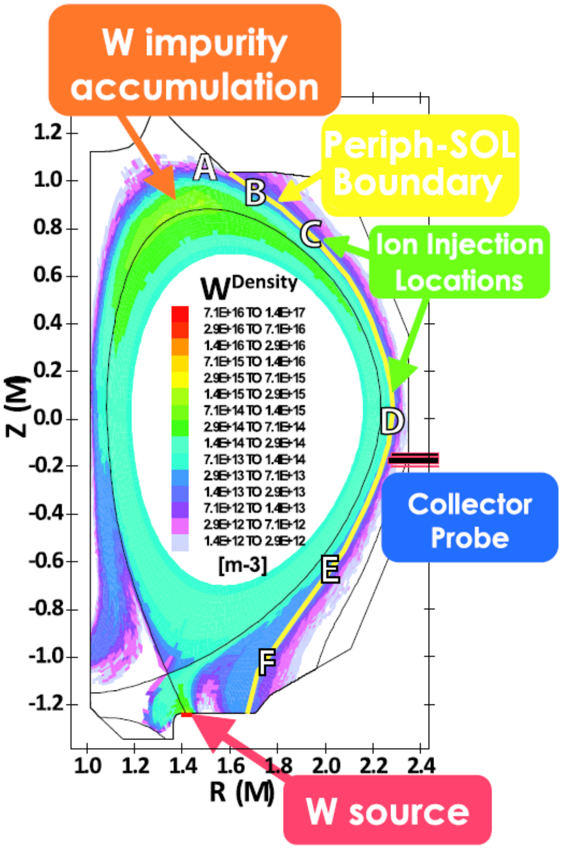

Figure 7. OEDGE simulation mesh with typical total tungsten density contours shown. Ion injection locations (labeled A-F) on the peripheral-SOL boundary are used in the ion injection simulations. Simulation depicts an increased density of tungsten at the crown.

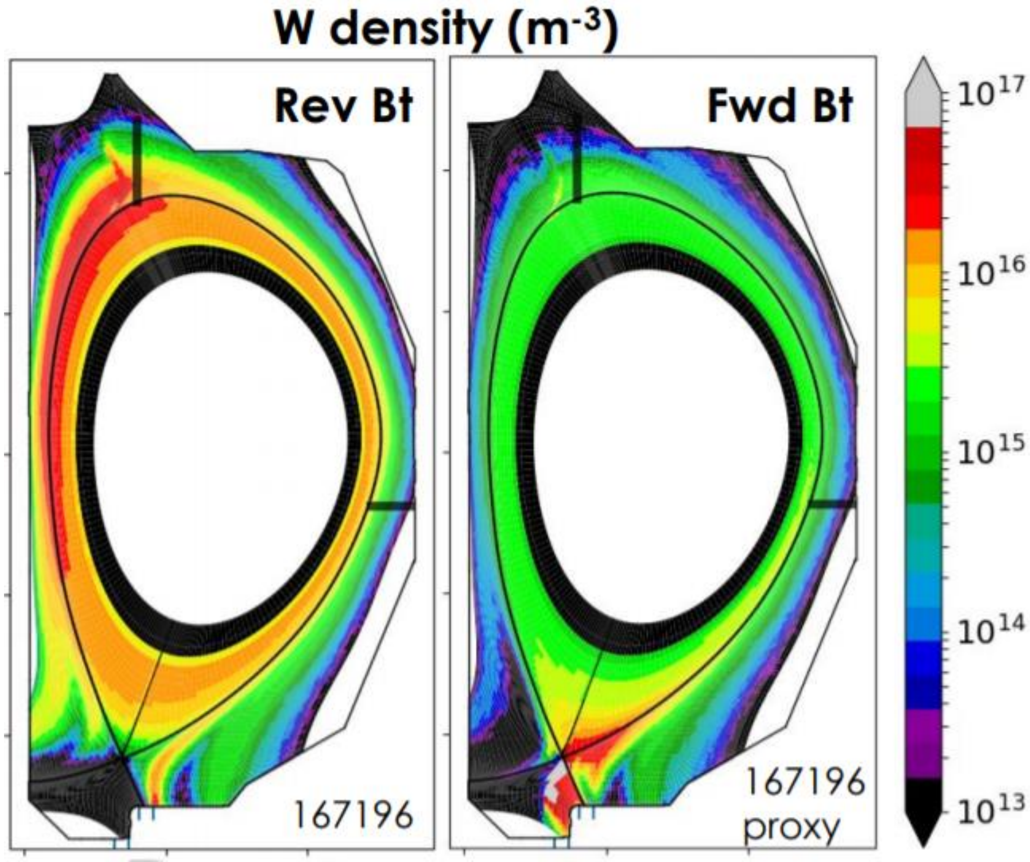

Figure 8. Tungsten density modeling in DIVIMP depicting the drift dependence on the direction of the B_T and its effect on the poloidal position of the theorized impurity accumulation region. Color bar units are atoms per cubic meter.

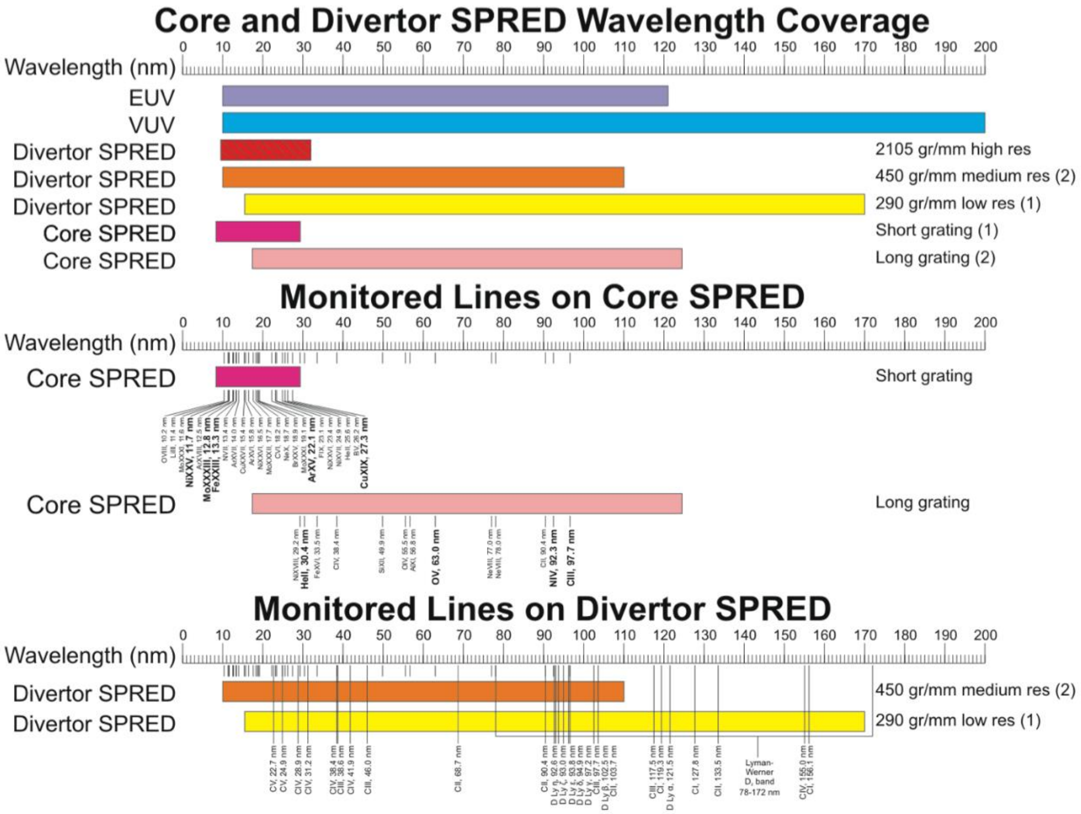

Figure 9. SPRED wavelength coverage in various regions of DIII-D dependent on grating [71]

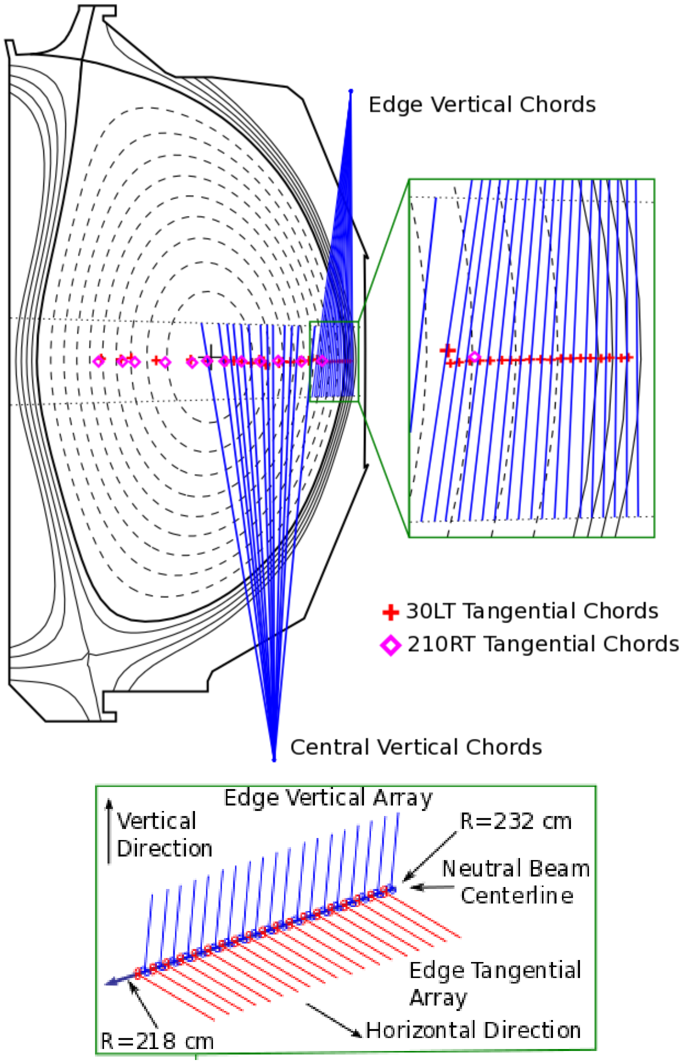

Figure 10. CER view chord geometry within DIII-D

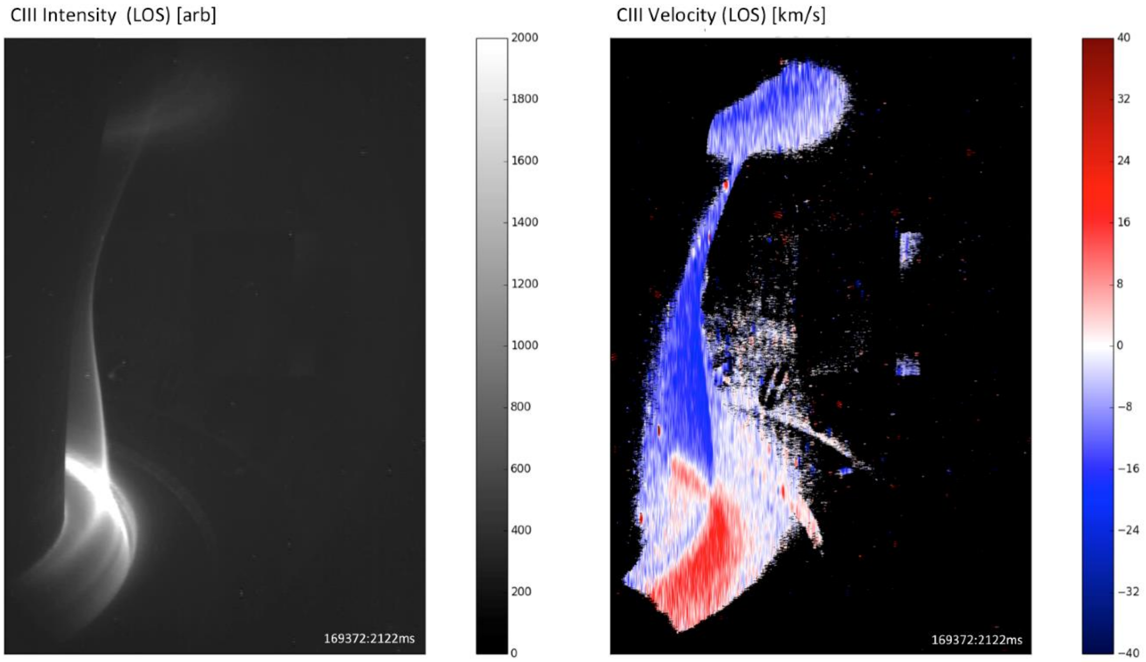

Figure 11. CIII measurements using DIII-D's CIS periscope view

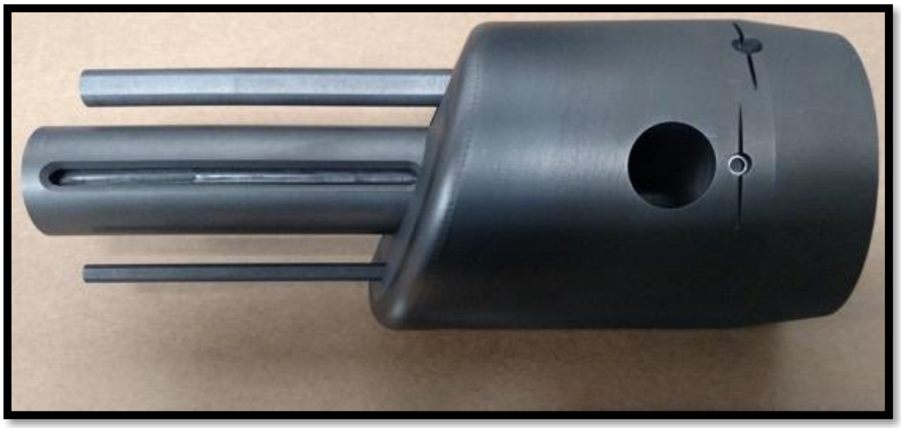

Figure 12. Triplet set of graphite collector probes inserted with MiMES for MRC 1

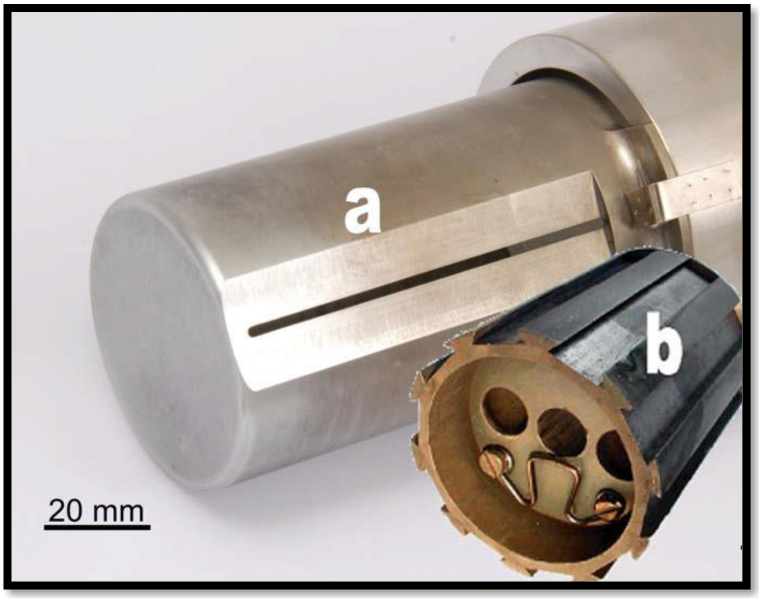

Figure 13. The molybdenum housing marked a, showing one of the two 4 mm wide and 60 mm long slits that are in the ion and electron facing directions. The rotatable sample holder normally located inside the housing is marked b [72].

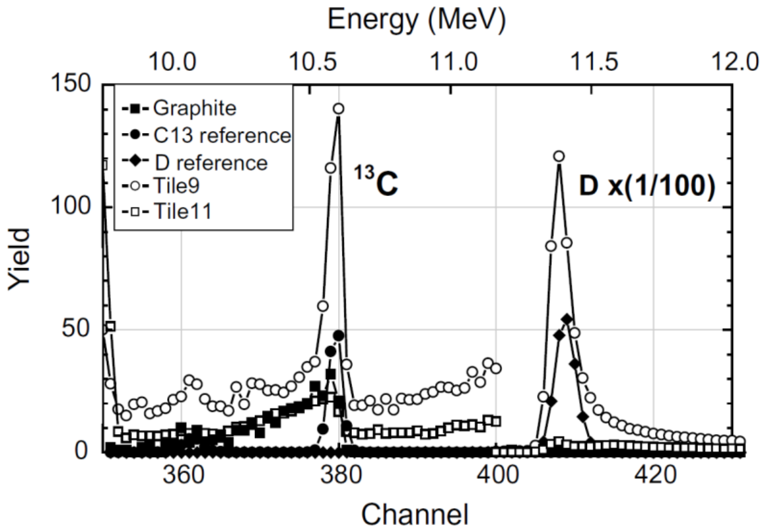

Figure 14. Energy spectra of protons from the ^{13}C (^{3}He, p) ^{15}N nuclear reaction for a graphite sample, a thin film ^{13}C reference sample, a thin film deuterium reference, and two of the tiles from DIII-D [20].

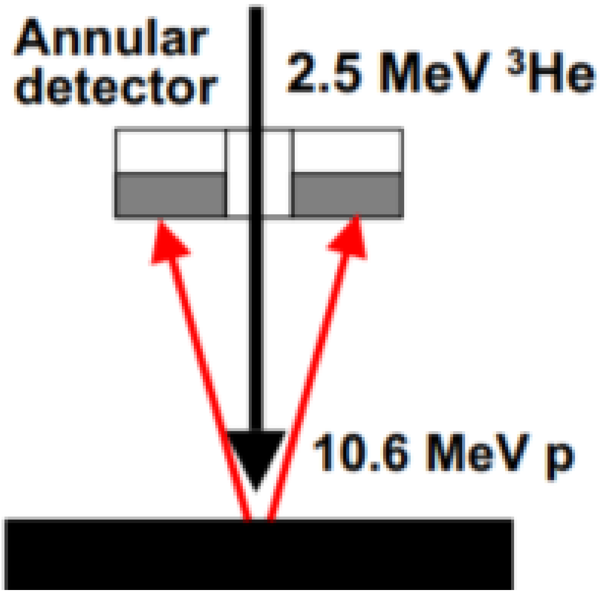

Figure 15. Optimized detector configuration for ^{13}C (^{3}He, p) ^{15}N NRA.

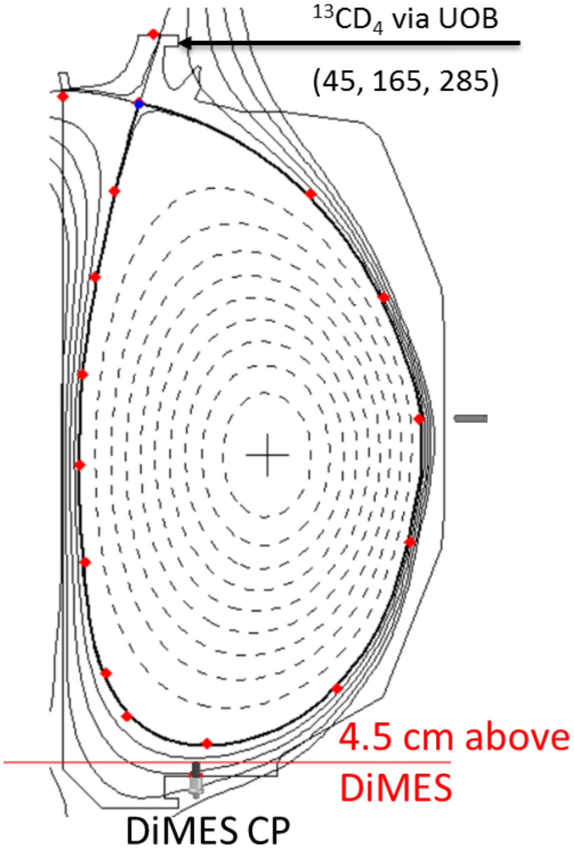

Figure 16. DIII-D shot 178346 depicting an elongated upper single null plasma with outer strike point located near the UOB gas puffing vessel entrance. Proposed MiMES and DiMES collector probes are also shown

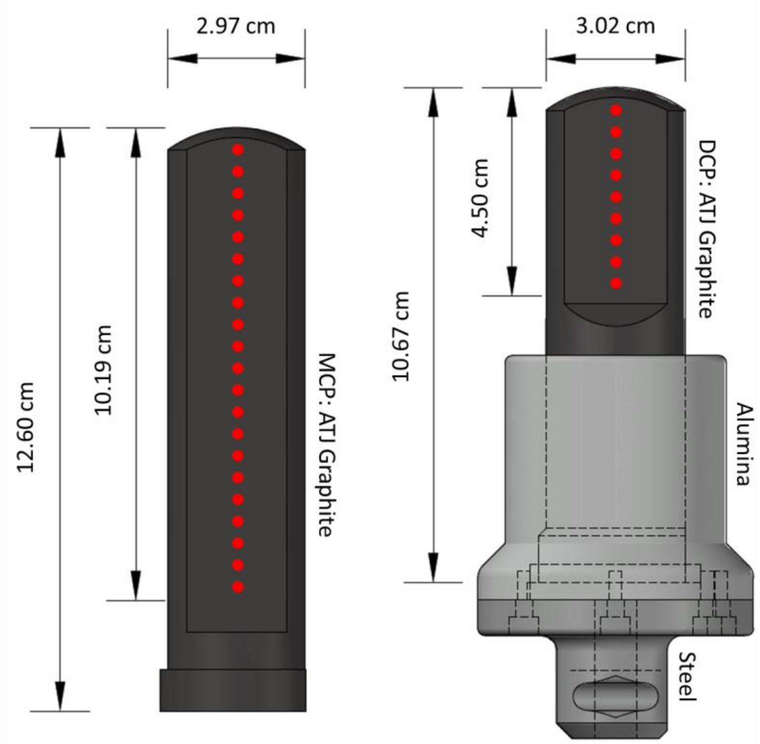

Figure 17. Renderings of MCP and DCP assemblies are shown on the left and right. Length and width of each collector probe is marked in centimeters. The smaller of the two length measurements on each probe face marks the length which is exposed during experiments. Red dotted lines mark where deposition from plasma exposure is characterized.

Figure 18. Collection plate insert design for hybrid probe housing

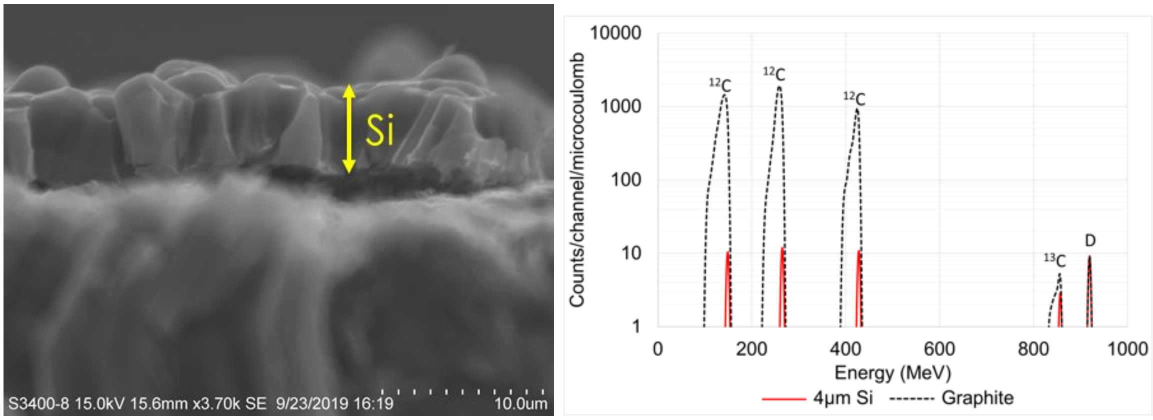

Figure 19. Silicon layer of ~5 μm grown by e-beam deposition and the effect on NRA analysis shown in SIMNRA simulations.

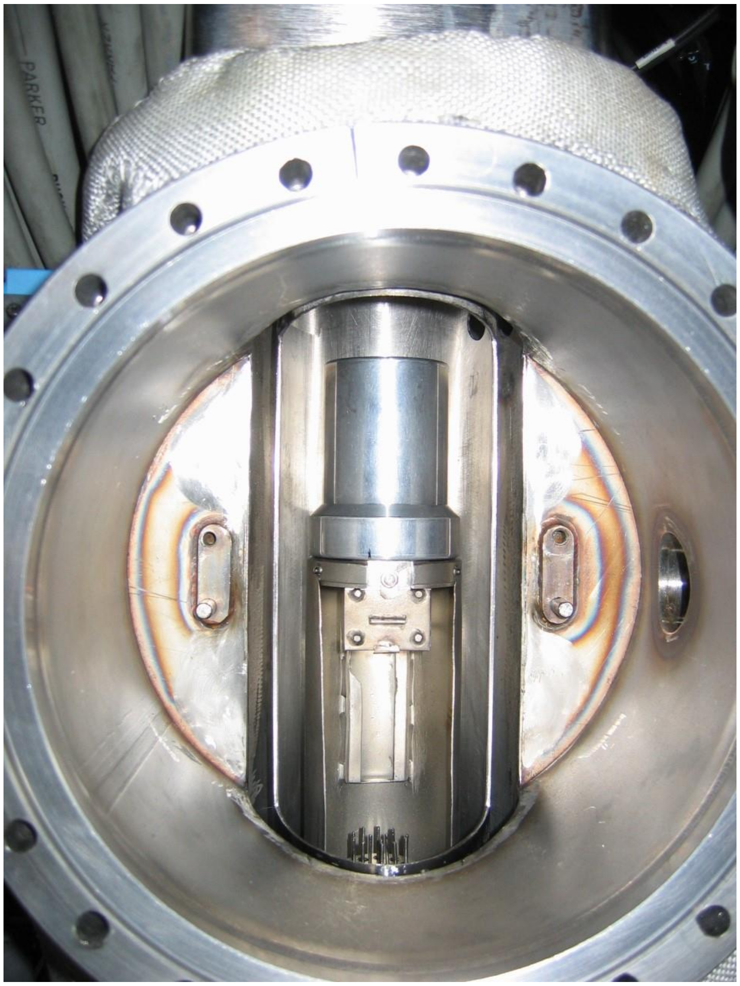

Figure 20. DiMES chamber at DIII-D.

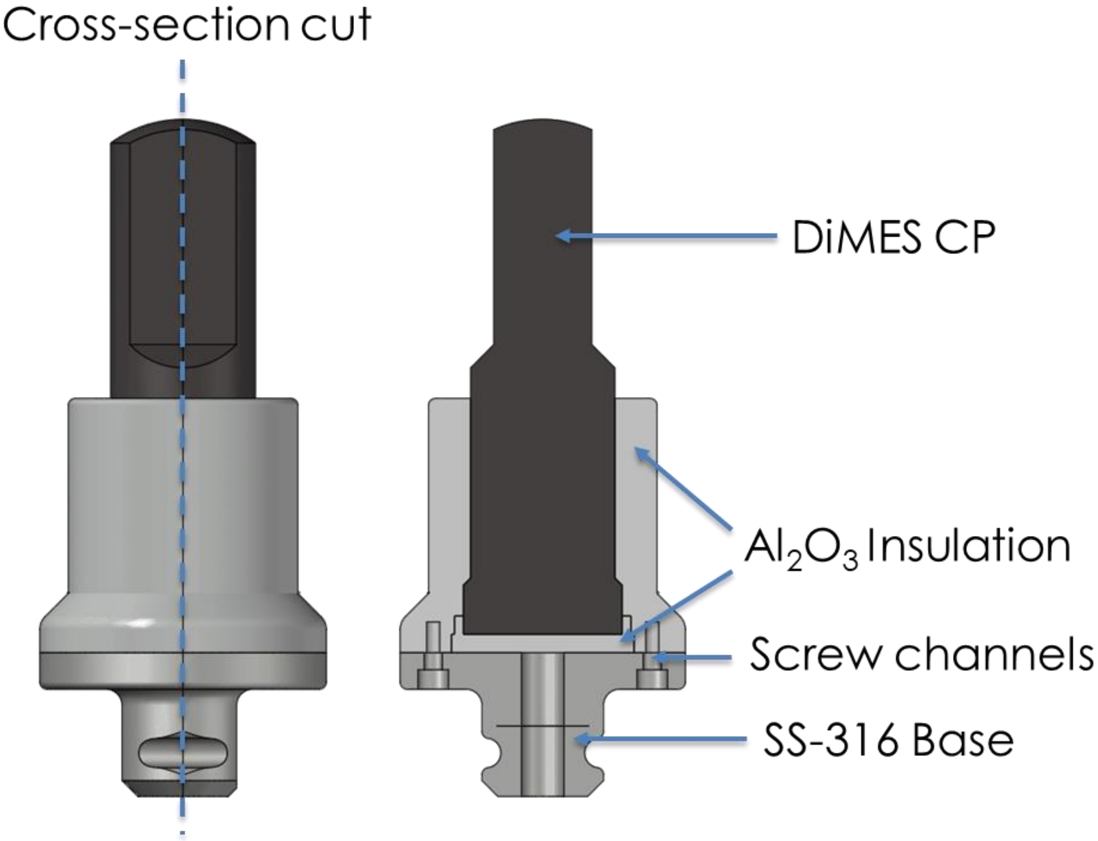

Figure 21. DiMES Collector probe assembly

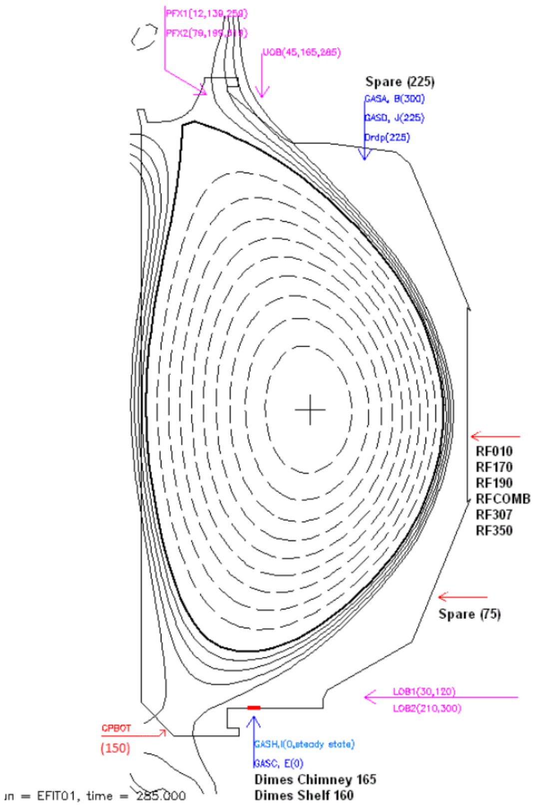

Figure 22. Poloidal gas injection locations around the DIII-D vessel with toroidal locations in parentheses

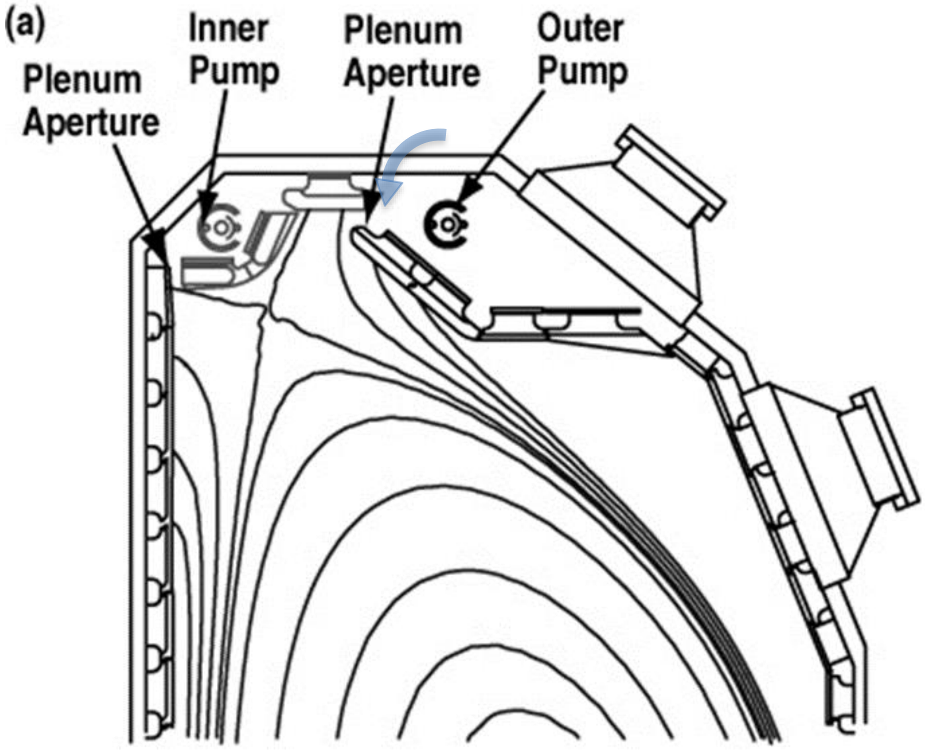

Figure 23. Schematic of inner and outer pumps and plenums on DIII-D's upper divertor

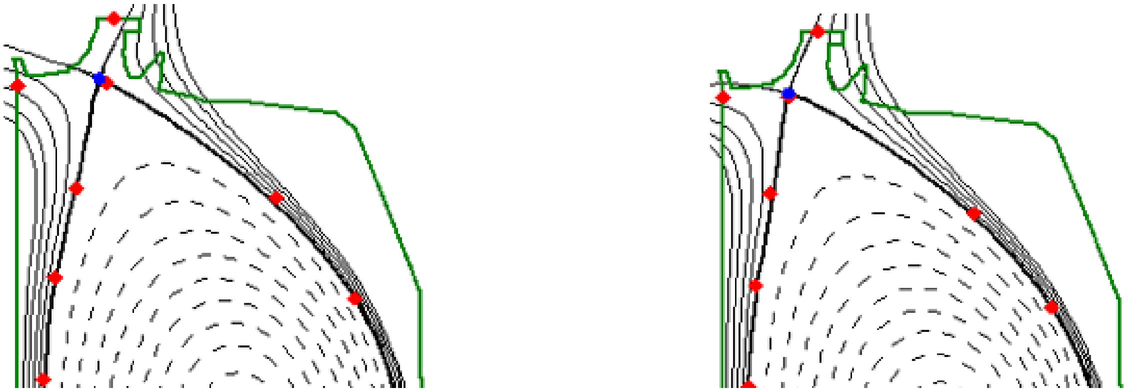

Figure 24. EFIT reconstruction for shot 171553 showing two strike point sweep positions at 2500 and 4000 ms. The shape control points in red and blue can be modified to decrease the gap distance between the plasma crown and the lower divertor. DiMES position is noted as a red stripe in the lower divertor.

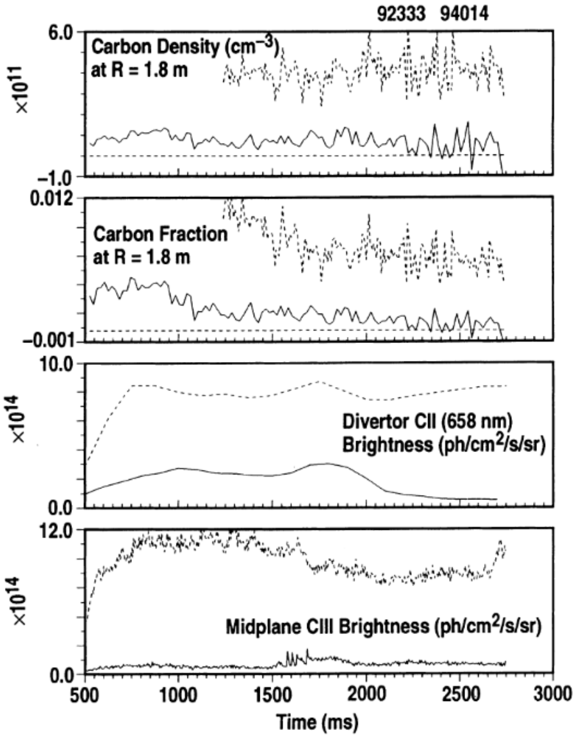

Figure 25. Carbon spectroscopic time traces for two L-Mode discharges with deuterium and helium fueling respectively.

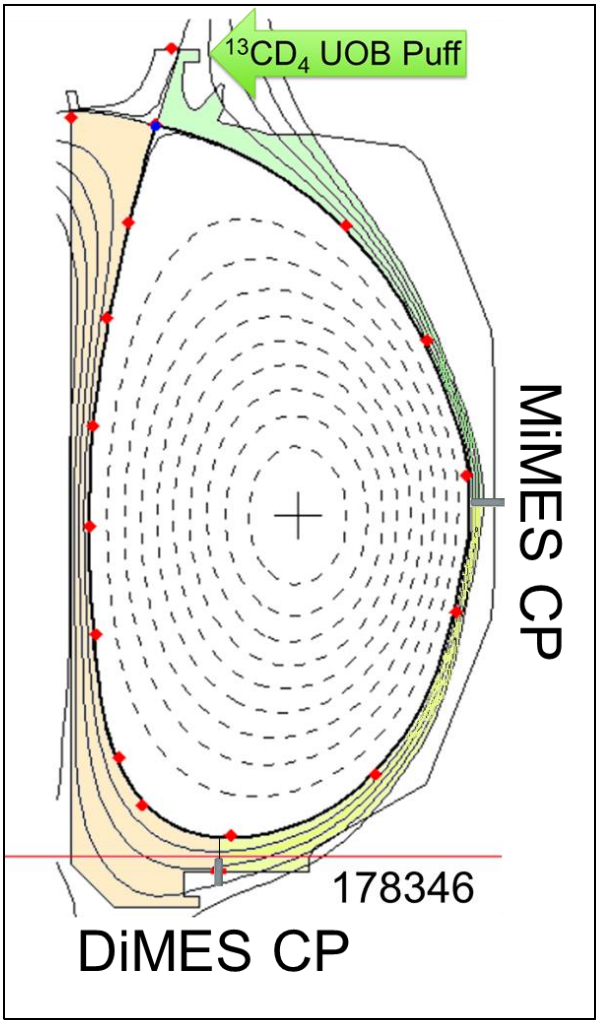

Figure 26. Three potential impurity accumulation regions due to $^{13}CD_4$ puff at UOB. Each region represents a change in ITF/OTF content ratio on the CP faces. The outer target is at the location of the plasma leg that will receive a 13CD4 UOB puff.

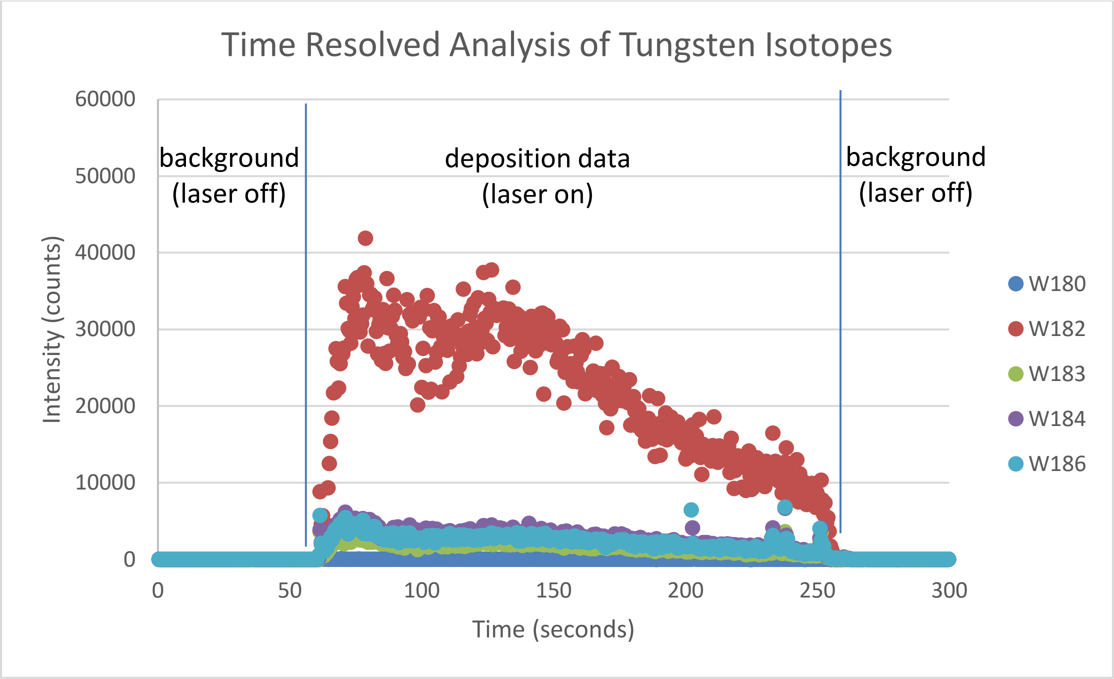

Figure 27. Representative time resolved analysis centerline scan of collector probe AD33 used in the first metal rings campaign.

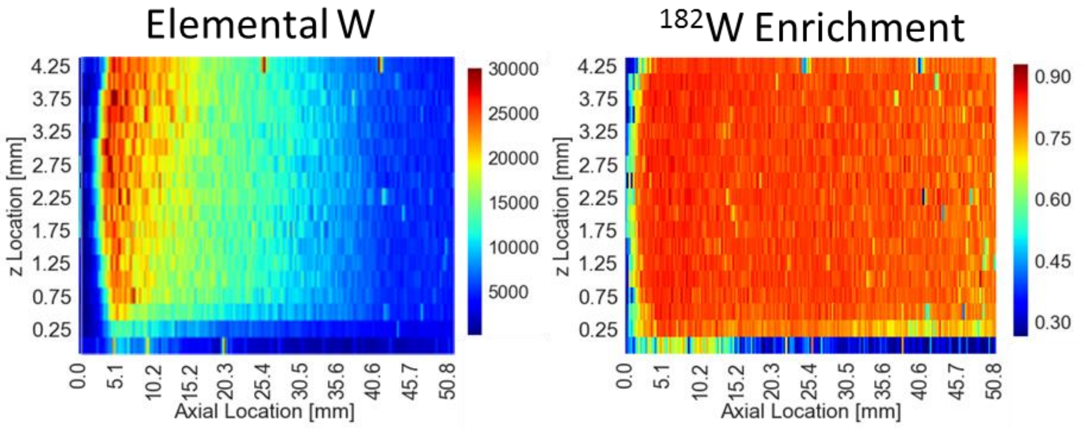

Figure 28. 2-D surface characterization of total tungsten content (left) and the isotopic ^{182}W enrichment fraction (right) across a typical 3 cm probe insert used in MRC 1.

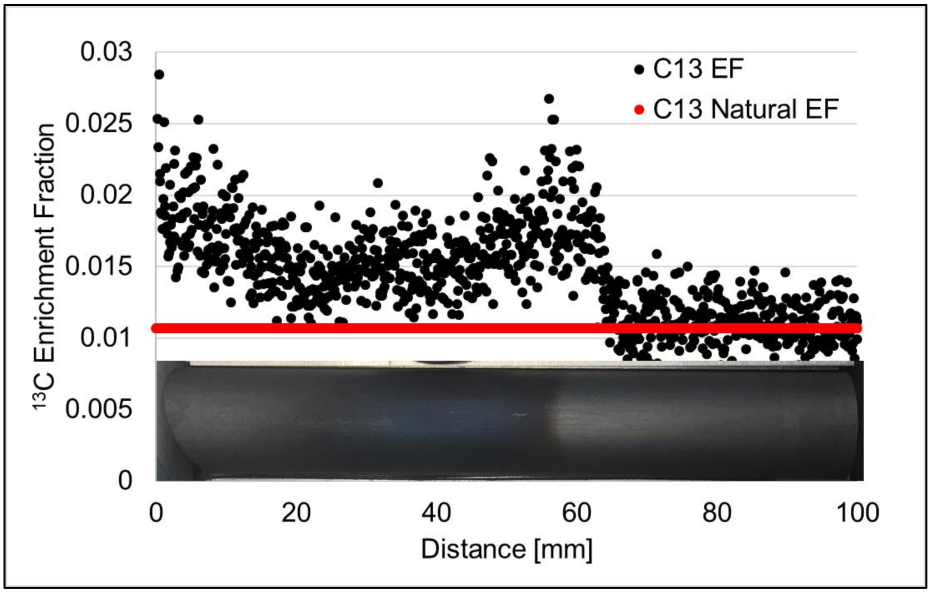

Figure 29. ^{13}C enrichment fraction measurements in black compared to the natural abundance value in red.

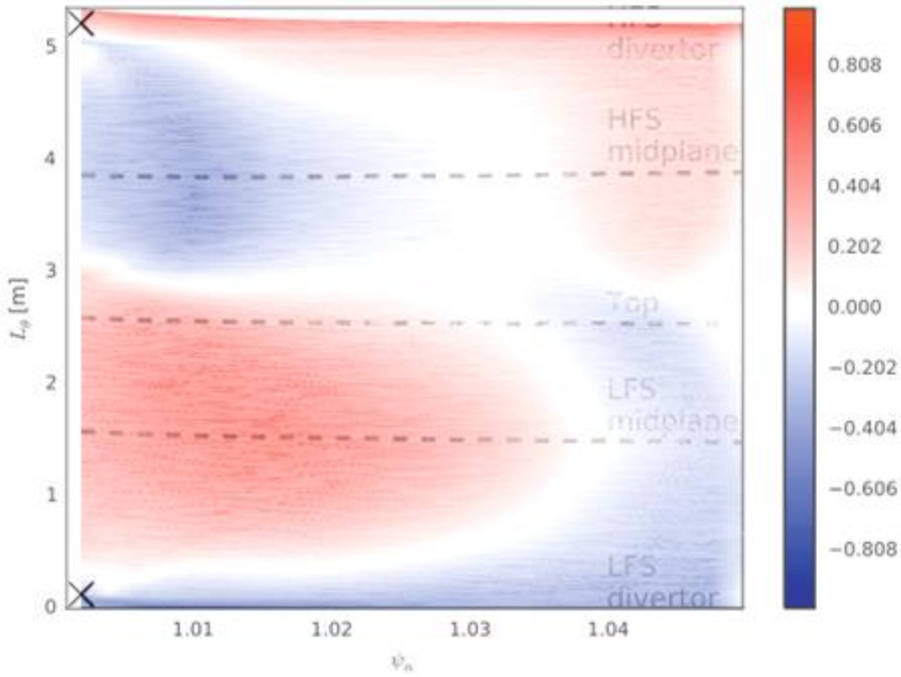

Figure 30. Contour plot of parallel Mach number in the SOL from XGCa simulations. Red indicated flow towards the high-field side divertor, and blue indicates flow towards the low-field side divertor. White is indicative of a stagnation in the flow with zero velocity.

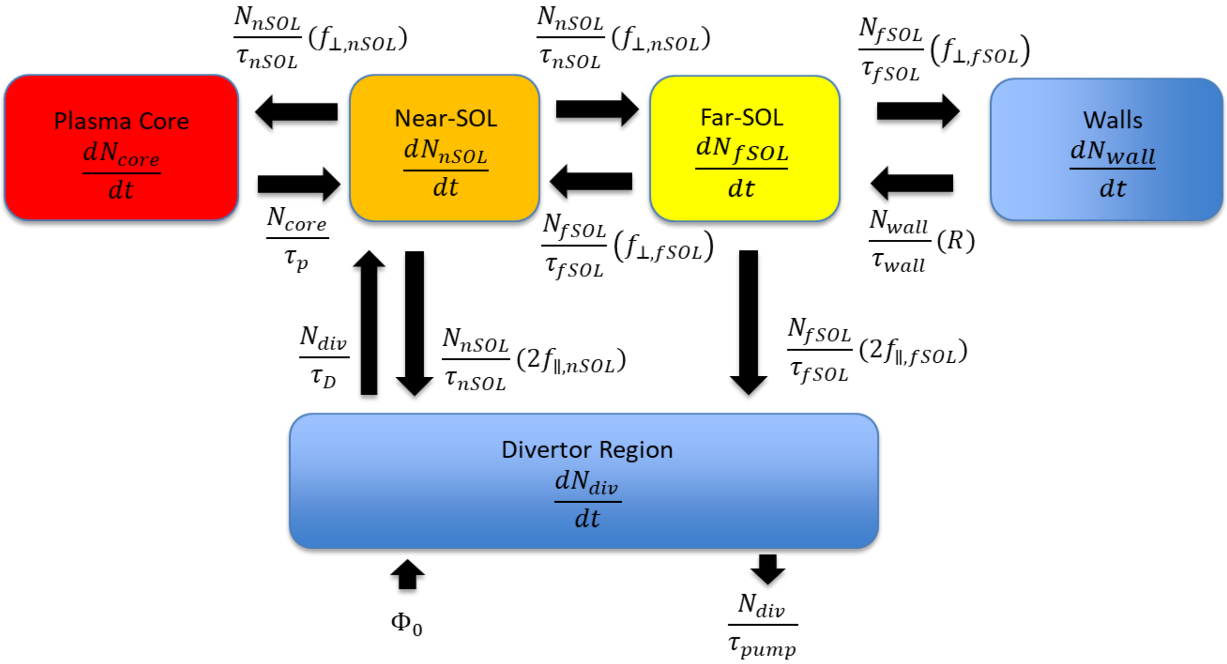

Figure 31. Schematic of the non-recycling multi-reservoir model

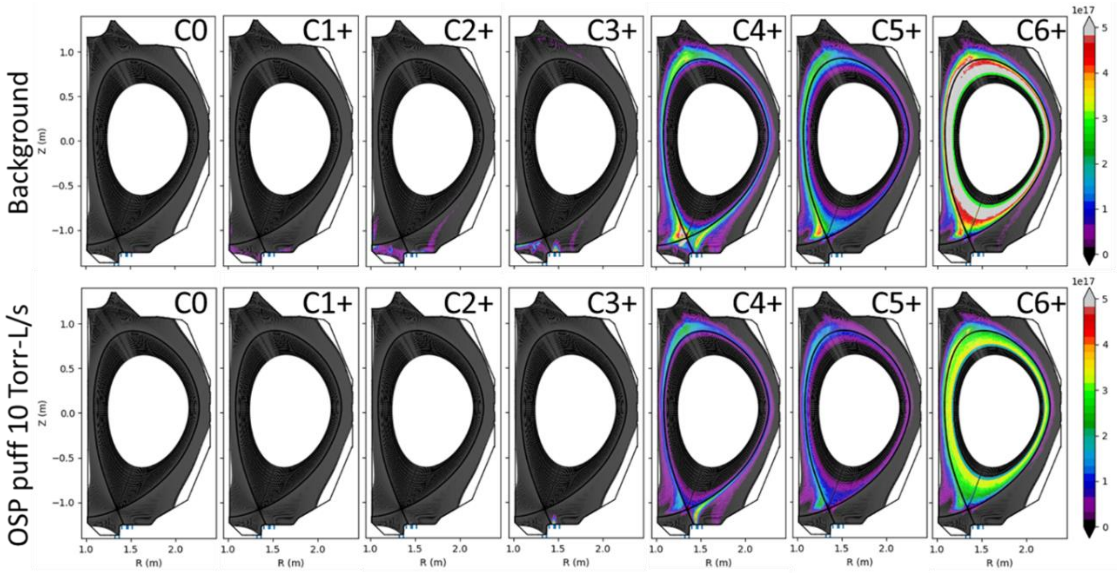

Figure 32. DIVIMP simulation of each carbon charge state throughout a DIII-D plasma. Conditions include a lower single null 3 MW L-mode plasma from MRC in Reverse B_T with ~3.5e20 at/sec or 10 Torr-L/sec of $^{13}CD_4$ puffing.

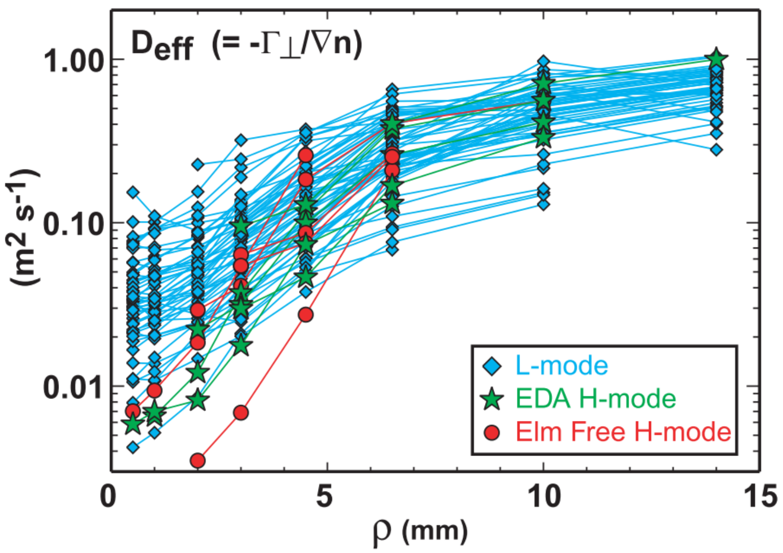

Figure 33. Effective cross-field particle diffusivity profiles for a range of plasma discharges on Alcator C-MOD showing the variance between the near and far-SOL with a boundary at $\rho = 5$ mm [45].

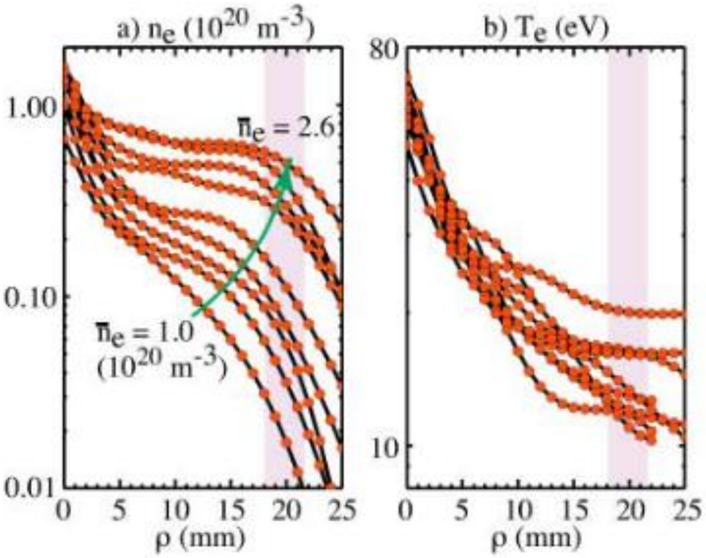

Figure 34. SOL (a) density profiles and (b) temperature profiles versus core density. The location of the outboard limiter is indicated by the shaded stripe. Note the change in density slope occurs at $\rho = 5\ mm$.

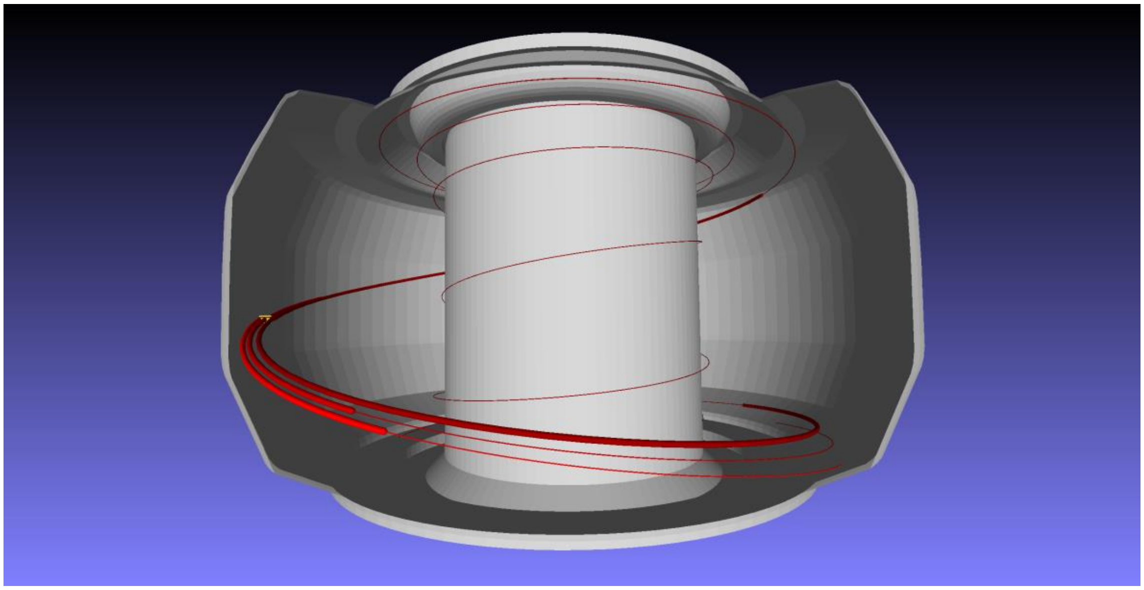

Figure 35. Visual representation of the connection length for a graphite collector probe (yellow) that is place at the outboard midplane of DIII-D. The red lines are at various distances from the separatrix, and each has a unique connection length.

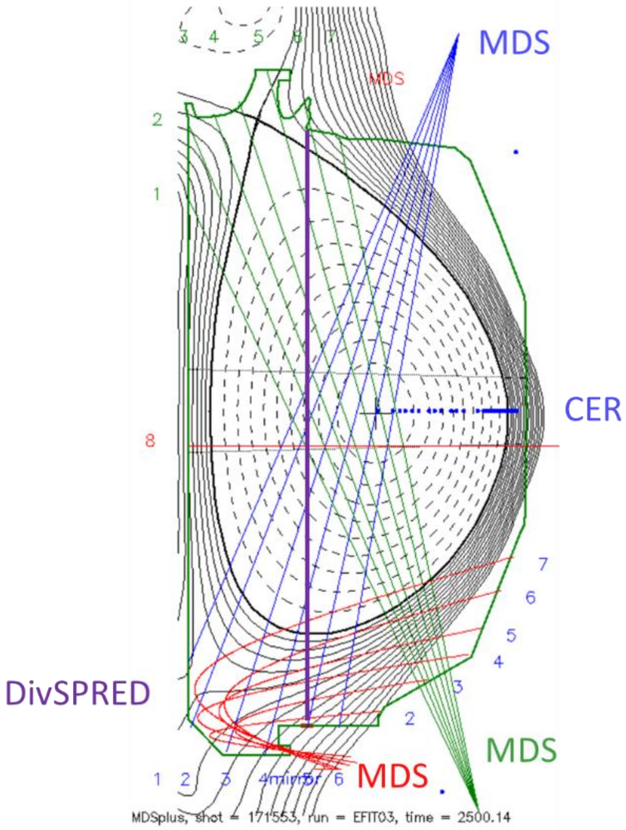

Figure 36. MDS, CER, and DivSPRED views for line integrated measurements of C4+ emission.

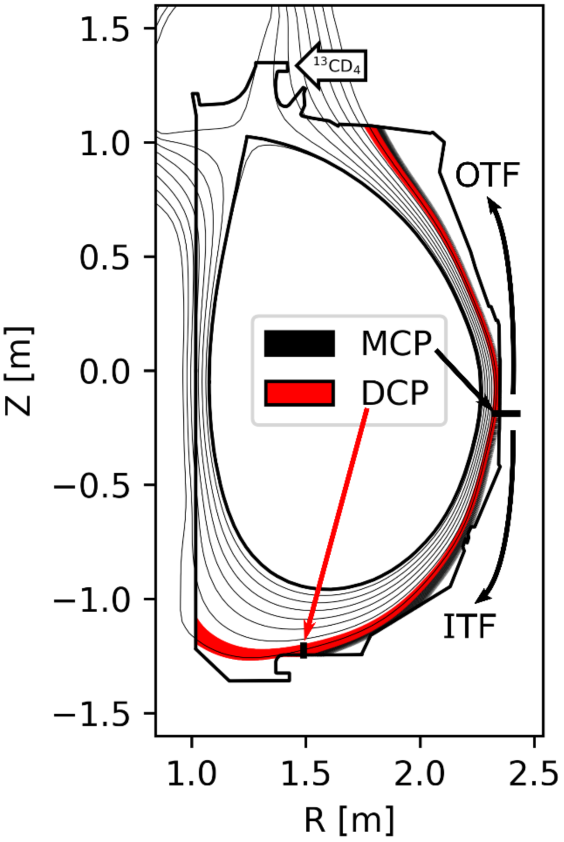

Figure 37. Poloidal cross section of DIII-D (shot # 187116) with field line trace simulations from MAFOT marked by black and red shaded flux surfaces for the MCP and DCP.

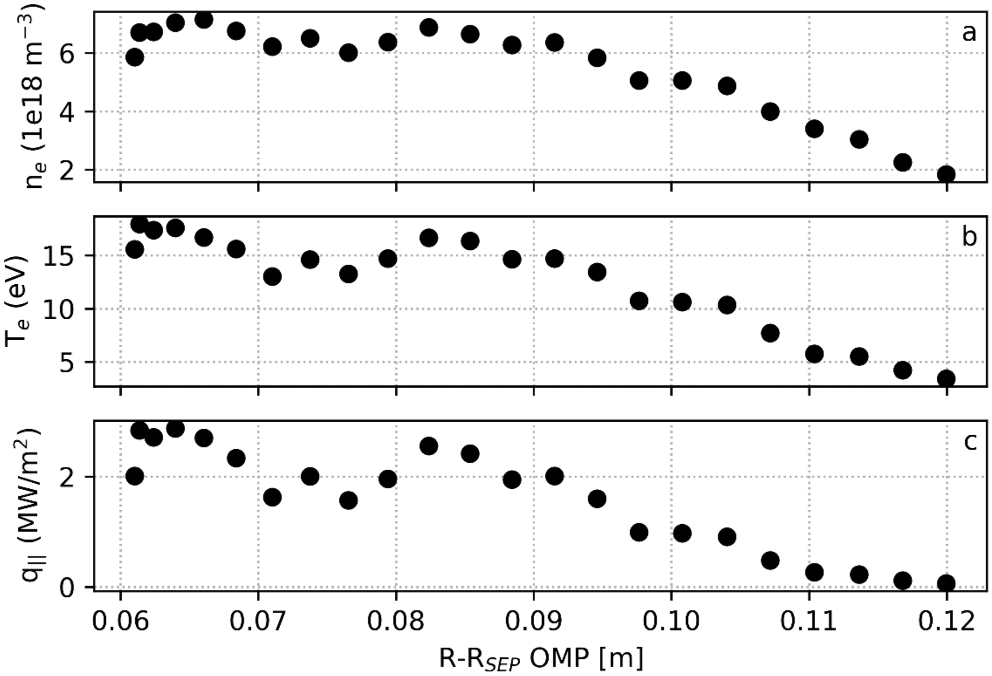

Figure 38. SOL electron temperature and density measurements from MiMES reciprocating probes during diagnostic companion shot 187106 at ~3400 ms.

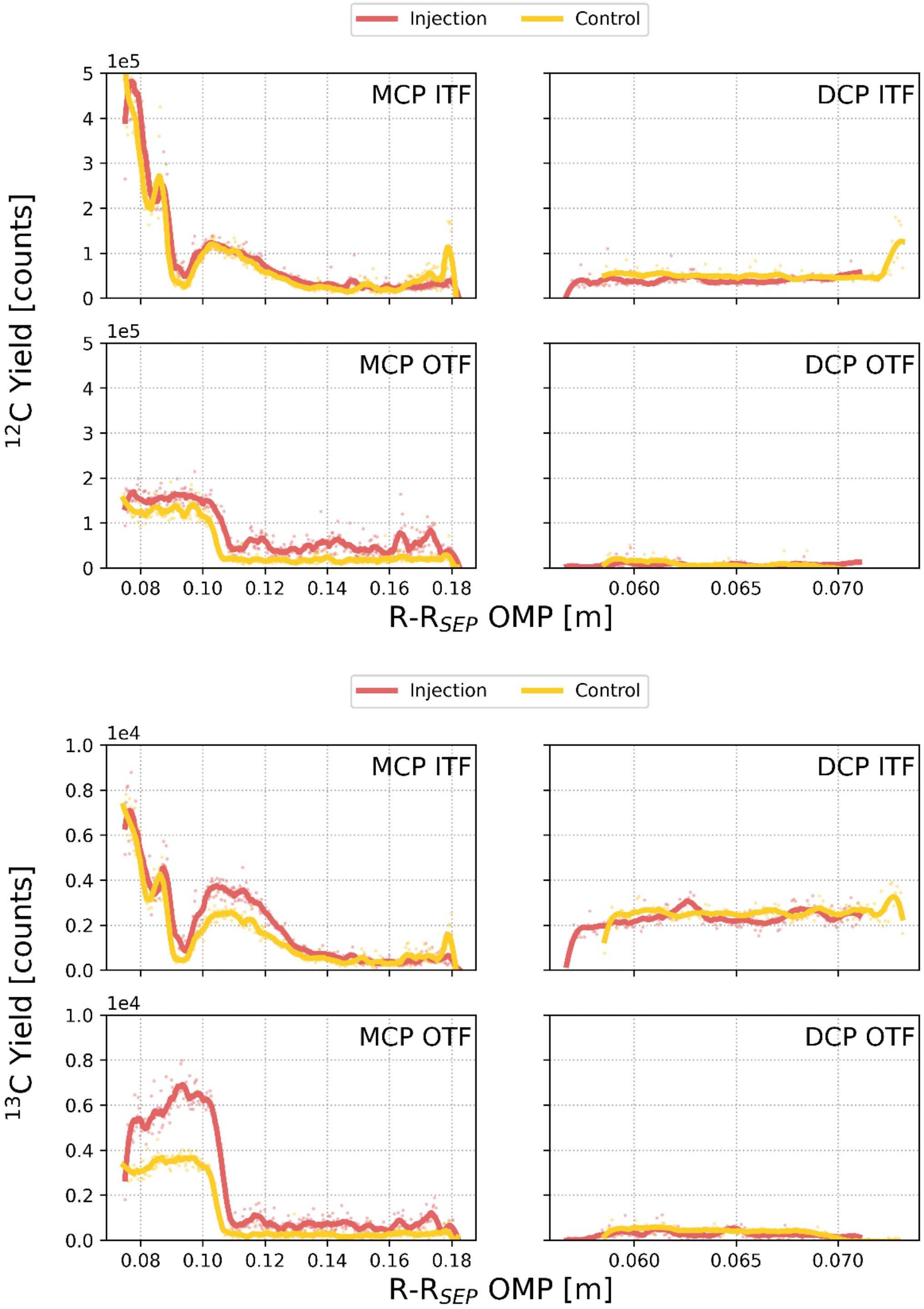

Figure 39. LA-ICP-MS measurements of ^{12}C and ^{13}C across the centerline of collector probes exposed to collection phases listed in Table 1.

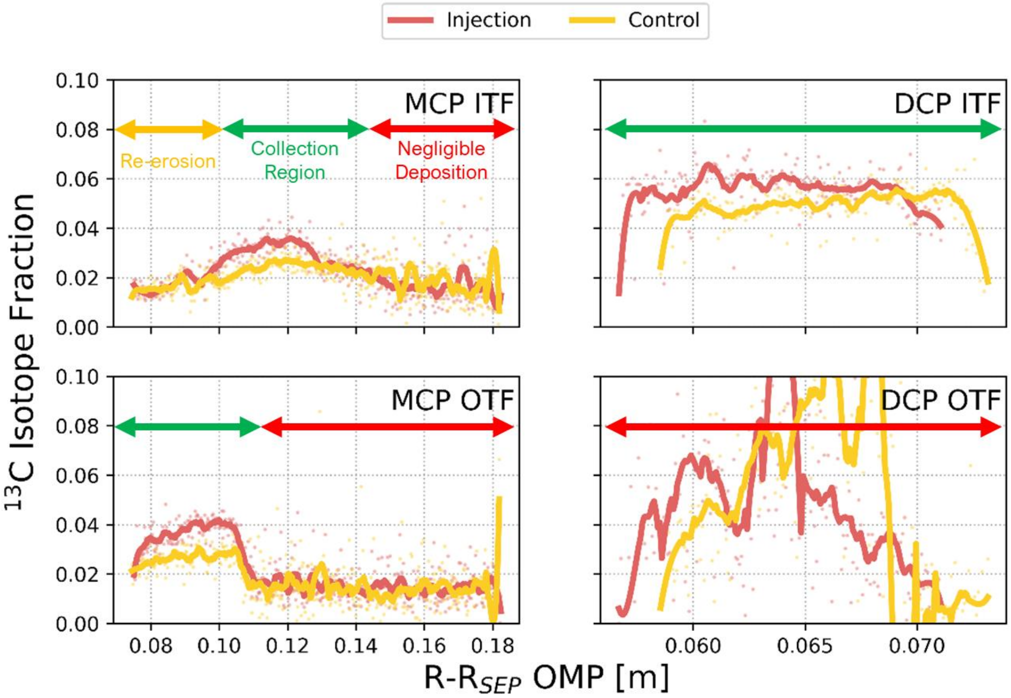

Figure 40. Isotopic fraction of ^{13}C in Figure 39 measurements for the methane injection and control sets in Table 1.

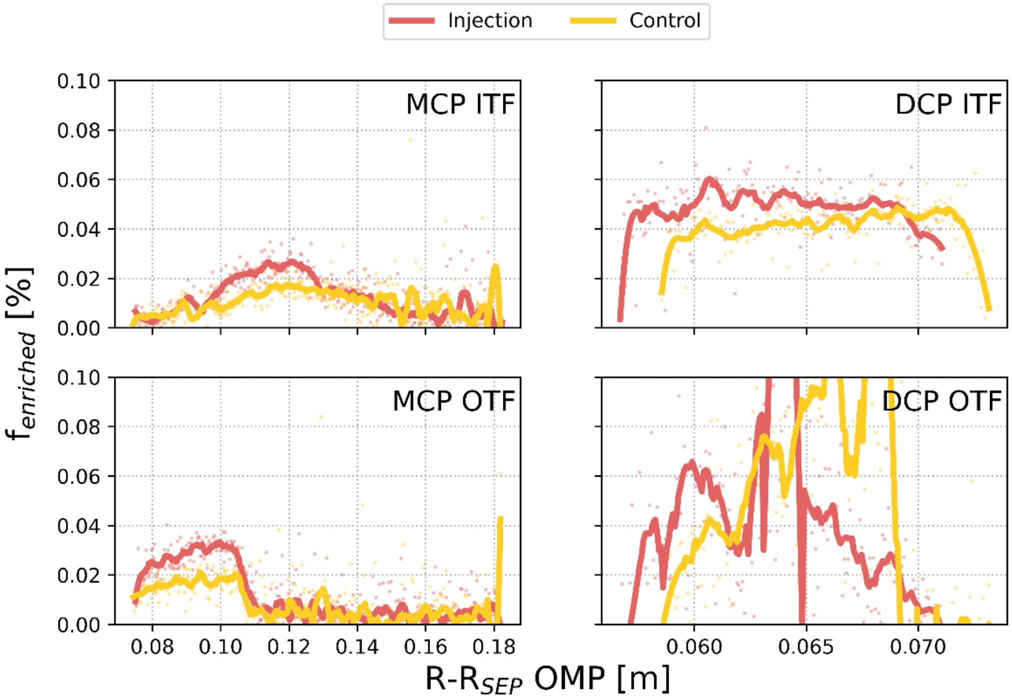

Figure 41. Fraction of enriched ^{13}C measured across the centerline of collector probes.

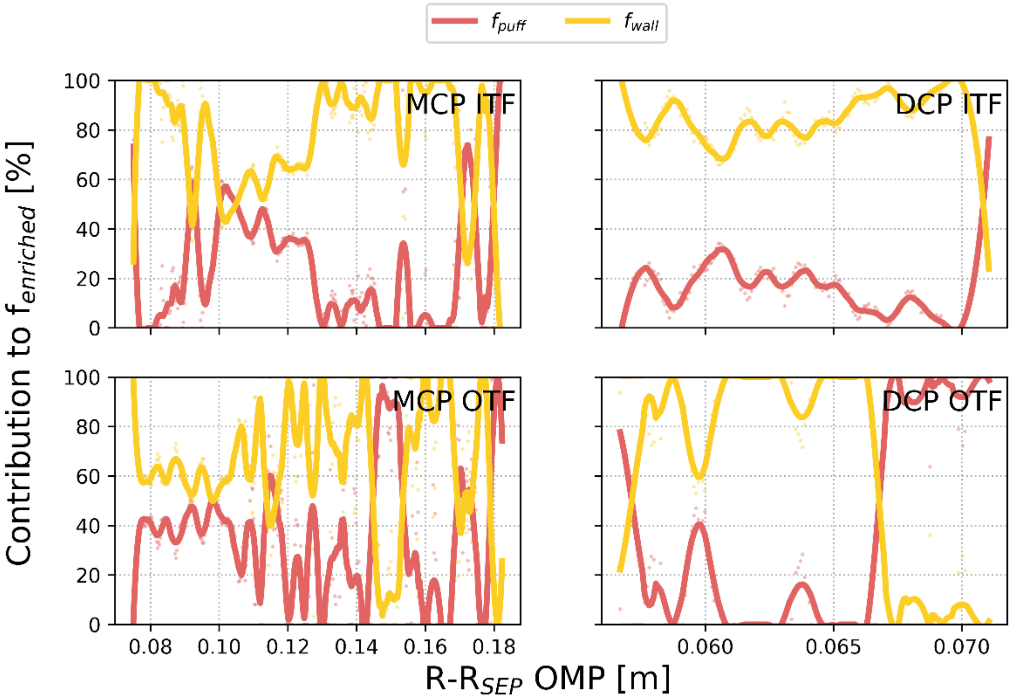

Figure 42. Injection set measurements of enriched ^{13}C contributions to $f_{enriched}$ from the $^{13}CD_4$ puff and the re-eroded wall source of enriched ^{13}C impurities.

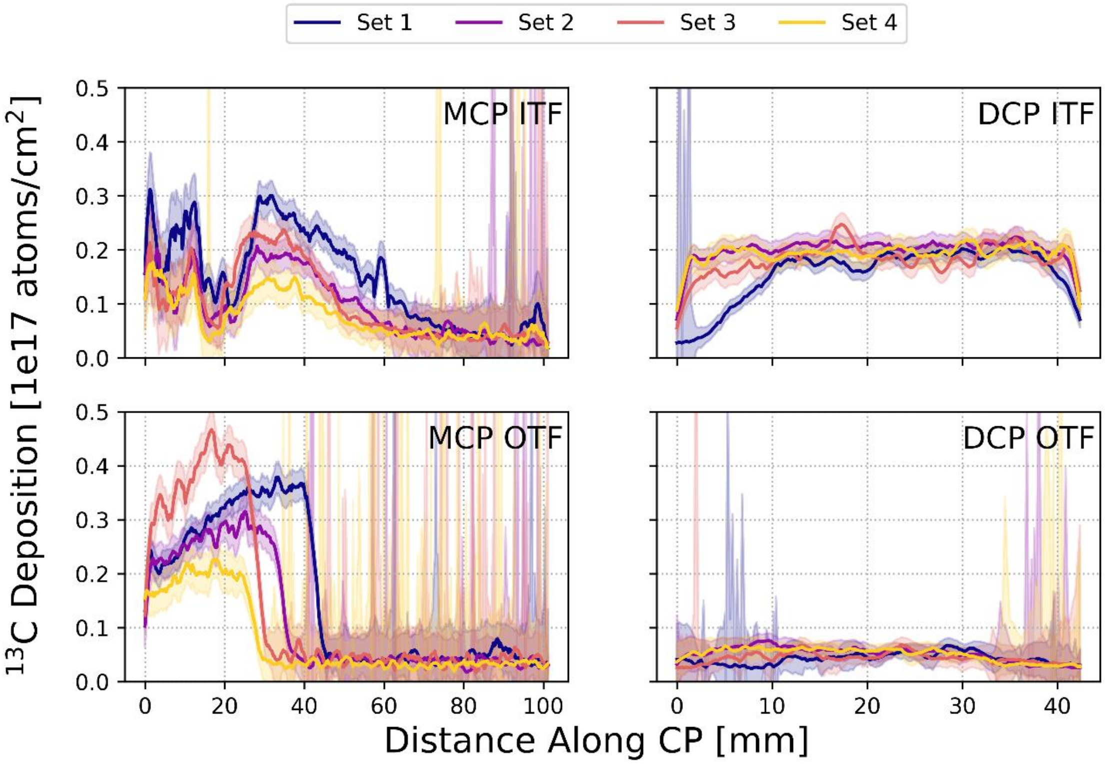

Figure 43. Table 5 collection phase results for MCP and DCP ^{13}C deposition measurements by LA-ICP-MS.

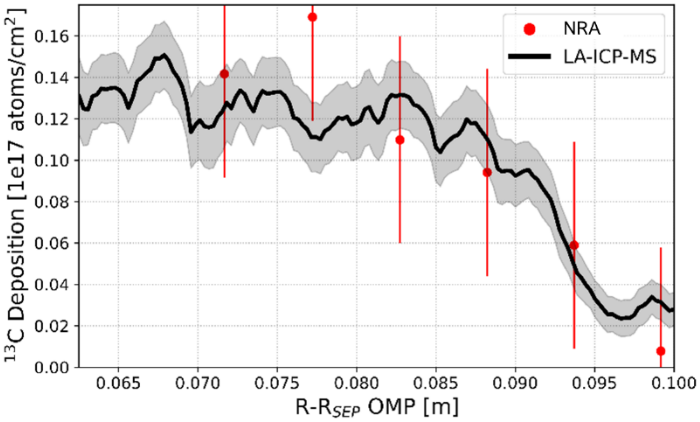

Figure 44. ^{13}C Excess measurements by NRA and LA-ICP-MS for MCP exposed to shots 184535-184536.

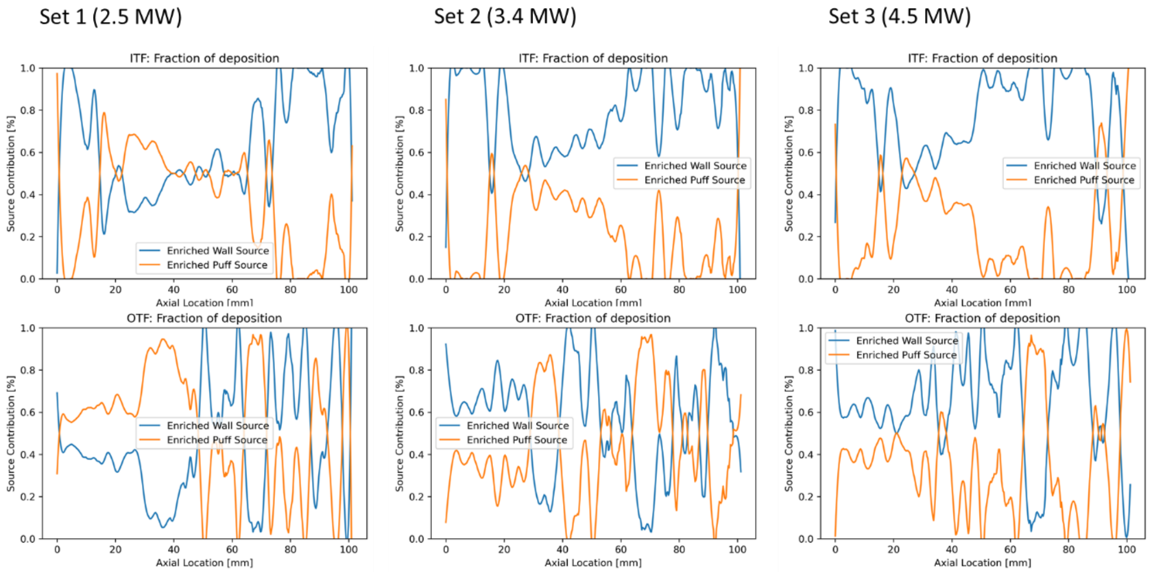

Figure 45. $f_{enriched}$ source contributions for Table 5 MCP probes.

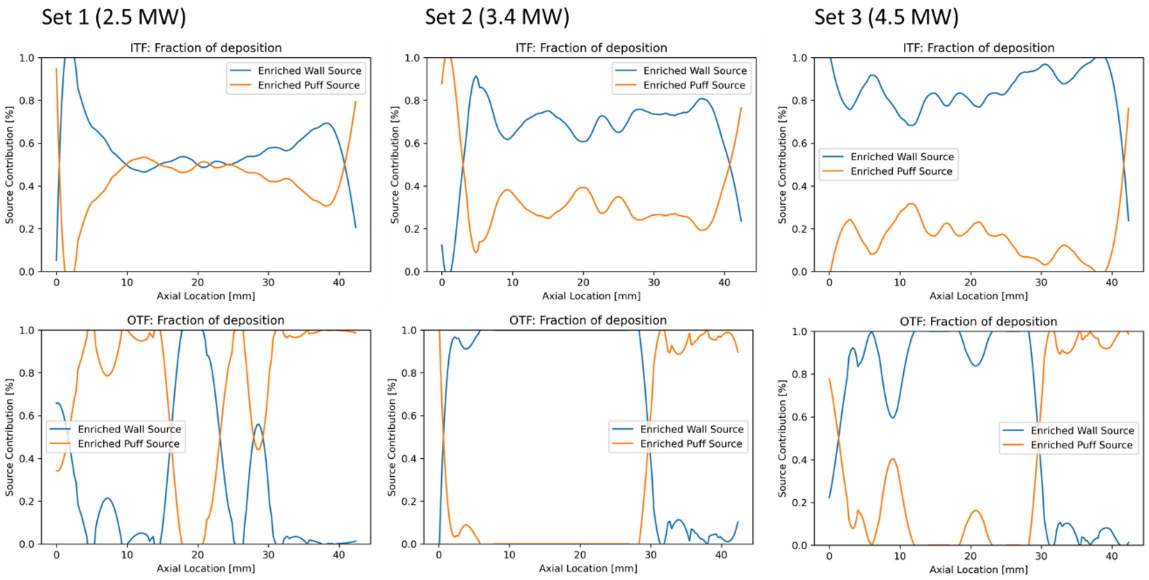

Figure 46. $f_{enriched}$ source contributions for Table 5 DCP probes.

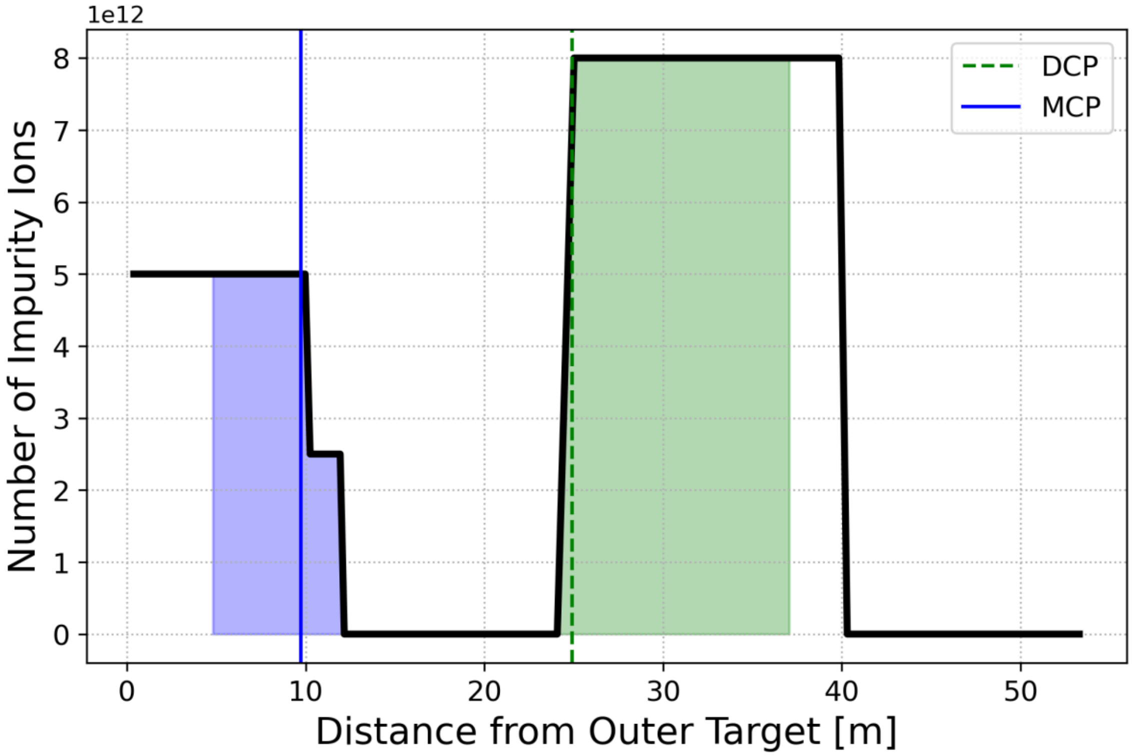

Figure 47. Expected impurity profile along a flux surface which feeds collector probes.

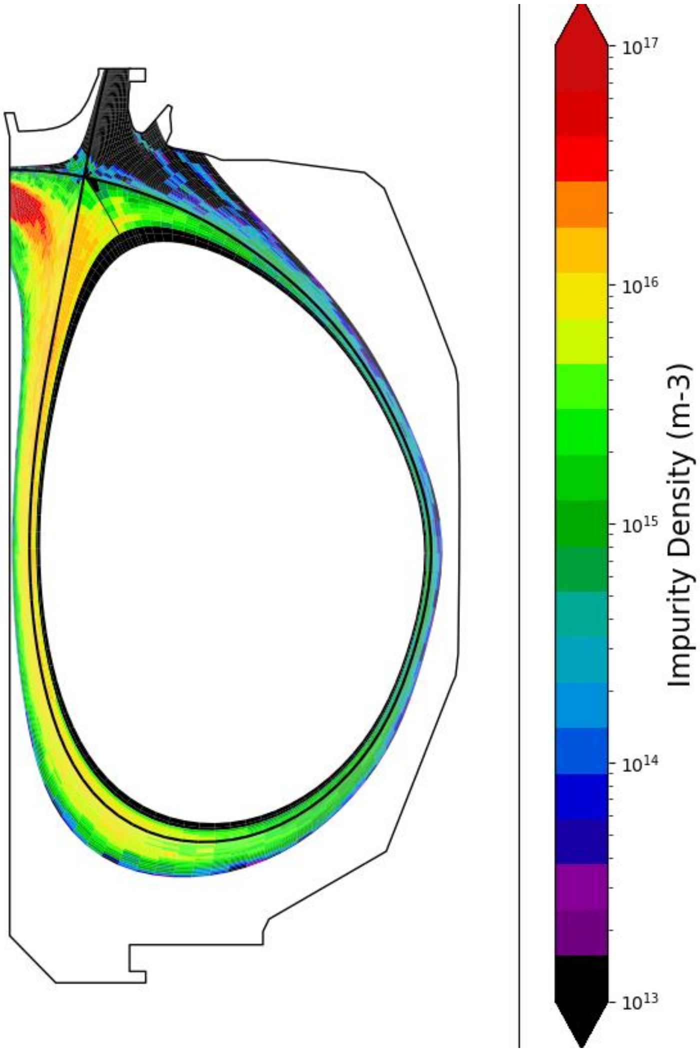

Figure 48. Inner strike point carbon impurity source simulation using DIVIMP.

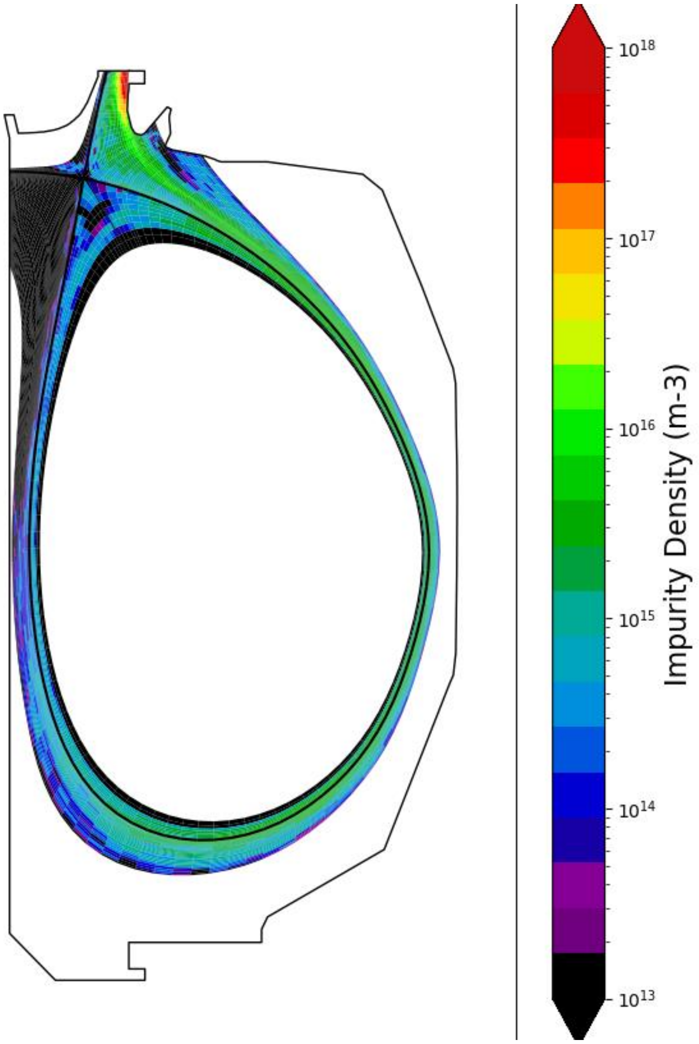

Figure 49 Outer strike point carbon impurity source simulation using DIVIMP.

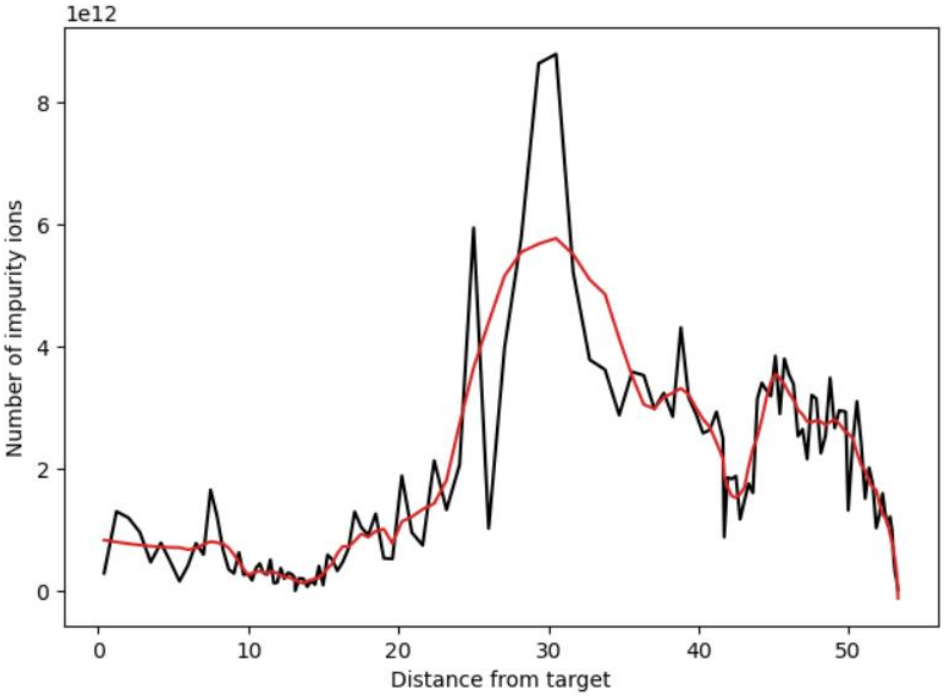

Figure 50 Inner strike point carbon impurity source simulation using DIVIMP for an outer ring. Distance from target begins at outer target and follows the simulation ring clockwise toward the inner target

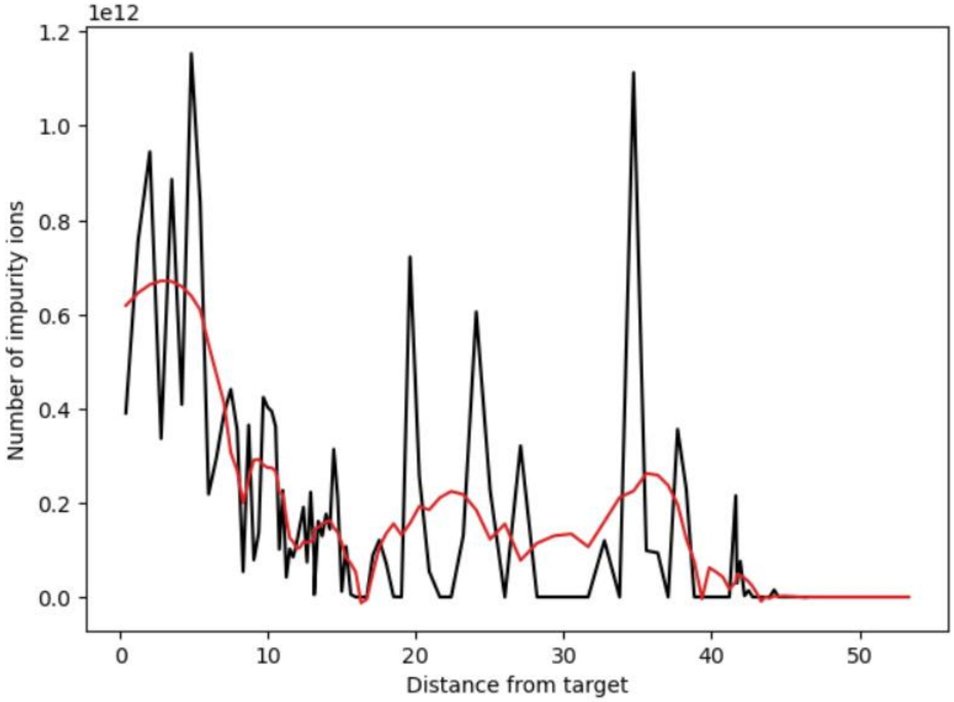

Figure 51 Outer strike point carbon impurity source simulation using DIVIMP for an outer ring. Distance from target begins at outer target and follows the simulation ring clockwise toward the inner target.

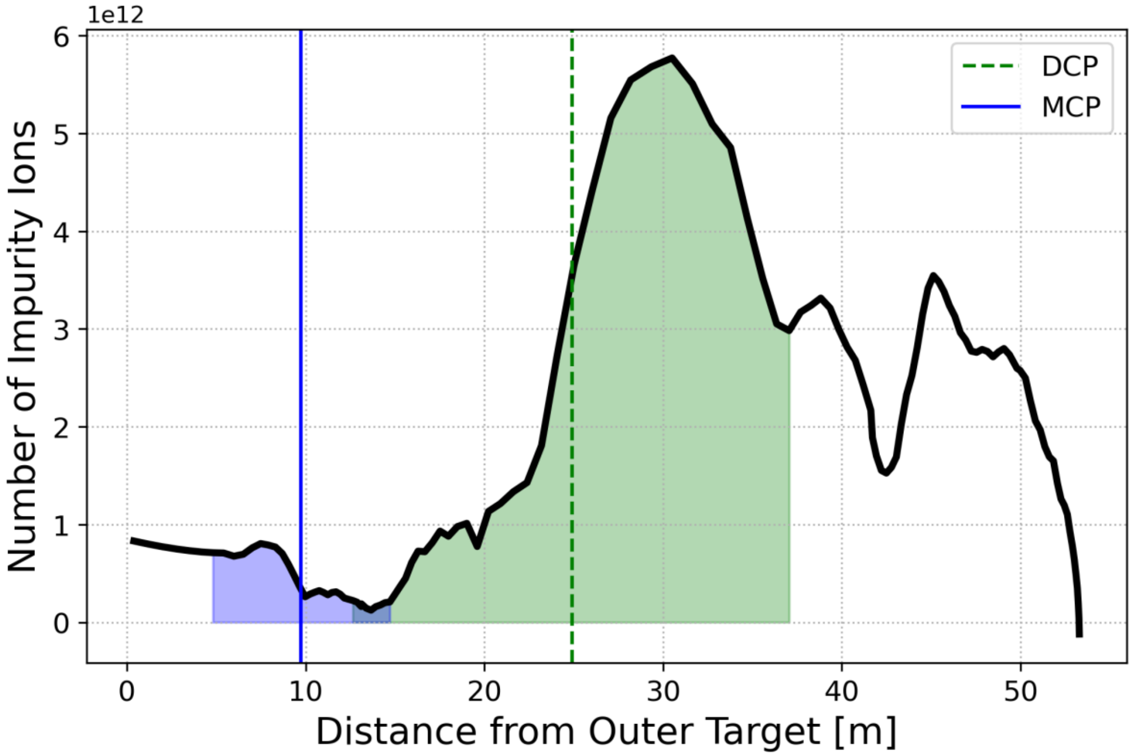

Figure 52. OSP carbon impurity source profile 3 cm radially inwards from the MCP tip location. DCP and MCP locations along the flux surface and their sampling lengths are shaded.

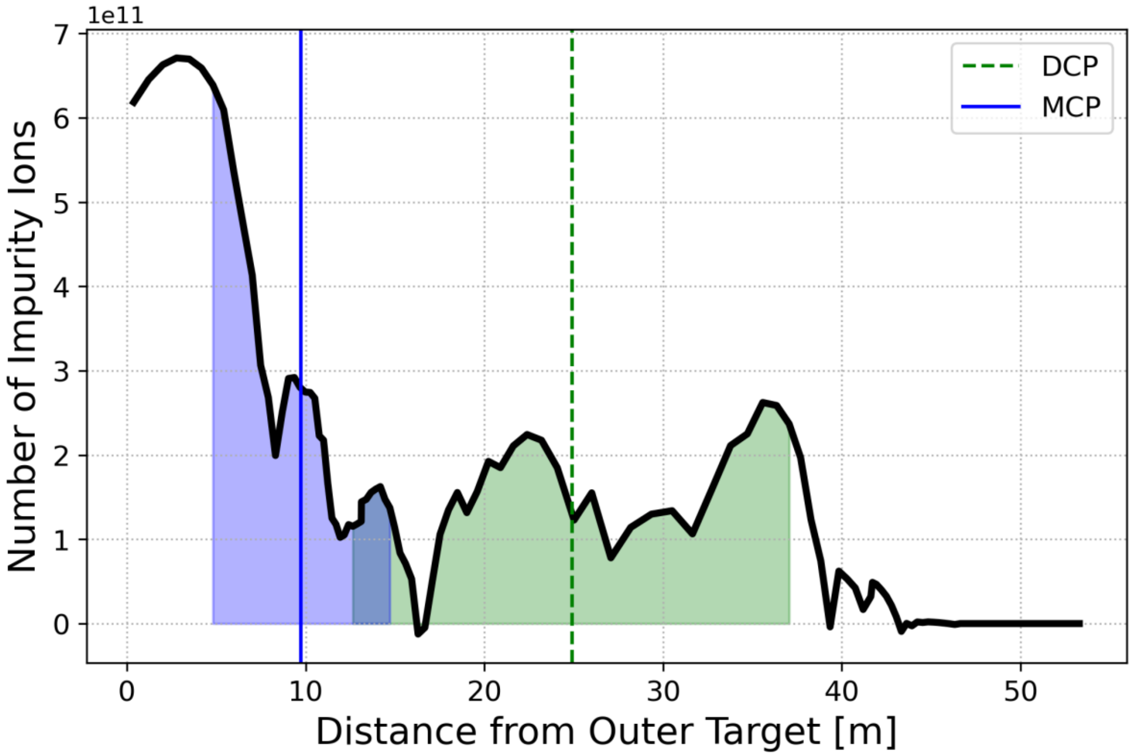

Figure 53. ISP carbon impurity source profile 3 cm radially inwards from the MCP tip location. DCP and MCP locations along the flux surface and their sampling lengths are shaded.

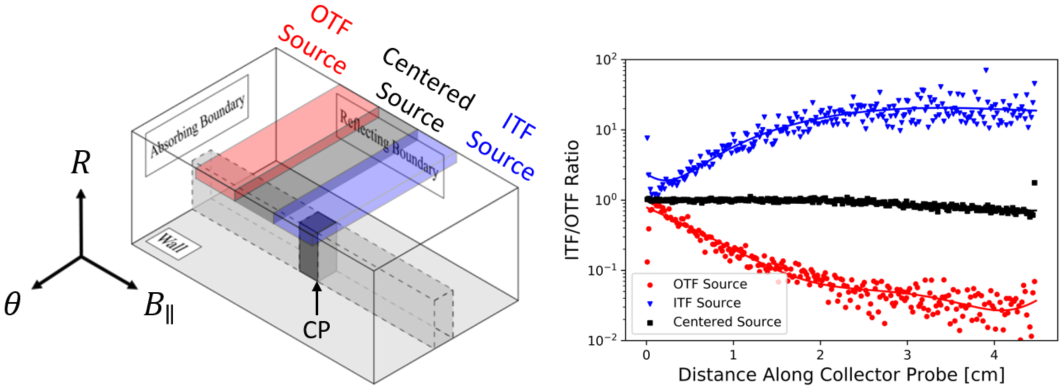

Figure 54. Left: An adaptation of the 3DLIM simulation volume from Zamperini [31]. The simulation volume includes three different impurity sources used to produce the right plot. An arrow points to the base of the DCP while the origin for the simulation is centered at the DCP tip that is closest to the sources. Right: the simulated ITF/OTF deposition ratios for the three unique accumulation positions along with an overlaid polynomial fit.

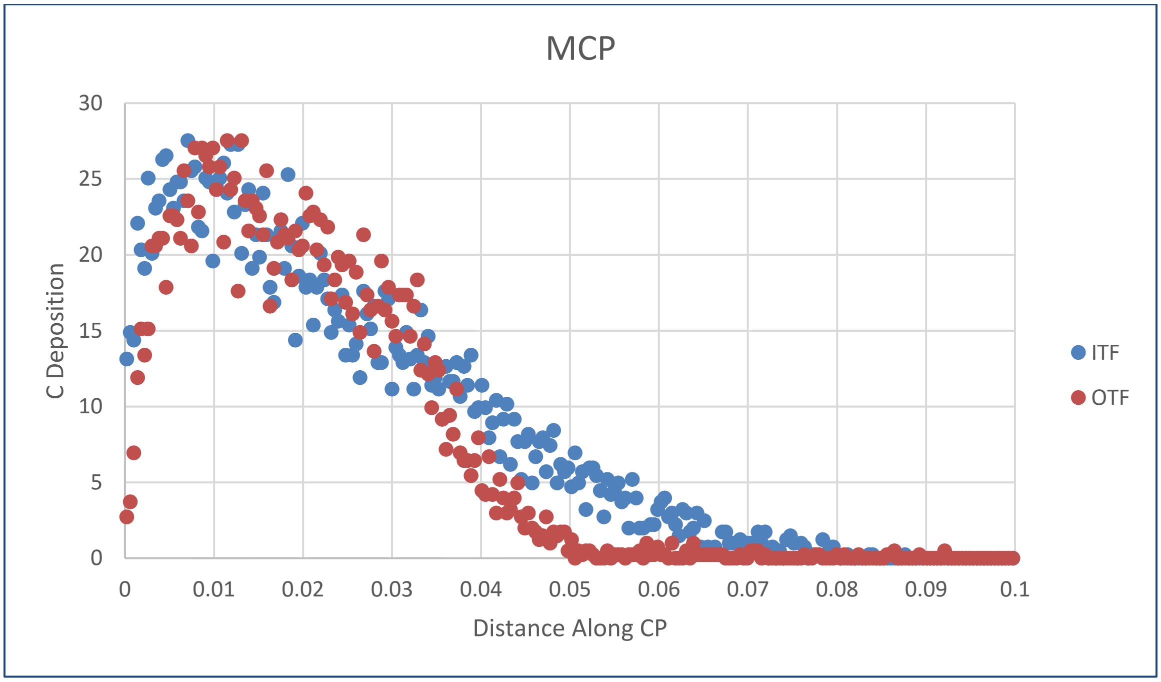

Figure 55. MCP simulated deposition patterns in 3DLIM using the dummy impurity profiles in Figure 47.

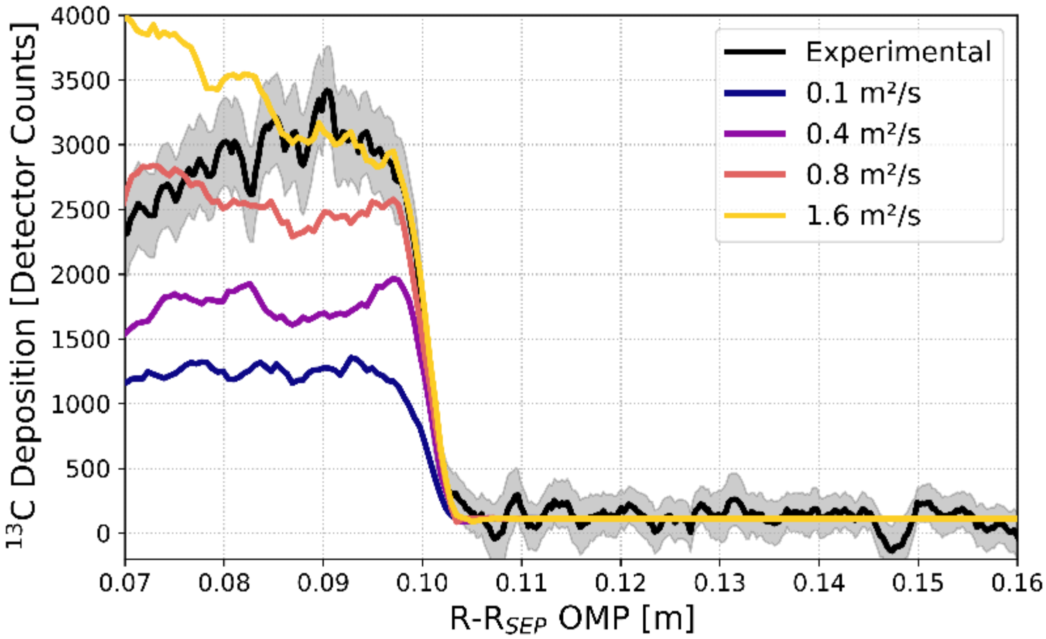

Figure 56. MCP OTF ^{13}C deposition pattern for collection phase 187122-187123. Simulated deposition patterns from 3DLIM are overlaid for a scan in perpendicular diffusion.

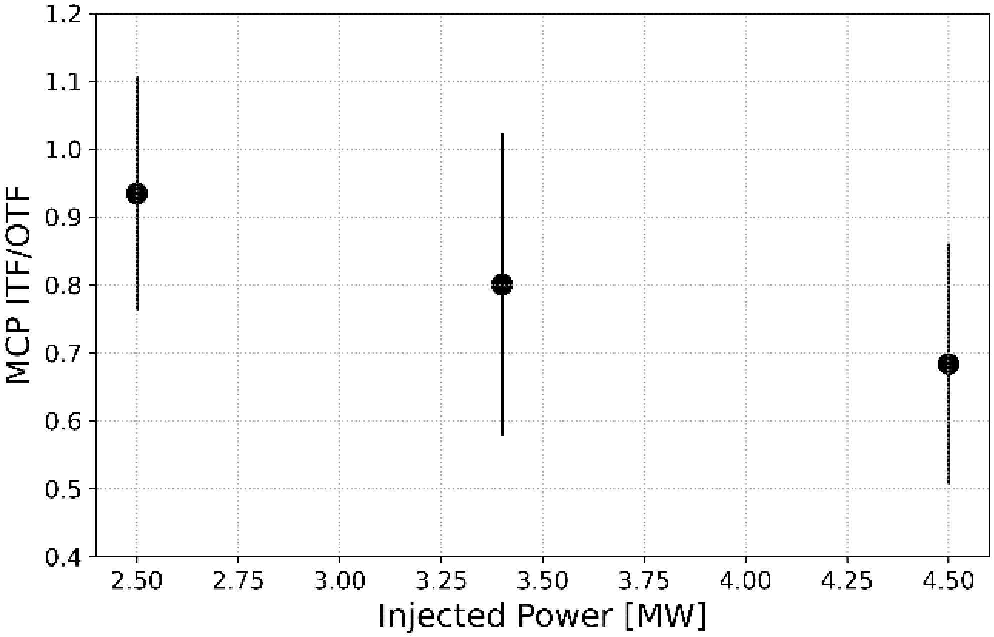

Figure 57. ITF/OTF deposition for the MCPs exposed during each collection phase in Table 5.

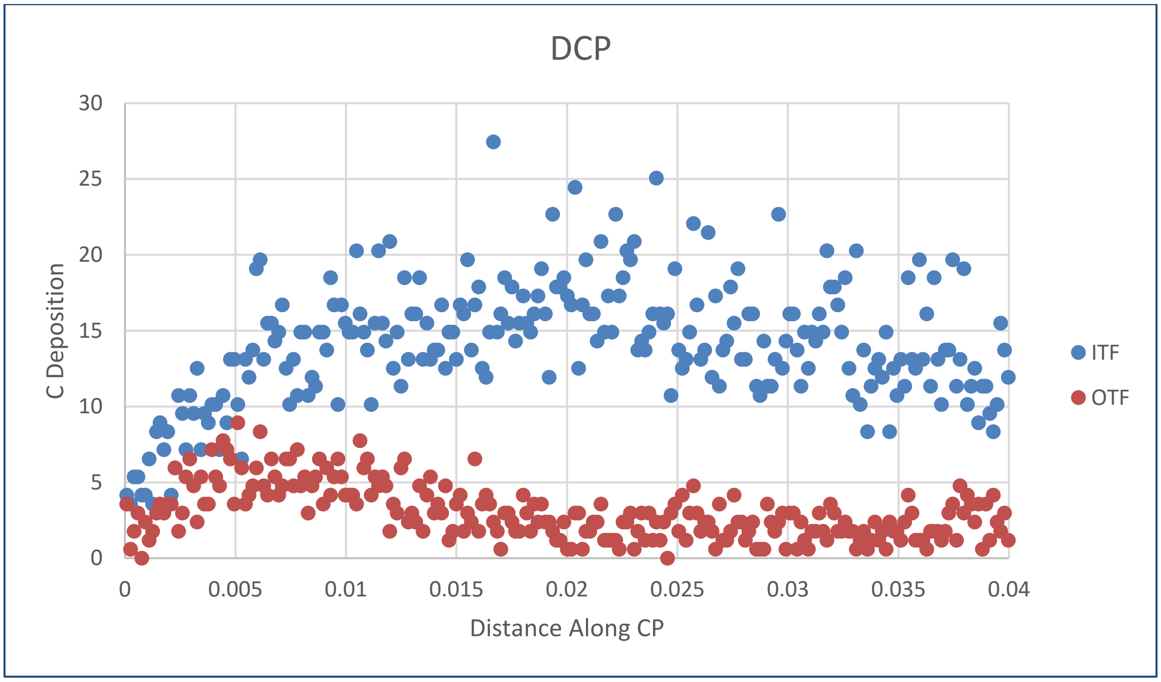

Figure 58. DCP simulated deposition patterns in 3DLIM using the dummy impurity profiles in Figure 47.

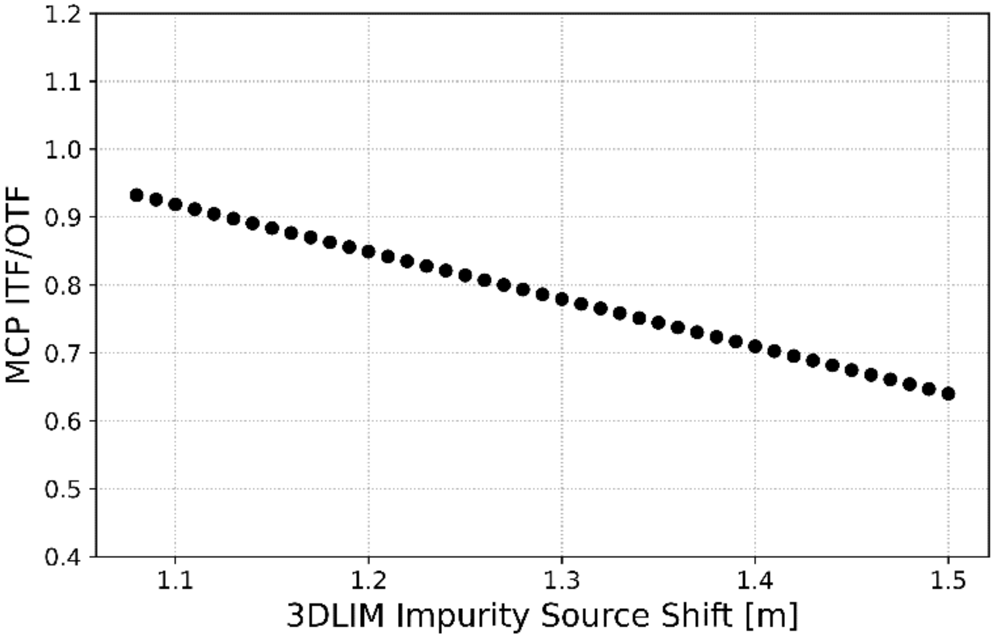

Figure 59. Simulated MCP ITF/OTF carbon deposition ratios for a shifted impurity source.

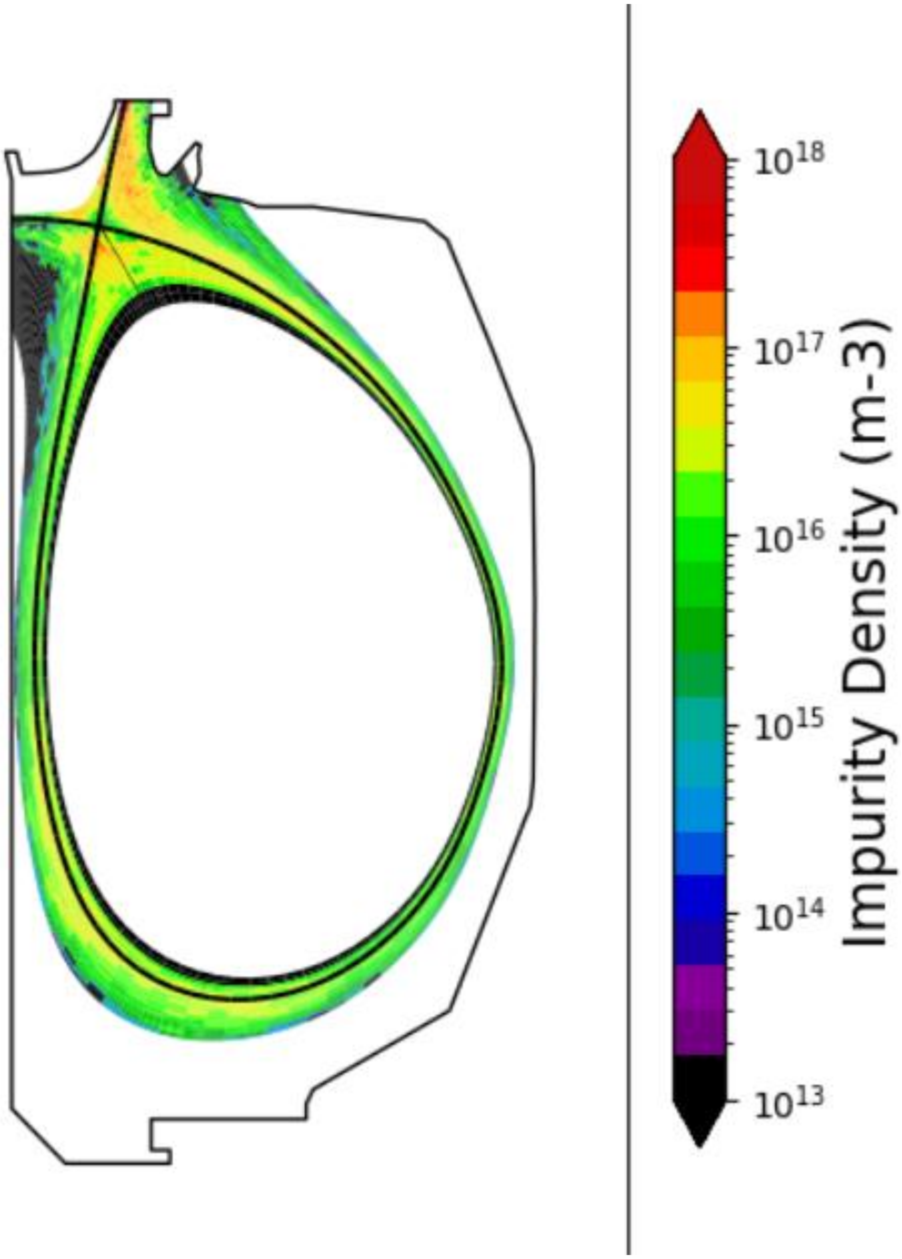

Figure 60 Outer strike point carbon impurity source simulation using DIVIMP where the injection location is directly adjacent to the strike point position.

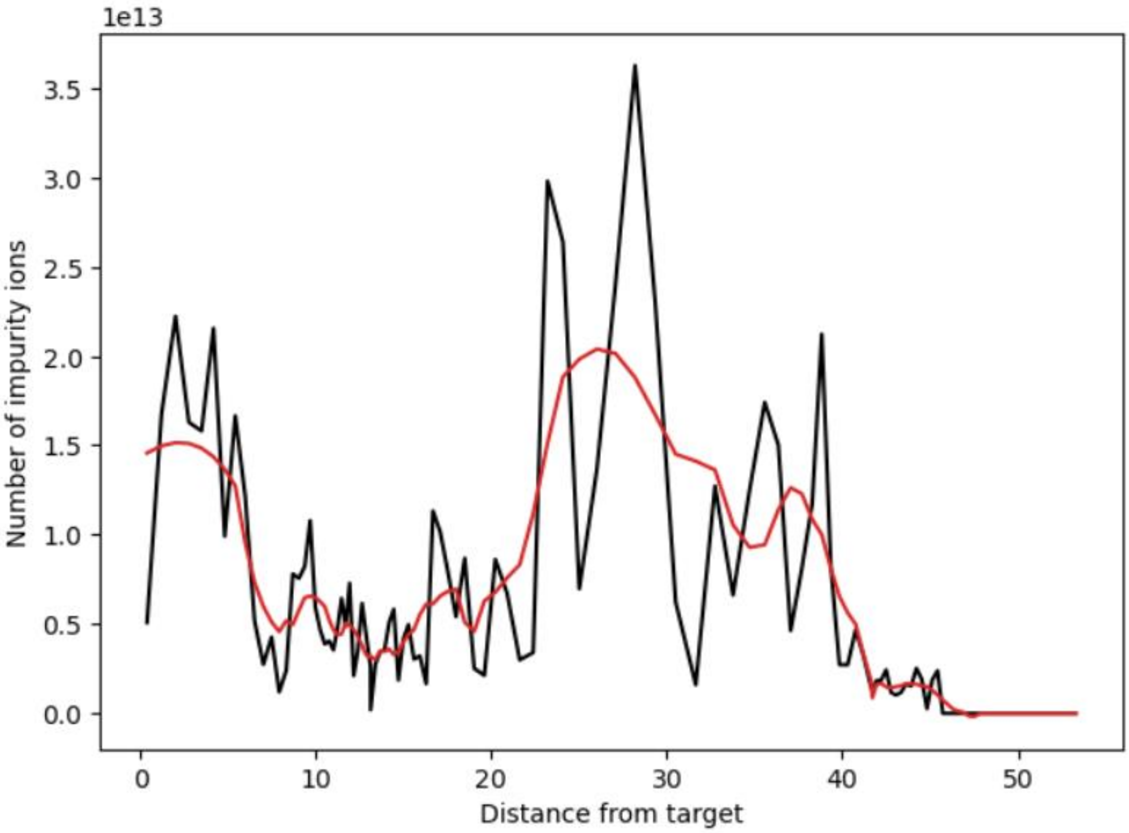

Figure 61 Outer strike point carbon impurity source simulation using DIVIMP for an outer ring. Distance from target begins at outer target and follows the simulation ring clockwise toward the inner target. Associated with simulations shown in Figure 60.

APPENDIX 2: TABLES

Table 1. Molar ionization energy, measured in eV [73]. Note spectroscopic notation defines carbon V as carbon 4+.

Number	Symbol	Name	CI (0)	CII (1+)	CIII (2+)	CIV (3+)	CV (4+)	CVI (5+)
6	C	Carbon	11.26	24.38	47.89	64.49	392.09	489.99

Table 2. Natural versus enriched enrichment fractions for carbon and tungsten

Natural	Enriched
0.9893 ^{12}C, 0.0107 ^{13}C	0.01 ^{12}C, 0.99 ^{13}C (CH_4 or CD_4)
0.0012 ^{180}W, 0.2650 ^{182}W, 0.1431 ^{183}W, 0.3064 ^{184}W, and 0.2843 ^{186}W	< 0.0005 ^{180}W, 0.9299 ^{182}W, 0.0284 ^{183}W, 0.0279 ^{184}W, and 0.0138 ^{186}W

Table 3. Summary of estimates provided by N. Eiditis on the DiMES collector probe disruption forces for the cases of insulation success and failure

Case	- *Effective Insulation*	- *Insulation Breakdown*
F_R	0 N	5.6 kN
F_ϕ	0 N	1.4 kN
F_Z	1.1 kN	1.1 kN
τ_ϕ	0 Nm	152 Nm
τ_R	0 Nm	38 Nm

Table 4. Methane injection experiment shot list for Chapter 3

Set	Diagnostic Phase [Shot]	Collection Phase [Shots]	Injected Power [MW]	I_P [MA]	n_e [m^{-3}]	B_T [T]	UOB [TL/s]
Injection	187106	187116-117	4.5	1.0	2.5 x10^{19}	-2.0	14.3
Control	187106	187119-120	4.5	1.0	2.5 x10^{19}	-2.0	0

Table 5. Methane injection experiment shot list for Chapter 4

Set #	Diagnostic Phase [Shot]	Collection Phase [Shots]	Injected Power [MW]	I_P [MA]	n_e [m^{-3}]	B_T [T]	UOB [TL/s]
Set 1	187105	187113-114	2.5	1.0	2.5×10^{19}	-2.0	14.3
Set 2	187111	187122-123	3.4	1.0	2.5×10^{19}	-2.0	14.3
Set 3	187106	187116-117	4.5	1.0	2.5×10^{19}	-2.0	14.3
Set 4	187106	187119-120	4.5	1.0	2.5×10^{19}	-2.0	0

APPENDIX 3: EXPERIMENTAL MINI-PROPOSAL

MP template: Release 1: 18-10-11, R J Buttery

Date Approved: ____________________ **By:** ______________________________

DIII–D Mini–Proposal

Subject:	**Axisymmetric 13C injection for testing divertor leakage and SOL transport models**	**D3DMP No. 2019-51-01** **revision 5**
From:	**J.H. Nichols, E.A. Unterberg, J.D. Duran, S.A. Zamperini, D.L. Rudakov**	**Date: Aug 23, 2019** **Revised: Jan 13, 2021**

---

1. Purpose of Experiment

Physics hypothesis to be tested or key advance aimed for: The main goal of this experiment is to measure (both indirectly and directly) the poloidal structure of upstream SOL impurity densities following tracer impurity injection at the divertor strike point. These measurements will be used to validate and improve SOL impurity transport models, which predict a poloidally-localized accumulation of impurities in the upstream near SOL. Our experiment aims to address the formation/occurrence of this accumulation from leakage of a divertor target source. Measurements will be taken in a controlled range of well-diagnosed SOL flow regimes to systematically test the plasma flow dependence of this upstream impurity transport, since models predict that changes in the background flow will modify the poloidal location of the theorized SOL impurity accumulation.

Principle result plots: Tracer impurity density as a function of poloidal angle, in multiple SOL flow regimes. A clear difference in impurity distribution with Bt direction.

Impact: The flux of impurities crossing the last closed flux surface from the SOL into the core (one of the key limiting factors for reactor performance) is determined by two factors: extrinsic (e.g. gas seeding/puffing) and intrinsic (e.g. sputtering from material surfaces) impurity production, and transport patterns of these impurities through the SOL. If it is true that SOL transport tends to accumulate impurities in a poloidally-localized reservoir, then it is the impurity density at this reservoir that sets the boundary condition for core contamination, even if the average impurity level is lower. Verifying this impurity accumulation, and understanding the physics behind it, opens the door for designing control mechanisms to mitigate and/or eliminate the impurity's impact on core performance, potentially enabling lower core impurity levels for a given SOL impurity production rate.

Predict first: Fluid models of SOL impurity transport often predict an upstream poloidal accumulation of impurities in the near SOL, due to large parallel ion temperature gradients (see background).

Additional scientific goals or piggy-back studies:

- Coincident: Characterize divertor retention of low-charge-state impurities for similar upstream conditions, but different drift directions.
- Coincident: Obtain comprehensive SOL plasma flow, density, and temperature data for development of an empirical-interpretive SOL model with drift-dependent flows.
- Coincident: Measure time constants for impurity retention in various SOL locations for development of a coupled reservoir model for non-recycling impurities.
- Coincident: Utilize different gas puff rates to characterize effect of impurity pressure gradients on divertor leakage and core penetration probability.
- Time-permitting: Test the feasibility of modifying upstream impurity behavior with puff-and-pump control actuators.

2. Background

Overall, SOL impurity transport is arguably the poorest-understood component of the chain of mechanisms that link impurity production due to PMI (erosion, sputtering, etc.) with core impurity contamination. Core contamination must be kept under control in future reactors in order to obtain high fusion performance, especially in devices with high-Z PFCs like tungsten. Therefore, understanding is needed in both steady-state and transient SOL conditions. This experiment aims to isolate and explore some of the mechanisms that are hypothesized to govern steady-state SOL impurity transport, as a precursor to the development of control actuators that may enable better core impurity mitigation.

Isotopic tracer injection (see [Stangeby JNM 2011] and references within) has been employed over the past 20+ years at DIII-D (and other devices) to explore material migration and SOL impurity transport. Many of these experiments were limited to a single configuration, due to the requirement that the experiment be run at the end of a campaign so as not to disturb the tracer material deposited on the PFCs. Advances in removable SOL collector probes [Donovan RSI 2018] and new spectroscopic techniques offer the promise of shot-to-shot resolution, enabling the study of far more configurations than before as well as actual parameter scans.

Impurity injection experiments at DIII-D in the mid-2000s contributed to a general worldwide understanding that impurities sourced from the main chamber would be frictionally coupled to fast SOL flows, and transport to the inner divertor and deposit as amorphous codeposited layers, at least for favorable ion grad-B direction [Stangeby JNM 2011]. However, in most of these experiments the tracer impurities were quickly entrained in the far SOL, so very little information was gained about impurity transport in the near SOL, which has stronger parallel temperature gradients and thus may have qualitatively different transport behavior.

The tungsten Metal Rings Campaign (MRC) on DIII-D in 2016 offered a new opportunity for tracer impurity studies, since W from either isotopically-distinct ring could serve as a tracer in the C environment of DIII-D. And since W sputtered at the divertor strike point could easily make it into the near SOL, this campaign allowed observation of hence-unobserved near SOL phenomenon.

One of the striking results of the MRC was the apparent evidence of an upstream (on the opposite side of the midplane as the active divertor) accumulation of W in the near SOL in certain configurations. The key diagnostic evidence for this was more W being found on the inner target facing side (away from the W source) of a midplane collector probe, and this interpretation was supported by OEDGE-DIVIMP modeling [Elder NME 2019] [Zamperini NME 2019], as seen in Figure 1. This upstream impurity accumulation has long been theorized by models based on 1D force balance [Neuheuser NF 1984] [Stangeby NF 1995] and often shows up in computer simulations [Senichenkov PPCF 2019], but had not been observed experimentally.

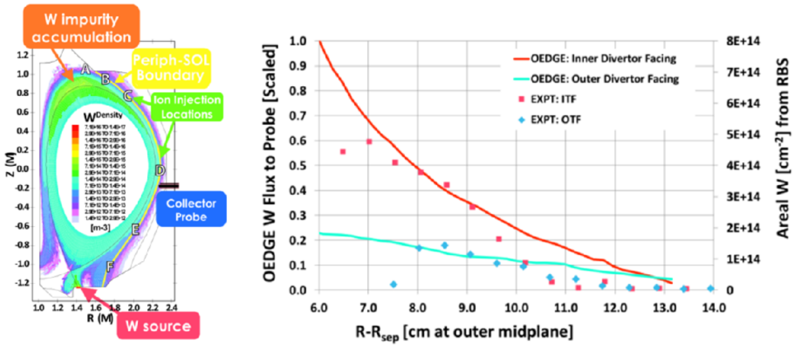

Figure 1: OEDGE-DIVIMP simulations of MRC collector probe with higher W content on the inner-target-facing (ITF) side, consistent with upstream W accumulation. Adapted from [Elder NME 2019].

However, this was not the case for every collector probe exposed during the MRC, during which many scenarios with widely varying shape, density, confinement regime, and injected power were run. As seen in Figure 2, one of the strongest predictors of which side of the collector probe had more W was Bt direction, which was not tightly controlled during the MRC experiments.

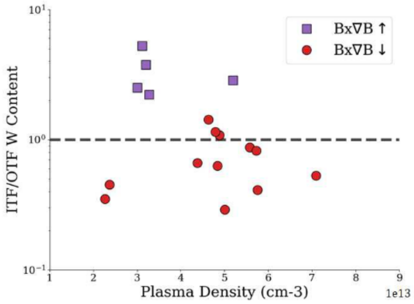

Figure 2: Ratio of W content observed on ITF and OTF sides of all MRC collector ptobes, as a function of Bt direction and electron density. From [Zamperini unpublished].

An expansion of previous 1D fluid models is in development to explain the MRC results [Stangeby NF 2020], building as well off of recent SOLPS-ITER simulations of impurity transport in AUG [Senichenkov PPCF 2019]. Under this model, the impurity velocity can be approximated by the sum of the background plasma flow velocity and a term proportional to the parallel ion temperature gradient:

$$\boldsymbol{v_z \approx v_i + \frac{e\tau_s\beta_i}{m_z}\frac{dT_i}{ds}}$$

When the impurity velocity goes to zero, this model predicts that accumulation can occur. Since the two terms are sometimes opposite in sign, changing the plasma velocity can shift the location of the impurity velocity zero crossing. The primary goal of this experiment is to actuate the SOL plasma flow velocity in a controlled fashion and observe the upstream impurity response, in order to evaluate the soundness of this transport model.

A large multi-machine effort, including DIII-D, has established the general pattern of SOL flows in tokamaks, at least for L-mode operation (see [Asakura JNM 2007], [Boedo JNM 2009], and references within). A key feature of these flows is that the qualitative character changes dramatically when reversing Bt, with the flow stagnation point near the outer divertor in favorable ion grad B and near the crown in unfavorable ion grad B, as seen in Figure 3. However, when changing the average electron density of a discharge, the SOL flow shape appears to stay the same but the magnitude changes, as seen in Figure 4.

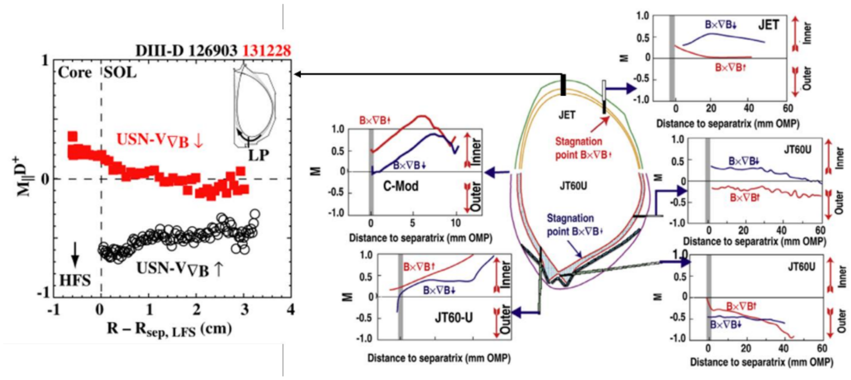

Figure 3: Multi-machine SOL flow patterns at different poloidal locations as a function of Bt direction. Adapted from [Boedo JNM 2009] and [Groth NF 2009].

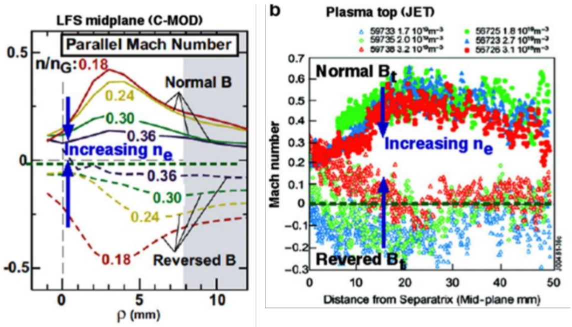

Figure 4: Multi-machine SOL flows as a function of electron density and Bt direction. Adapted from [Asakura JNM 2007].

Based on these observations, in this experiment we expect the Bt direction to be a major actuator of upstream impurity behavior (as observed in the MRC), and the electron density to be a smaller actuator. Of course, this expectation will be tested!

This experiment builds off knowledge gained during the MRC, and informs further experiments that may be carried out during campaigns such as SAS-1W.

3. Experimental Approach

Isotopically-marked deuterated methane (13CD4) will be used as the source of tracer carbon in this experiment. 13C can be differentiated from natural C (primarily 12C) via surface analysis techniques like NRA and LAMS [Duran FST 2019], making it possible to isolate the carbon deposition on collector probes that comes from the tracer gas versus the background C that is ubiquitous in DIII-D. Methane was chosen because 13CD4 is reasonably easy to procure, and methane dissociation models are already incorporated in many SOL impurity transport codes.

As a proxy for material sputtered from the outer strike point, this methane will be injected into the outer divertor leg of an **USN plasma via the upper outer baffle (UOB).** A USN shape is chosen over a LSN shape so that the X-point probe and DiMES (both in the lower divertor) can be used as upstream SOL diagnostics.

The UOB is chosen for two reasons: (1) the three injection valves and baffle structure make injection from the UOB roughly toroidally symmetric, making analysis considerably easier compared to toroidally-asymmetric gas inlets; and (2) as the MRC tungsten experiments have shown, it is necessary to have tracer impurities reach the near SOL in order to observe accumulation-like effects, making injections from locations like the LOB that have to penetrate the far SOL less attractive.

A **gas injection rate of 10 Torr-L/s** will be used, with the valve voltages determined using the recent CH4 flow rate calibration. This gas rate was chosen to maximize C signal while minimizing its perturbative effect on the outer divertor plasma. The exact flow rate may change depending on the results of Phase 1 shots.

We will use a two-pronged approach to measure the tracer 13C in the upstream SOL: indirectly via collector probes at MiMES and DiMES, and directly via various spectroscopic arrays. These approaches are both powerful but not entirely tested, and utilizing both represents an important risk mitigation strategy.

A **double-sided collector probe at MiMES** was successfully deployed during the MRC, and a similar double-sided design will be used at MiMES for the current experiment. Collector probes work by effectively attracting any impurities within a certain parallel distance (the sampling length) on a flux tube intersecting the probe. The sampling length of a collector probe scales with its diameter squared, so 3 cm diameter probes will be used to get a relatively large sampling length of 3-5 m [Donovan RSI 2018].

Likewise, a **double-sided collector probe will be deployed for the first time on DiMES**. Compared to the MiMES probe, the DiMES probe will be shorter and spatially fixed, but will have the same 3 cm diameter. This probe will sample the crown of a USN plasma, predicted to be a key region for SOL impurity accumulation.

Collector probes are typically limited to the far SOL due mainly to re-erosion/sputtering concerns, meaning that they only collect impurities that have diffused out of the near SOL and into the far SOL. In the MRC, the interpretation was put forth that more W would be found on the side of the collector probe facing a region with higher near SOL W density, since that would lead to more radial W diffusion into the far SOL. Thus, the ratio of an impurity on the inner-target-facing (ITF) versus outer-target-facing (OTF) side serves as an indirect measurement of whether there is a higher impurity density in the near SOL upstream or downstream of the probe. Comparing this ratio at both the outer midplane and crown via the MiMES and DiMES collector probes, respectively, will enable further poloidal localization of the near SOL impurity source.

In addition, we will use a combination of existing and newly developed spectroscopic diagnostics to measure carbon densities throughout the device. Since most spectroscopic diagnostics cannot differentiate between 13C and 12C, each shot in the experiment will include a flattop period prior to gas injection, during which background signals can be measured and subsequently subtracted from the with-gas signals. The percent change in the measured carbon densities thus will be proportional to the density of the tracer 13C.

At the temperatures characteristic of the upstream near SOL (50-100 eV), C4+ is the primary charge state of carbon, and thus a poloidal localization of C V emission would be representative of impurity accumulation. C V lines are rare outside of the EUV/VUV, but we have identified a discernable spectral line at 494.45 nm that could be C V (or B V). If this line is C V, then the spatial coverage of MDS will potentially allow for the direct measurement of C4+ at many poloidal locations. **MDS** will be tuned to 465 nm (C III) during the Setup Phase, but will be moved to 495 nm to measure this potential C V line during the Diagnostic Phase. MDS will be moved again to 581 nm (C IV) during the Collection Phase. The following viewchords will be instrumented to view primarily the upstream (lower divertor) plasma:

- SA, R0, T2, T3, T4, T5, T6, T7, L2, L3, L4, L5, L6, U4, U5, U6

DivSPRED, with the 450 gr/mm grating, will be used to measure VUV C V lines (at 22.7 and 24.8 nm) through the DiMES chord, either to cross-calibrate the MDS SA chord or act as a backup measurement.

Either one of the **HR-VUV** spectrometer or the **WiSE** spectrometer system is a desired diagnostic, to monitor C V lines at 227 nm.

CER will be set up with interleaved spectrometers set to C VI 529.1 nm and C IV 772.6 nm, allowing radial profiles of n_C6+ and n_C4+ at half radial resolution. The C4+ profile will be used to cross-calibrate the MDS R0 chord (or be a backup measurement), while the C6+ profile will serve to monitor the core carbon inventory in each configuration. The 330R and 30L beams will be modulated (and 90 degrees out of phase) to provide high-quality edge/SOL CER data (via the vertical and tangential CER chords intersecting 330R), in conjunction with axis-to-edge measurements of the core C content (via the tangential CER chords intersecting 30L).

Similar to previous methane injection experiments, the **Tangential TV** (TTV) cameras will be deployed in both the upper and lower divertors, with C II and C III filters to measure C+ and C2+ distributions. The upper divertor TTVs will be especially useful for diagnosing how divertor retention of C changes as we change configurations.

Upward-facing **filterscope** arrays with D_alpha and C III filters will be utilized to help constrain plasma reconstructions, and help evaluate low-charge-state C leakage.

A goal of this experiment is obtaining the plasma diagnostic data needed to model each one of our configurations with interpretive SOL reconstruction tools like OEDGE. Thus, it is important to have as many of the upper divertor (both outer and inner) embedded **Langmuir probes** as possible.

The primary electronics system can support 20 embedded probes, so the following probes will be active during the experiment, covering the entire non-SAS upper divertor:

- C-1, C-2, C-3, C-4, C-5, D-1, D-2, D-3, D-4, P-1, P-2, P-3, P-4, P-5, P-6, P-7, A-1, A-2, A-3, A-4

A secondary electronic system for Langmuir probes can support 8 additional measurements, and will be hooked up to the following probes:

- A-15, A-16, A-17, A-18, S-1, S-2, S-3, S-4

Throughout the experiment, the **Thomson Scattering** system will be in Configuration #5: HIRES-MID, SHELF-12, SAS-4. The HIRES-MID setting enables high-resolution measurements of ne and Te in the pedestal and near SOL above the outer midplane, while the SHELF-12 and SAS-4 settings allow simultaneous characterization of ne and Te in the crown and divertor entrance of our USN plasma shape.

Since SOL flows are a key driver of impurity transport, it is critical to make good measurements of the flows in as many locations as possible. Since near SOL flows are the most important component for impurity accumulation physics, **plunging Mach probes** will be an essential diagnostic: during the "Diagnostics Phase" (see below), the X-point probe and MiMES will be outfitted with their multi-probe reciprocating Langmuir probe heads. At the low powers used in this experiment (Pnbi<1.5 MW), the reciprocating probes should be able to reach the separatrix with little risk. The appropriate plunge depth will be determined on the first shot of the day. **Periscope CIS** is a desired diagnostic to provide poloidally-comprehensive measurements of far SOL flows.

Measurements of SOL ne and Te made with the **midplane and X-point reciprocating probes**, as well as DTS, during the "Diagnostics Phase" will be used to estimate the expected heat flux on the DiMES collector probe in each configuration. Prior to the insertion of the DiMES collector probe in the "Collection Phase", each configuration will be evaluated to ensure the plasma shape and SOL conditions are compatible with thermal limits determined in the DiMES collector probe design review.

Scans to run:

- **Forward vs Reverse Bt (two ½ days)**
    - Note: in USN, Reverse Bt is the favorable $B \times \nabla B$ direction.
- **Electron Density**

As described in the Background, we expect the Bt direction and plasma density to be control knobs for the plasma SOL flows, with Bt direction being a "major" knob that changes the qualitative flow patterns, and density being a "minor" knob that mainly changes the magnitudes. We would like to run 3 different density points (2.0, 3.5, 5.0 e19 m-3) in each Bt direction, for a total of 6 configurations.

In each configuration, the average injected power will be held constant at 1.0-1.5 MW (exact value depends on beam voltages), to minimize changes in temperature gradient-driven SOL transport. This power level was chosen so that the discharges would reliably stay in **L-mode**, regardless of Bt direction. ELMs would greatly complicate analysis, so staying in L-mode is highly preferable.

Each of our half days will be **split into 3 discrete "phases**", differing according to the diagnostic configuration and strike point behavior. Each plasma configuration will be run in both the Diagnostics and Collection phases.

- Setup phase: Vary outer strike point location and methane puff rate to find optimum values.
- Diagnostics phase: Reciprocating probes are active, outer strike point is swept for LP/TS profiles.
- Collection phase: Collector probes are active, strike point is fixed.

It takes about 30-40 minutes to reconfigure MiMES between collector probes and reciprocating probes, so on each half day, all configurations will be run in the Diagnostics Phase before moving on to the Collection Phase.

Setup Phase

A USN shape is required for this experiment. An X-point decently far from the upper divertor (RXPT~1.23 m, ZXPT~1.04 m) is desirable to minimize plasma contact with the SAS baffle. A plasma current of 1.0 MA is requested. Outer and inner gaps should be around 7 cm. GAPBOT of ~20 cm is desirable, to ensure the X-point reciprocating probe can reach the last closed flux surface. The EFITRT1 simulation known as **969002.2200** (see below) represents the desired target shape. The patch panel from **178351** can be loaded in order to develop this shape. The GASA fueling programming for 178351 can be recycled to establish the discharge in the first 1500 ms, and then modified with GASB to reach the desired density during flattop.

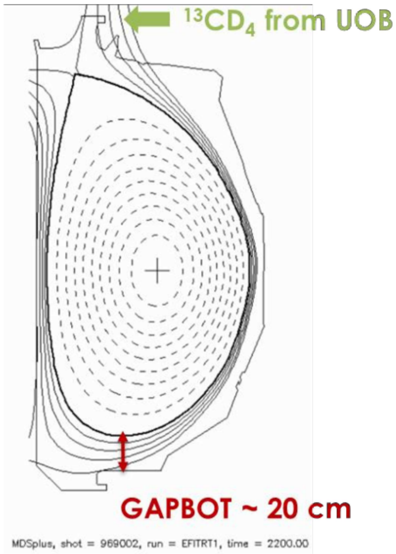

Figure: Reference shape

Changes to the shape should be tested in Setup Phase shot 1.1, including a short UOB 13CD4 puff at 20 Torr-L/s to ensure the shape is controllable during gas injection (see below). Additionally, reciprocating probes can take test plunges as needed, and DTS will be in the shelf configuration to obtain crown plasma data, which will be used to confirm that the heat flux to the DiMES collector probe will remain below administrative limits.

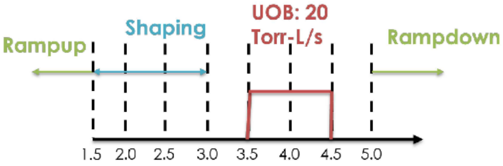

Figure: Timing schematic for Setup Phase 1.1

On the second shot of the Setup Phase (1.2), both the OSP location and UOB puff rate will be varied in order to find values that maximize 13C penetration into the upstream SOL, while also trying to minimize perturbations to the divertor plasma. 3 strike point sweeps across the upper divertor will be performed, each 800 ms long and ranging from RVSOUT=1.295 m / ZVSOUT=1.348 m (969002 @ 2000 ms) to RVSOUT=1.395 m / ZVSOUT=1.348 m (969002 @ 2500 ms). The UOB gas puff rates will be set to 0, 10, and 20 Torr-L/s during each of these sweeps, respectively (see below).

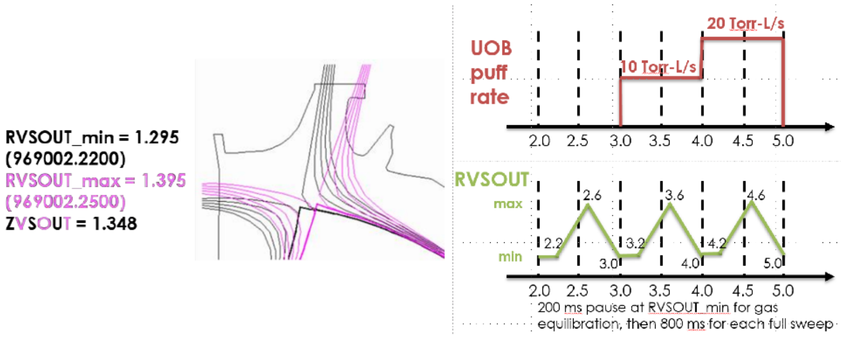

Figure: Strike point sweep parameters and timing schematics for Setup Phase 1.2

The level of 13C entering the upstream SOL will be evaluated by increases in CIII signals in the vicinity of the upper X-point, measured by MDS and TTV, that correlate with changes in the UOB puff rate. Plasma perturbations will be evaluated with Thomson scattering and target Langmuir probes.

If a suitable combination of RVSOUT and UOB puff rate is found in 1.2, the experiment will move to the Diagnostics Phase. If not, another Setup Phase shot (1.3) will be taken to test strike point positions further up the SAS baffle, and higher UOB puff rates (see below).

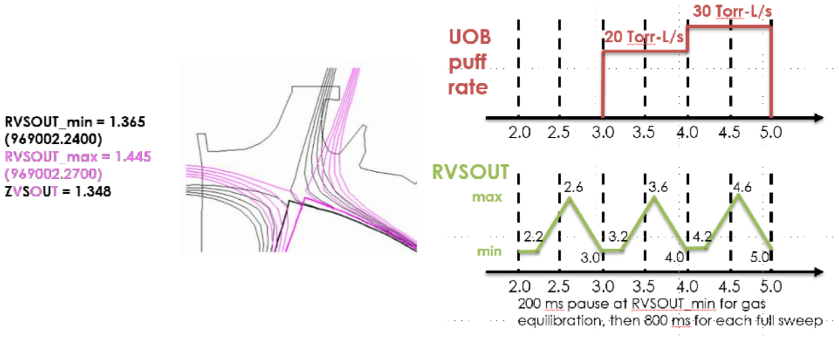

Figure: Strike point sweep parameters and timing schematic for Setup Phase 1.3 (if needed)

Diagnostic Phase

13CD4 will be puffed from the UOB at the same rate during both the Diagnostics Phase and Collection Phase. Puffing gas during the Diagnostic Phase enables a measurement of the SOL plasma that includes any perturbations due to the gas puff. The exact rate will depend on the results of steps 1.2/1.3 in the Setup Phase.

During the Diagnostics Phase, the outer strike point will be swept across the upper divertor. Two sweeps will be done, to capture plasma data both with and without methane gas injection. 13CD4 will be puffed from the UOB from 3.1-4.5 s, at the rate determined in Setup Phase 1.2/1.3. At the minimum OSP location, RVSOUT=1.295 m, while at the maximum OSP location, RVSOUT=1.350 m. These RVSOUT locations will be shifted accordingly if a strike point further up the SAS baffle is used. Both reciprocating probes will be plunged at 2.1 and 3.5 s, at times when the strike point and gas status are fixed. DTS points in the SAS configuration will be used to characterize the near-divertor plasma during the strike point sweep.

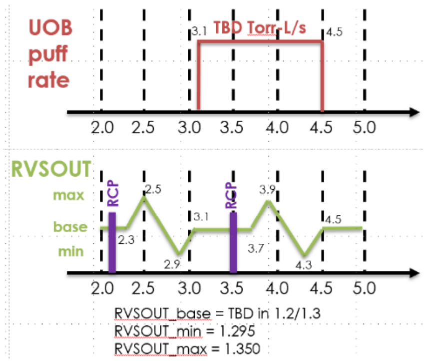

Figure: Timing schematic for all Diagnostic Phase shots (2.1-2.4)

<u>Collection Phase</u>

During the Collection Phase, the outer strike point will be held fixed at a value determined by shots 1.2/1.3 of the Setup Phase. This value will be chosen to maximize penetration of the injected methane into the upper divertor near SOL. UOB 13CD4 will be puffed (at a constant rate) from 2.5-4.5 s. The X-point reciprocating probe will be plunged at 2.1 and 3.5 s.

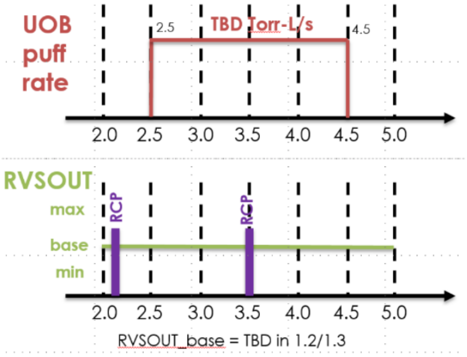

Figure: Timing schematic for all Collection Phase shots (3.1-3.4)

In between each Collection Phase shot, there will be a short pit run to swap collector probes at MiMES and DiMES.

Analysis & Roles:

Provide list of roles for executing the experiment on the day, and who will do them.

- MP Author: Nichols
- Session Leader: Unterberg
- Diagnostic Coordinator: Nichols
- Inter-shot Analysis: Zamperini, Duran
- Physics Operator: Shafer
- MiMES and DiMES Samples: Rudakov, Ren, Abrams
- Reciprocating Probe Guru: Boedo/Rudakov
- Langmuir Probe Guru: Watkins
- Beam Operator: Wilcox
- Spectroscopy Setup: Wilcox, McLean, Scotti
- CER operator: Chrystal or deputy

Provide list of analysis tasks to be pursued after experiment completed, and who will do them (please also review analysis needs with your physics area meeting, once experiment has been run).

- Collector probe sample NRA: Wampler
- Collector probe sample LAMS: Duran
- MDS analysis: Nichols, Unterberg
- LP analysis: Watkins, Nichols, Zamperini
- Mach probe analysis: Boedo, Zamperini, Nichols
- TS analysis: Zamperini, Nichols
- CERFIT: Chrystal or deputy
- OEDGE-DIVIMP modeling: Nichols, Zamperini, Elder

4. Resources

4.1. Tokamak

First half day: USN L-mode, reference 178351, forward Bt, Ip=1.0 MA, Bt=-2.0T.

Second half day: USN L-mode, reference 178351, reverse Bt, Ip=1.0 MA, Bt=2.0T.

Shape: On both half days, maintain reference X-point location. GAPOUT=GAPIN=7 cm (as in reference). Try to match GAPBOT and lower triangularity to 969002.2200.

Prefer to not immediately follow a boronization. Morgan Shafer is Physics Operator.

4.2. Neutral Beams

Pnbi ~ 1.0-1.5 MW.

We will use 330RT and 30LT for this experiment, to enable high-resolution CER measurements in the core, edge, and SOL. Beams will be kept at full voltage to maintain CER calibrations, but will be run at reduced duty cycle to achieve the desired average power level.

Beam programmer is Bob Wilcox, who will finalize the duty cycle calculations.

4.3. ECH

None.

4.4. Diagnostics

Essential:

- MiMES collector probe
- DiMES collector probe
- Core/Edge Thomson Scattering (config #5)
- Langmuir probes (upper divertor suite: C-1, C-2, C-3, C-4, C-5, D-1, D-2, D-3, D-4, P-1, P-2, P-3, P-4, P-5, P-6, P-7, A-1, A-2, A-3, A-4; secondary system: A-15, A-16, A-17, A-18, S-1, S-2, S-3, S-4)
- MDS (prefer chords SA, R0, T2, T3, T4, T5, T6, T7, L2, L3, L4, L5, L6, U4, U5, U6)
    - C III 465 nm: typical integration time/gain
    - C V 495 nm: integration time = 200 ms, gain = 10
    - C IV 581 nm: integration time = 100 ms, gain = 20
- Core/Edge/SOL CER (interleaved C6+ and C4+)
- CO2 interferometer
- Upper TTV (C II and CIII)
- Calibrated UOB methane flow rate

Highly desirable:

- Midplane reciprocating probe/Mach head
- X-point probe/Mach head
- Divertor Thomson Scattering (config #5)
- Filterscopes (Dalpha and C III)
- Lower TTV (C II and C III)
- DivSPRED
- HR-VUV spectrometer
- Bolometers
- Periscope CIS
- ASDEX gauges

Diagnostic Coordinator: Nichols

4.5. *Gas Systems*

UOB: C13D4 with pre-programmed release (see Experimental Approach).

Standard D2 fueling from GASA, GASB as needed. Suggest using GASA programming from reference shot (178351) for rampup, then reaching desired density with GASB.

No pellets.

4.6. *Cryopumps*

All cryos warm. Glow between shots.

4.7. *IC-coil requirements*

None required. Physics operator can use them if they want.

5. Experimental Plan

Reverse Bt half day

1. **Setup Phase (2-3 shots, 12 min each)**
   RCP on MiMES; X-pt probe active; glow between shots
   1.1. Establish reference discharge with modified shape, and determine appropriate reciprocating probe penetration depth.
   1.2. Determine optimum RVSOUT and UOB flow rate for maximizing methane penetration into upper divertor, while minimizing plasma perturbation. Perform 3 OSP sweeps, during gas puffs of 0 (bkg), 10, and 20 Torr-L/s. Look for OSP position that gives maximum C II/ C III emission near X-point, preferably while minimizing change in upstream TS data.
   If adequate C emission at X-pt is found, continue to 2.1
   1.3. (if necessary) Extra steps to determine optimum RVSOUT and UOB methane gas puff rate. Sweep OSP further up the vertical target, and puff methane at 0, 20, and 30 Torr-L/s.
   Decision point: Choose RVSOUT and UOB methane gas puff rate to use for future shots.

2. **Diagnostics Phase (4 shots, 12 min each)**
   RCP on MiMES; X-pt probe active; OSP swept; glow between shots
   2.1. ne=3.5e19 m-3
   2.2. ne=2.0e19 m-3
   2.3. ne=3.5e19 m-3, with 2x the UOB 13CD4 rate as 2.1
   2.4. ne=5.0e19 m-3

Long pit run (30 min) to set up hardware for Collection Phase.

3. **Collection Phase (4 shots, 20 min each)**

CP on MiMES; X-pt probe active; OSP fixed; pit runs between shots
3.1. ne=3.5e19 m-3
Pit run: swap out collector probes on MiMES and DiMES
3.2. ne=2.0e19 m-3
Pit run: swap out collector probes on MiMES and DiMES
3.3. ne=3.5e19 m-3, with 2x the UOB 13CD4 rate as 2.1
Pit run: swap out collector probes on MiMES and DiMES
3.4. ne=5.0e19 m-3
Pit run: swap out collector probes on MiMES and DiMES

Total for Reverse Bt half day: 10-11 shots, 4 hours

Forward Bt half day

Same shot plan as Reverse Bt half day.

Total for Forward Bt half day: 10-11 shots, 4 hours

Total for MP: 20-22 shots, 8 hours

Additional half day (potential Director's reserve candidate)

Forward Bt. Upper inner cryo cold.
Goal is to increase inner-target-directed SOL flows by turning on the upper inner cryo, and see how this modifies upstream SOL impurity behavior.
Try to use same plasma configurations as main experiment.

Forward or Reverse Bt. Further fill in matrix of UOB puff rate vs. upstream density.
Goal is to evaluate role of impurity pressure gradient forces in divertor leakage and core penetration.
Try to use same plasma configurations as main experiment.

6. Analysis Plan and Deliverables

Main plots obtained from this experiment:

- In-situ: upstream C V emission vs.

  - poloidal angle (crossed MDS viewchords enable poloidal localization of signals)
  - electron density (minor knob for SOL flows)
  - Bt direction (major knob for SOL flows)
- Ex-situ: ITF and OTF 13C density on midplane and crown collector probes vs.
  - R-Rsep (radial decay lengths are measure of radial transport)
  - electron density (minor knob for SOL flows)
  - Bt direction (major knob for SOL flows)
- 13C/12C ratio on collector probes (measure of divertor leakage)

Secondary plots:

- Divertor C II and C III emission vs. electron density and Bt direction (measure of divertor leakage)
- Midplane C6+ density vs. electron density and Bt direction (measure of core penetration)
- Midplane and crown SOL flows vs. R-Rsep, electron density, and Bt direction
- Times constants of C signal decay for core/divertor spectroscopic diagnostics following end of methane puff vs. electron density and Bt direction
- Interpretive modeling of all of the above with OEDGE-DIVIMP

Collector probe samples will be shipped to Sandia (Wampler) for NRA analysis, and UT-Knoxville (Duran) for LAMS analysis.

Langmuir probes, CER, TS, and passive spectroscopic diagnostics will have to go through their standard analysis workflows to turn raw data into physics quantities.

OEDGE-DIVIMP interpretive modeling (Nichols, Zamperini, Elder) will be carried out for all 8 configurations. SOL reconstructions, constrained by all available diagnostics, will calculated for each configuration, followed by tests of impurity transport models.

If successful, this experiment will support at least 3 papers, and supply data for 2 Ph.D. theses (Duran and Zamperini).

7. Radiation Awareness

A site boundary limit of 300 μrem is requested.

Appendix: ‘Predict First’ Predictions (if applicable)

<Paste in any plots, slides, quotes from papers, or table from work that uses theory or simulation predict specific results expected in this experiment.>

8. References

[Stangeby JNM 2011] P.C. Stangeby, J. Nucl. Mater. 415 (2011) S278-S283.
[Donovan RSI 2018] D.C. Donovan, et al., Rev. Sci. Instrum. 89 (2018) 10I115.
[Elder NME 2019] J.D. Elder, et al., Nucl. Mater. Energy 19 (2019) 287-294.
[Zamperini NME 2019] S.A. Zamperini, et al., Nucl. Mater. Energy 18 (2019) 87-92.
[Neuhauser NF 1984] J. Neuhauser, et al., Nucl. Fusion 24 (1984) 39.
[Stangeby NF 1995] P.C. Stangeby and J.D. Elder, Nucl. Fusion 35 (1995) 1391.
[Stangeby NF 2020] P.C. Stangeby and D. Moulton, Nucl. Fusion (2020) in press
[Senichenkov PPCF 2019] I.Y. Senichenkov, et al., Plasma Phys. Control. Fusion 61 (2019) 045013.
[Asakura JNM 2007] N. Asakura, J. Nucl. Mater. 363-365 (2007) 41-51.
[Boedo JNM 2009] J.A. Boedo, J. Nucl. Mater. 390-391 (2009) 29-37.
[Groth NF 2009] M. Groth, et al., Nucl. Fusion 49 (2009) 115002.
[Duran FST 2019] J.D. Duran, et al., Fus. Sci. Tech. 75 (2019) 493-498.

5. Resources

* Machine Setup

-- Diagnostic Coordinator: Nichols, Jacob
-- 1st Physics Operator: Shafer
-- Target Shot: 178351
-- Ip Direction: Normal
-- Ip Range: 1.0MA
-- Bt Range: -2
-- Bt Direction: Normal
-- Shape: USN - Upper Single Null
-- OSP on lower outer shelf? no
-- Cryopumps :
-- 3d Coils: Standard Error Field Correction
-- 3d Coils Special Setup:
-- I-Coil:
  -- Special Setup: -
-- C-Coil:
  -- Special Setup: -
-- New ASIPP Super-SPAs Needed:: no
-- 3D Programmer: (Other Candidate)
-- Audio Amplifier:
-- Dud Detector: no
-- PCS Software Version: Standard PCS Software
-- PCS Software Comments:
-- PCS Support:
-- NBI (Beam) Programmer: (Other Candidate) Wilcox
-- NBI Feedback Bn:
-- NBI Feedback Rotation:
-- Other PCS Needs:

* Heating/Fueling Systems
-- NBI 30lt: e
-- NBI 30rt: d
-- NBI 150lt:
-- NBI 150rt:
-- NBI 210lt:
-- NBI 210rt:
-- NBI 330lt: d
-- NBI 330rt: e
-- NBI Gas: d2
-- NBI Other:
-- 150 Beam Line Tilted: no
-- 150 Beam Line Angle:
-- Is variable voltage beam capability needed? no
-- Min ECH Power:
-- Max ECH Power:
-- ECH Aimer: (Other Candidate)
-- Helicon Required: no
-- LFS Pellet Pacing: no

-- HFS Pellet Pacing: no

-- Argon Pellet Injector: no

-- Medusa MGI: no

-- Cerberus MGI: no

-- Pellet Shell: no

-- Pellet Shattered: no

-- Theory Prediction: no

-- Simulation Code Run:
-- Simulation Prediction: no

-- Special EC Ops:

-- Gas A: D2
-- Gas B: D2
-- Gas C: none
-- Gas D: none
-- Gas E: none
-- Gas Other: gasline D with C13D4 using value UOB
-- Min. Gyrotrons:
-- Max Gyrotron:
-- Min Acceptable Power (MW):
-- Max Desired Power (MW):
-- Min Acceptable Pulse Length (s):
-- Max Desired Pulse Length (<= 5s):
-- Power Modulation Needed?: no
-- Min Modulation Freq (Hz):
-- Max Modulation Freq (Hz):
-- Power Feedback Control Required: no
-- Mirror Steering Feedback Control Required: no
-- Lithium Li Dropper:
-- PMI Dimes: yes
-- PMI Mimes: yes

Diagnostics

-- Diagnostic Coordinator: Nichols, Jacob

* Profile Diagnostics

-- Core and Horizontal (Tangential) Thomson: E
High Density Edge Channels: Middle
-- CER: E
-- MSE: D
-- CO2 Interferrometer: E
-- ECE Michelson Interferometer:
-- HECE Radiometer:
-- Soft X-ray Toroidal:
-- Soft X-ray Poroidal:
-- Bolometers: I
-- Visible Bremstrahlung:
-- Fast Ion Dalpha (FIDA):
-- Fast Ion Loss Detector (FILD):
-- CORE SPRED:
-- DISRAD:
-- Neutron Counters:
-- Main Ion CER:
-- Neutron Scintillators:
-- 14MeV Neutron Counter (SSBD & PIPS):
-- Gamma Ray Imager (GRI):
-- Imaging Fast Ion D-Alpha (IFIDA):
-- Imaging Neutral Particle Analyzer (INPA):
-- Hard X-Ray (HXR) Bismuth Germanate (BGO) Array:
-- Profile Diagnostics Special Request:

* Fluctuation Diagnostics

-- Magnetics:
-- Fast Magnetics:
-- BES:
-- Doppler Back Scattering (DBS-60):
-- Doppler Back Scattering (DBS-240):
-- High Frequency (15-50 MHz fluctuations) Doppler Back Scattering (DBS-HF):
-- Cross-Polarization Scattering (CPS):
-- Correlation Electron Cyclotron Emission (CECE-60):
-- Phase Contrast Imaging:
-- Electron Cyclotron Emission Imaging (ECEI):
-- Ion Cyclotron Emission (ICE):
ICE Setup: Standard
-- Microwave Imaging Reflectometry (MIR):
-- Radial Interferometer-Polarimeter (RIP):
-- Fluctuation Diagnostics Special Request:

* Edge Diagnostics

-- Upper Filterscopes: E
-- Lower Filterscopes: I
-- Midplane Filterscopes: I
-- Upper Divertor Langmuir Probes: E
-- Lower Divertor Langmuir Probes: D
-- ASDEX Gauges: I
-- Upper Penning Gauge:
-- Lower Penning Gauge:
-- Density Profile Reflectometer (edge + core):
-- Midplane Reciprocating Probe: I
Background SOL characterization needed for modeling.
-- X-point Reciprocating Probe: I
Background SOL characterization needed for modeling.
-- Upper Divertor IRTV:
-- Lower Divertor IRTV:
-- Midplane Periscope IRTV:
-- 90 deg UCSD Fast Framing Camera:
-- 225 deg UCSD Fast Framing Camera:
-- Upper Tangential TV: E
-- Lower Tangential TV: I
-- MDS Spectrometer: E
-- Divertor Thomson: I
Wed like to use the combined SHELF-12 and SAS-4 setup (config #5)
Config: shelf / Sample Rate: 50Hz / TS Consultant: glassf
-- Periscope Flow: D
Characterizing the far-SOL flows is a component of the MP.
-- Lower Divertor Flow TV:
-- DiMES TV:
-- Tile Current Monitors:
-- Tangential Soft X-ray:
-- LLAMA (Lyman-alpha Measurement Apparatus):
-- Edge Diagnostics Special Request:

* Other Diagnostics

-- Laser Blow Off:
-- Impurity Powder Dropper:
-- Impurity Granule Injector:

6. Radiation Awareness

-- Site Boundry Dose: 300

VITA

Jonah D. Duran was born on November 4th 1992 in Athens, Georgia. He was raised in both eastern North Carolina and east Tennessee before attending college at The University of Tennessee, Knoxville. As an undergraduate student, he studied nuclear engineering. Jonah also gained experience as an undergraduate research assistant with both Dr. Brian Wirth and Dr. Maik Lang where his study focused on nuclear materials. In addition, he worked as a resident assistant for the university beginning in 2013 until acquiring a BS degree in May of 2015. Jonah continued his studies in nuclear engineering as a graduate research assistant under the advisement of Dr. David Donovan. During this time, his research was based at the DIII-D tokamak in San Diego, California with an emphasis on nuclear fusion science and technology. Jonah was an author of professional posters, conference presentations, and publications. He defended his thesis for a MS degree in nuclear engineering and received his MS degree in December of 2017. Jonah continued with Dr. David Donovan for a PhD in the nuclear engineering department following 2017. During this time, he received a U.S. Department of Energy Office of Science Graduate Student Research award for a year of research at Oak Ridge National Laboratory. Jonah also acted as president for the Trout Unlimited college chapter at The University of Tennessee, “Vols on the Fly”. He defended his PhD dissertation in the summer of 2022 in time for a fall graduation.